1991

Ultrasonic flaw classification and sizing

Sung-Jin Song
Iowa State University

Order Number 9212192

Ultrasonic flaw classification and sizing

Song, Sung-Jin, Ph.D.

Iowa State University, 1991

U·M·I
300 N. Zeeb Rd.
Ann Arbor, MI 48106

Ultrasonic flaw classification and sizing

by

Sung-Jin Song

A Dissertation Submitted to the

Graduate Faculty in Partial Fulfillment of the

Requirements for the Degree of

DOCTOR OF PHILOSOPHY

Department: Aerospace Engineering and Engineering Mechanics
Major: Engineering Mechanics

Approved:

Signature was redacted for privacy.

In Charge of Major Work

Signature was redacted for privacy.

For the Major Department

Signature was redacted for privacy.

For the Graduate College

Iowa State University
Ames, Iowa

1991

TABLE OF CONTENTS

GENERAL INTRODUCTION

All kinds of engineering materials and structures have flaws, some of which can cause catastropic failures. In modern high performance engineering applications, the structural integrity of these materials and structures are quite often evaluated using fracture mechanics. This evaluation in turn requires information on the flaw geometry (location, type, shape, size, and orientation). The ultrasonic nondestructive evaluation (NDE) method is one technique that is commonly used to provide such information. Usually, the ultrasonic flaw characterization process involves two steps; flaw classification (determination of the flaw type) and flaw sizing (prediction of the flaw shape, orientation and size parameters). The purpose of this research effort is to develop new techniques for both classification and sizing. Specifically, we will use ultrasonic models and measurements to evaluate the type and size of single isolated flaws inside materials. The results generated will be in a form that can be used directly in quantitative estimates of the flaw's significance.

Ultrasonic Flaw Classification

Cracks are usually considered more dangerous than non-crack-like (volumetric) defects. Thus, it is common to try to classify only between more severe (crack-like) and less severe (volumetric) flaws. For weldments, however, it is desirable to introduce more flaw classification categories (such as cracks, porosity and slag inclusions) not only for the evaluation of the structural integrity of the weld but also for the improvement of the weld process performance.

In conventional ultrasonic NDE, flaw classification is usually done by a human operator based on heuristic experience-based echodynamic pattern identification techniques [1,2]. Unfortunately, these methods are highly operator dependent and often do not perform well in practice.

Recently, there have been developed model-based quantitative classification techniques which extensively use amplitude information of the ultrasonic signals received from flaws. Shcherbinskii and Belyi [3], for example, proposed the use of "form factors" of flaws which are features that can be measured with a tandem transducer method. Expanding this concept, Volpinkin [4] developed a modified method which can be applied to classifying flaws in weldments. The satellite-pulse technique developed by Gruber [5] also falls into this category. Very recently, Chiou and Schmerr [6] developed a new scheme which can distinguish smooth vs. sharp-edged flaws by use of the time-separation and amplitude difference of mode-converted diffracted signals in a quasi-pulse-echo configuration. On the other hand, there has been work on the use of features extracted from the frequency domain of ultrasonic signals. This approach is known as ultrasonic spectral analysis [7,8] and typically uses broadband ultrasonic pulses. Fitting and Adler [9] have reviewed previous work in this area in detail.

All of the methods mentioned above need to capture very "strong" features so that the flaw type information can then be directly decided by a human operator. Unfortunately, in many realistic situations the classification problems are not so simple and the criteria fuzzy. To take care of this difficulty, new approaches using "ultrasonic pattern recognition"

techniques, have been introduced that use a variety of modern digital signal processing techniques, and various decision-making algorithms. This approach involves three steps: 1) measurement of the ultrasonic signals from flaws, 2) the extraction of a set of features from those measurements which can serve as a basis for a given classification problem, often using digital signal processing techniques, and 3) solving the given classification problem using these features and a specific decision-making criterion.

Some of the earlist work related to ultrasonic pattern recognition was done by Rose and his co-workers [10,11,12]. They extracted physically based features from the ultrasonic time domain signals and adopted the Fisher linear discriminant function as a classifier. Burch and Bealing [13] used a similar approach to classify relatively large buried flaws in ferritic steel welds into four different groups. In their work, they used more general features extracted from the time domain and a weighted minimum distance pattern recognition algorithm as a classification rule. In a following study, Burch [14] expanded this idea to a classification problem of vertical and near vertical planar defects using a combination of pulse-echo and tandem techniques.

The rapid advance in the field of artificial intelligence (AI) has stimulated the development of some approaches which extensively use AI concepts. For example, Mucciadi and his co-workers [15,16] developed an ultrasonic inversion procedure which discriminated and sized flaws by the use of adaptive learning networks, using features extracted from the power spectrum. Recently, Koo [17] presented a flaw classification system using modeling, signal processing and adaptive learning networks. In his work, he used more "fundamental" (model-based) features extracted from the time

domain. A rule-based expert system approach has also been used to solve ultrasonic flaw classification problems by Schmerr and his co-workers [18,19]. In this case, nine "fundamental" features extracted from the time and frequency domains were used. More recently, artificial neural networks have seen applications in this area.

Artificial neural networks [20,21] loosely model the structure and operation of the human brain. They are composed of richly interconnected simple processing elements which can operate simultaneously to achieve high speed data processing. They have the ability to approximate arbitrary mappings from sets of input-output patterns presentations. Furthermore, once trained, they can produce outputs "instantaneously." The recent discovery of new training algorithms such as back-propagation [22] has brought widespread interest in the application of neural networks to various fields. In the field of NDE, neural networks trained by the back-propagation algorithm have been used to solve a variety of sizing and classification problems [23,24,25,26,27]. However, "back-propagation" neural networks have been criticized because of some important disadvantages. These disadvantages include the need for a trial-and-error based determination of the optimal network structure, lengthy training times, and opaqueness of the way in which the neural net reaches its "conclusions." Recently, a probabilistic neural network (PNN) [28,29,30] model has been developed that has all the advantages of neural networks mentioned above but without the typical disadvantages.

In the first topic of this work, we present an ultrasonic flaw classification problem in weldments that can be solved by use of the PNN.

We show that such a network is simple to construct and fast to train. We also demonstrate that the PNN is able to exhibit the high performance of other neural networks, such as feed forward nets trained via back-propagation, while possessing the PNN's important advantages of speed of training, explicitness of architecture, and physical meaning of the outputs. Finally, we show that the performance of the PNN is also comparable to that of common statistical approaches, such as the K-nearest neighbor method.

Ultrasonic Flaw Sizing

Obtaining flaw size, shape and orientation information from ultrasonic measurements is one example of having to solve an inverse problem of elastic wave scattering. Conventional ultrasonic NDE techniques have not been particularly effective in solving such problems even though a wide variety of ultrasonic flaw sizing approaches [31,32,33] have been developed including amplitude-based and time-of-flight methods, detailed imaging methods, and equivalent sizing methods.

Conventional field inspections have used only the amplitude information of ultrasonic signals for flaw sizing. For small flaws they have often simply relied on the comparison of the amplitude of flaw signals with those of standard references, like flat-bottom holes, of known sizes. This method has been known as the use of Distance-Gain-Size (DGS) curves and was first formulated and experimentally determined by Krautkramer [34].

Even though this method has a wide variety of applications [2], very few following studies have considered the DGS approach after Krautkramer's original work. Recently, however, Schmerr and Sedov [35] and Sedov, Schmerr and Song [36] have described new ultrasonic scattering models for

the pulse-echo response of a flat-bottom hole in contact and immersion testing, respectively. An important feature of these models is their ability to predict both the near-field and far-field response of a flat-bottom hole, whose axis is aligned with the axis of a piston transducer. In [36], these predictions were shown to be in good agreement with experiments when single frequency DGS-like curves were considered.

In the second subject of this dissertation, we show that "true" DGS curves (obtained from the time-domain amplitude measurements as in Krautkramer's original approach) can be developed easily from these models through deconvolution procedures and Fourier analysis. These theoretical DGS curves will be shown to be in good agreement with experiments even in the very near-field. Finally we also use the models to predict frequency response curves that compare favorably with experimental results in both the near and far-fields.

The use of DGS curves is restricted to flaws smaller than the beam size of a transducer. For sizing relatively large flaws, echodynamic patterns [1,2] have been extensively used, based on mapping the amplitude variation as a function of position of a transducer scanning over a flaw. These conventional approaches, however, are often not quantitative enough to produce the size information needed for modern fracture mechanics calculations [37,38].

Some advanced techniques attempt to avoid limitations of conventional amplitude-only approaches by use of time-of-flight information or a combination of time-of-flight and amplitude information. There are, for example, the Time-of-Flight Diffraction (TOFD) method

[39,40,41] and the Satellite-Pulse techniques [5,42]. Even though these techniques have achieved successes in some applications, they still have some important limitations in the information they can extract about flaw geometry.

To get more complete information about flaw geometry, various detailed imaging methods have been developed [43] including the Synthetic Aperture Focussing Technique (SAFT) [44,45], and the amplitude and transit time locus curves (ALOK) [46], acoustical holography [47], and ultrasonic tomography [48]. These techniques require detailed scanning and considerable data processing. Even after this time consuming process, the results sometimes cannot be directly used for fracture mechanics calculations.

In between the two extremes of conventional methods and detailed scanning methods, there is a model-based approach called equivalent flaw sizing [49,50,51]. In this approach, flaws are reconstructed in terms of "best-fit" equivalent ellipsoids (for volumetric flaws) or ellipses (for cracks) obtained from a relatively small number of ultrasonic measurements at different transducer orientations and locations. This approach has been developed based on ultrasonic scattering models such as the Born approximation for volumetric flaws [49,50] or the Kirchhoff approximation for cracks [51]. Recently, a unified algorithm that can be applied to both volumetric flaws and cracks was developed by Schmerr and et al. [52].

For the successful implementation of this approach, there are two major issues which one has to consider: 1) accuracy of experimental measurement of the equivalent radius, which is defined as the distance from

the flaw centroid to the front surface tangent plane, and 2) the efficiency of the optimization algorithm used to determine the best-fit flaw parameters from the measured equivalent radius data.

The equivalent radius, which is the one of the basic parameters on which most current equivalent flaw sizing methods rely, is normally obtained, for small flaws directly from the ultrasonic waveform itself by use of signal processing. Unfortunately, most current methods to determine this quantity suffer from the so-called "zero-of-time" problem [53,54,55]. Even though efforts still continue to be undertaken to solve this problem [56], no entirely satisfactory and general solution is currently available. Furthermore, most methods currently available are restricted to relatively small flaws. In this dissertation, we show three new approaches which can solve the zero-of-time problem in performing equivalent sizing for both relatively large and small flaws.

The efficiency of the optimization scheme (the second issue mentioned above) in the past was an important issue because of the very complicated nonlinear nature of the problem [50]. Fortunately, Chiou and Schmerr [57] have recently eliminated this issue by developing a new approach where they reformulated the optimization problem into a two-step problem involving a simple linear least squares optimization step and the solution of a straightforward eigenvalue problem. In this study, we take advantage of this two-step algorithm in the development of our new equivalent flaw sizing techniques.

In the third topic of this dissertation, we show how the equivalent flaw sizing concept can be combined with simple time-of-flight measurements to

produce a new time-of-flight equivalent (TOFE) sizing method. This method uses information on the time-of-flight, and transducer location and orientation at each measurement to produce the best-fit ellipsoid that matches the ultrasonic data measured at different look-angles. We demonstrate with experiments that the TOFE method is indeed a viable sizing tool for relatively large flaws (> 1mm) even in anisotropic materials such as composite materials and in welds provided that the wavespeed in the material is well characterized.

In the last topic of this dissertation, two new equivalent flaw sizing approaches for relatively small (< 1mm) flaws are addressed; 1) an amplitude-based equivalent (ABE) sizing method for obtaining the best-fit equivalent flaw geometry by use of amplitude ratios measured at different transducer orientations, and 2) a first moment (FM) method for estimating the equivalent radius of a flaw directly from the time domain flaw waveform response. We show how these approaches can both provide new methods to solve the zero-of-time problem and demonstrate the excellent performance of these methods with experiments.

Explanation of Dissertation Format

This dissertation is written in the alternate format in compliance with the regulation of the Graduate College Thesis Office of Iowa State University. The dissertation includes a general introduction followed by four parts and a general summary. The literature cited in the General Introduction can be found following the General Summary.

These parts contain four different topics of research work that either have already been published or will be submitted for publication. In each

part, figures and tables are placed at the end of the contents according to the requirement for journal publication. Part one, which presents a new methodology for ultrasonic flaw classification in weldments using probabilistic neural networks, is an extension of a paper which appeared in Review of Progress in Quantitative Nondestructive Evaluation, Vol. 10A, pp. 697-704. This extended paper has been submitted to Journal of Nondestructive Evaluation. The second part, which describes a model-based approach to construct the DGS diagrams and frequency response curves for flat-bottom holes, is an extension of part of a paper which appeared in Review of Progress in Quantitative Nondestructive Evaluation, Vol. 10A, pp. 59-65. This extended paper has been accepted and will appear in Research in Nondestructive Evaluation. The third part, which describes a new time-of-flight equivalent sizing method for relatively large flaws, is an extension of part of a paper which will appear in Review of Progress in Quantitative Nondestructive Evaluation, Vol. 11. This extended paper has been accepted and will appear in Research in Nondestructive Evaluation. The last paper, which discusses two new approaches in equivalent flaw sizing for relatively small flaws, is an extension of part of a paper which will appear in Review of Progress in Quantitative Nondestructive Evaluation, Vol. 11. This extended paper has been submitted to Nondestructive Testing and Evaluation. Finally, a general summary is given at the end of this dissertation.

PART I. ULTRASONIC FLAW CLASSIFICATION IN WELDMENTS USING PROBABILISTIC NEURAL NETWORKS

Ultrasonic flaw classification in weldments using probabilistic neural networks

Sung-Jin Song and Lester W. Schmerr

Center for NDE and
Department of Aerospace Engineering and Engineering Mechanics

Iowa State University

Ames, Iowa 50011

ABSTRACT

A probabilistic neural network is used here to classify flaws in weldments from their ultrasonic scattering signatures. It is shown that such a network is both simple to construct and fast to train. Probabilistic nets are also shown to be able to exhibit the high performance of other neural networks, such as feed forward nets trained via back-propagation, while possessing important advantages of speed, explicitness of their architecture, and physical meaning of their outputs. Probabilistic nets are also demonstrated to have performance equal to common statistical approaches, such as the K-nearest neighbor method, while retaining their unique advantages.

INTRODUCTION

The detection of flaws in weldments is important because defects such as cracks, porosity and slag inclusions can seriously degrade the structural integrity of a weld. However, it is equally important to identify (i.e., classify) these flaws in order to make quantitative estimates of their influence on structural performance. Previously, a wide variety of classification approaches have been used for ultrasonic inspections including heuristic experience-based methods [1,2], signal processing and pattern recognition schemes [3,4], adaptive learning methods [5], and expert systems [6,7]. More recently, neural networks have been applied to such problems [8,9,10].

Neural networks [11,12] are ideally suited for classification problems since 1) they can automatically learn the mapping between their inputs and outputs through examples - in the case of ultrasonic flaw classification problems, the inputs are the features of ultrasonic signals, and outputs are flaw classes, 2) they can generalize to cases that have not been explicitly learned, and 3) once trained, can produce classification results "instantaneously." However, neural networks such as feed forward nets trained by the back-propagation algorithm [13] have some important disadvantages. First, for these nets the choice of the appropriate network architecture for a particular classification task must be normally made on a purely trial and error basis. Second, once the architecture is chosen, the training times are often very lengthy. Finally, the methods of how the neural network obtains its results are opaque to the user.

Recently, a probabilistic neural network (PNN) [14,15,16], which has all the advantages of neural networks listed above but without the typical disadvantages, has been developed for classification problems. The simple feed

forward network structure of the PNN appears similar to that used in networks trained by the back-propagation algorithm (Figure 1). However, the PNN architecture is determined directly by the training samples and the training of PNNs is noniterative and hence very fast. Another key advantage of the PNN is that its outputs can be interpreted as probability distributions for the various classes, allowing one to use a variety of standard decision-making methods. The main disadvantage of the PNN is that all training samples must be stored and used in classifying unknown test samples. In various practical classification problems, the performance of the PNN is known to be equivalent to that which can be achieved by networks trained by back-propagation with large numbers of training samples [17]. Furthermore, special-purpose processors and commercial systems such as the Lockheed Probabilistic Neural Network Processor [18], Neuralware's Neuralworks Professional II Plus, and Hecht-Nielsen's Explore Net 3000, now implement PNNs at high speeds through the use of parallel hardware.

In this work, we briefly describe the structure of the PNN and apply it to the classification of flaws in weldments with two experimental examples. We will show that the network's behavior is relatively insensitive to choices of the training sets and user-defined network parameters and compare its performance to both a standard "back-propagation" network and that of a K-nearest neighbor statistical classifier.

PROBABILISTIC NEURAL NETWORKS

Even though the architecture of a PNN is quite similar to that of other feed forward neural networks, there are some very unique characteristics in its structure and use. In this section, some of the important characteristics of the PNN including architecture, training, and classification, will be discussed briefly.

Architecture

The basic architecture of the PNN is shown in Figure 1 for a classification problem involving 3 classes. The network contains four layers consisting of 1) an input layer, where the features to be used by the network are presented, 2) a pattern layer where each of the pattern units accepts a weighted sum of the inputs and applies a Gaussian activation function to that sum at its output, and 3) a summation layer (in which summation units are connected to each pattern unit of the appropriate class and sum the outputs of the attached pattern units) where the summed output is weighted by a user-defined parameter and then presented to the fourth and final output layer, and 4) an output layer, whose values are used directly in the classification process.

Unlikely other neural networks, the PNN architecture is strictly determined by the number of classes of a specific problem and the choice of training samples. The numbers of output units and corresponding summation units are equal to the number of classes, and the number of pattern units is the same as the number of the training samples. Finally, the number of input units is equal to the dimension of the input feature vectors. There are three types of weights in the PNN. The weights, W_{ij}, (Figure 1) are determined completely by

the training set since they are defined directly from the input features of each training sample. In fact, the only adjustable parameters in the network are the other two sets of weights - the user-defined parameters, C_i , and the smoothing constant, σ in the activation functions (Figure 1). The determination of both of these latter weight types are discussed below.

Network Training

The training of the PNN can be achieved by a very simple three stage process (Figure 1):

1. Given the choice of inputs, a pattern layer output node, N_j , (j = 1, 2, ... N) is chosen for each of the N training samples.

2. If we let X_{ij} (i = 1, 2, ... M, j = 1, 2, ... N) denote the M features corresponding to each training example, then the weights, W_{ij} , between the j-th second layer node and the i-th input feature, X_i , are obtained by simply setting $W_{ij} = X_{ij}$.

3. Finally, each pattern unit in the second layer is connected to the summation unit which corresponds to the known class of that training example.

Since the weights, W_{ij} , are determined without any iterations, training can be done "instantaneously." Furthermore, what the training steps do is to estimate the probability density function for each class from training samples, similar to a standard statistical Parzen window approach [19]. For example, if we have n_i training samples from a certain class, then step 1 and 2 produce n_i Gaussian distributions which have their centers at the training samples. Then, at step 3 these individual Gaussian distributions are summed to estimate the probability density function.

Choice of Network Parameters

Once the network is trained, as described above, the only remaining parameter choices are the user-defined parameters C_i (i = 1, 2, 3) and the "smoothing" parameter σ (Figure 1). The user-defined parameters C_i , which are given by $C_i = h_i l_i / n_i$, are determined by three factors; the a priori probability, h_i , the cost factor, l_i , and the number of training samples, n_i, in that particular class. The product of factors, $h_i l_i$, can be simply set equal to one, in which case all output flaw classes are weighted equally in "cost." However, if the user wishes to place a stronger weight on a particular class, say cracks, the $h_i l_i$ product can be used to adjust the decision-making process. The smoothing parameter, σ, in contrast, is used to adjust the collective importance of each of the individual patterns in the second layer pattern units [14]. A small value of σ tends to emphasize the individual patterns, while a large value of σ instead smoothes out the behavior over many patterns. This corresponds to producing narrow Gaussian distributions around the training samples for the case of small values of σ, or generating wide Gaussian distributions for the case of large values of σ. Although there are some theoretical results which govern the choice of σ [15], σ was chosen here on a more pragmatic basis. An acceptible σ was defined here as one which both produced "good" classification results as well as a stable behavior of the network over a wide range of σ-values. Thus, the behavior of the network was made insensitive to the specific choice of σ.

Classification

Once the training and the network parameter selection are done, classification can be performed on the test samples. The classification rule is to classify a test sample to that class whose output nodes in the PNN has the

maximum output, corresponding to the maximum expected risk for the test sample. This is just the Bayes rule [19], which states: Classify a test sample x to the class i, if

$$h_i l_i P_i(x) \geq h_j l_j P_j(x) \qquad (i \neq j)$$

where,

h_i = the a priori probability of occurance of test samples from class i.

l_i = the loss factor associated with the misclassification.

$P_i(x)$ = the probability density functions for class i.

EXPERIMENTAL EXAMPLE I

In this section, an experimental example will be presented where the PNN is used to separate welding defects into three distinct classes (crack, porosity, slag inclusion). The PNN architecture for solving this problem, training and test data set, input features, and the performance obtained will be addressed.

Input Features and Network Architecture

The ultrasonic data we used in this study were supplied by Westinghouse Corporation. Digitized A-scan narrow band waveforms were taken using contact transducers from deliberate welding defects, of the three types mentioned previously, in steel test blocks. The test blocks had stainless steel cladding on the surfaces which made the ultrasonic waveforms quite noisy. A total of 239 waveforms (104 waveforms from cracks, 53 waveforms from porosity, and 82 waveforms from slag inclusions) were selected.

The success of any neural network often depends crucially on the choice of the input features. Ideally, these features should be distinguishing characteristics of different flaw classes and "fundamental" in the sense that they are based on the physics of the scattering process. Since the data set provided to us by Westinghouse was not taken specifically to extract any particular set of such features, we used a variety of more heuristic features as inputs. As shown in Table 1, these features consisted of ten time domain features and four frequency domain features. To extract these features from the digitized waveforms, a feature extraction program was developed using FORTRAN 77 on an APOLLO DN 10000 workstation.

Approximately half of these waveforms were used to train the network, and the remaining waveforms served as a testing set to evaluate the network

performance. Using these training samples, a probabilistic neural network was implemented also using FORTRAN 77, and executed on the APOLLO workstation. The specific PNN used had 14 nodes in the input layer, 120 nodes in the pattern layer, and 3 nodes both in the summation and the output layers. The network also employed Gaussian (exponential) functions as the activation functions in the pattern layer.

Performance Evaluation Criteria

The two performance evaluation criteria that were used for measuring the performance of the network were the correct accept rate, $(CA)_i$, and the false reject rate, $(FR)_i$, for each of the three classes (i = 1, 2, 3) where $(CA)_i$ and $(FR)_i$ are defined as:

$$(CA)_i = \frac{m_i}{n_i} \qquad (i = 1, 2, 3)$$

m_i = number of testing examples from class i classified correctly

n_i = total number of testing examples from class i

$$(FR)_i = \frac{\sum_j m_{ji}}{\sum_j n_j} \qquad (j \neq i)$$

m_{ji} = number of testing examples from class j classified to class i

n_j = total number of testing examples from class j

Thus the correct accept rate is merely that proportion of samples from a certain class c_i classified correctly, while the false reject rate is the proportion of samples from the other classes misclassified into that class c_i. Note that the terms "accept" and "reject" used here do not imply that the flawed part is in any way "acceptable" or "rejectable."

Performance of PNN

Figures 2a, b show plots of the correct accept rate and of the false reject rate, respectively, for each of the three flaw classes for the factor $h_i\, l_i = 1$ ($i = 1, 2, 3$) and the parameter σ varied over a range of 0 - 0.3. This range of σ-values we found produced the highest correct accept rates, and, as Figures 2a, b show, the network performance did not vary substantially with the choice of σ in this range. Although the correct accept rates are lower here than what we would like to see in a production classification system, our extensive experience with this data set suggests that this performance is the best that can be expected for this set of features and experiments. Since the particular choice of σ was not crucial here, we arbitrarily picked $\sigma = 0.1$ for all our subsequent testing. Figure 3a shows a summary of the total performance of the network under the conditions mentioned above.

Sensitivity to the training set is also an important factor in neural network performance. A certain network may perform well with a specific training set, but then not show the same performance with a different training set. In that case we can not use the network for practical classification purposes. To test the sensitivity of the PNN performance to the choice of training set, the training and test sets initially used in the tests described above were switched. As can be seen from Figure 3b, the resulting network produced very similar results to the

original one except for the false reject rates for cracks. Given the overall performance of both networks, however, this difference is probably not significant.

Figures 4a, b, c show the behavior of the network when different cost factors l_i were used for each class. Cracks are often much more important than other flaws. Thus, by making the cost factor for cracks higher than those for slag inclusions or porosity, the correct accept rate for cracks can be significantly improved. For this particular experiment, this improved performance only comes, however, at the price of increased false rejects for cracks also as shown in Figure 4a, b, c.

Although the Gaussian distribution function is typically used as an activation function in the second layer of a probabilistic network, there is nothing fundamental about this choice. We also considered the Cauchy distribution [15] which is an activation function choice with longer "tails" than the Gaussian. A comparison of Figure 3 (Gaussian activation function case) and Figure 5 (Cauchy activation function case) shows that there is little change in network performance with either choice. This implies that the PNN is stable with respect to some variation in the activation function.

Comparison to K-Nearest Neighbor Classifier

Theoretically, for small σ the PNN should behave similar to a K-nearest neighbor (KNN) classifier, which is a very simple and popular classical classifier [14,15]. The most well-known form of the KNN classification rule [19] is to classify a test sample to the class that the majority of its K nearest neighbors belong to. Stated explicitly, this rule is as follows: Classify a test sample x to class i, if

$$\frac{p_i \cdot k_i}{n_i} \geq \frac{p_j \cdot k_j}{n_j} \qquad (i \neq j)$$

where

n_i = the total number of samples from class i

p_i = a priori probability of class i

k_i = the number of samples from class i in volume V which contains K nearest samples

$K = \sum k_i$ = number of samples in volume V

To compare the performance of the PNN and the KNN approaches, a KNN classifier was trained and tested on exactly the same data sets as used in our original PNN experiments. Figures 6a, b show plots of the correct accept rate and the false reject rate, respectively, for each of the three classes where the number of nearest neighbors, K, varied over a range of 1 - 15. As shown in those figures, the KNN classifier performance did not vary much with the choice of K in this range, so we arbitrarily chose K = 7 for all subsequent calculations. Figure 7 shows the classification performance of the KNN classifier with K = 7. A comparison of Figure 3 for the PNN and Figure 7 shows that there is no practical difference between these two results. Actually, this similarity in performance was expected, since we chose to use a relatively small σ in our PNN. However, the PNN does have the advantage over the KNN classifier of being able to complete classifications very rapidly and to produce estimates of the actual probability distributions of the flaw classes at the outputs

[16,17]. These probability distributions might be used to advantage if a user were to employ, for example, a more sophisticated classification decision-making process.

EXPERIMENTAL EXAMPLE II

Feed forward networks trained by the back propagation algorithm (also called the generalized delta rule) [13] are often used for classification problems because of their ability to represent very general mappings. Recently, Brown and DeNale [9] have used such a neural network to distinguish two kinds of welding defects (planar and volumetric). Here, we will consider the same problem using the PNN and the KNN approaches.

Brown and DeNale's Problem

In Brown and DeNale's work [9], a steel weld containing lack of fusion defects (planar) and a block with side drilled holes (volumetric) were inspected to get digitized A-scan ultrasonic waveforms from defects. From these waveforms, 5 features including the mean, variance, coefficient of variance, coefficient of skewness, and coefficient of kurtosis were obtained by a feature extraction program. A total of 68 waveforms were taken, among which 44 waveforms (22 waveforms from planar flaws and 22 waveforms from volumetric flaws) were used for the training samples and 24 waveforms (12 waveforms from planar flaws and 12 waveforms from volumetric flaws) were used for test samples. A 3-layer back-propagation neural network with five input nodes, five hidden layer nodes, and two output nodes was trained with the training set. A sigmoid activation function was used in this network. After the network was trained, the test set was presented to the network for classification, and an overall classification accuracy of 98.5% was reported with only one misclassification in the test set.

PNN Architecture and Performance

Since Brown and DeNale [9] published a complete table of their training and testing sets, it was possible to construct a PNN to also solve their problem. A standard PNN with Gaussian activation functions was implemented using FORTRAN 77 on a Decstation 5000. The PNN in this case had 5 nodes in the input layer, 44 nodes in the second layer, and 2 nodes both in the third and the output layers, because their data set had 5 input features and 44 training samples and 2 classes as output. The two performance evaluation criteria of the correct accept rate and the false reject rate were chosen again.

Figures 8a, b show plots of the correct accept rate and of the false reject rate, respectively, for each of the two flaw classes with the factors, $h_i\, l_i = 1$ $(i = 1, 2)$ and the parameter σ varied over a range of 0.2 - 6. As shown in those figures, the network performance did not vary at all with the choice of σ in this range. Furthermore, the PNN showed the exactly same result as that of Brown and DeNale's back-propagation network. It showed the overall correct accept rate of 98.5% with one misclassified test set, which was the one that the back-propagation network also misclassified.

The same data set was also presented to the KNN classifier. Figures 9a, b show the classification results by the KNN classifier with K varied over a range of 1 - 15. The KNN performance stayed almost the same regardless of the choice of K in this range. Again, the classification accuracy was the same as those of the two neural networks.

CONCLUSIONS

We have demonstrated the use of PNN's for the classification of welding flaws by ultrasonics. The PNN has been shown to have a simple architecture that is easily constructed and trained. Since the training is noniterative, it is very fast. Also, since the PNN produces estimates of the probability density function of each class at outputs, the manner in which this net obtains its results is not opaque to the user. Finally,we have shown that in the PNN users can put subjective information into the decision making process by providing suitable weighting factors in the summation layer.

The PNN produced reasonable and consistent classification performances for both experimental cases considered. For Brown and DeNale's data set, the PNN matched the high performance of a back-propagation network but without the training time "overhead." Thus the PNN is a good choice as a classifier for these weld problems.

Also for both cases, the PNN's behaved similarly to KNN classifiers. Even though the performance of the PNN was very similar to that of the KNN classifier, the PNN does have the advantage of speed. This speed advantage will be further strengthened, as mentioned previously, by the recent developement of various special-purpose processors and commercial systems which have efficiently implemented the PNN in both hardware and software.

ACKNOWLEDGEMENTS

We would like to thank Dr. Warren Junker of Westinghouse Corporation for providing us with the ultrasonic data used in this study and to thank Mr. Bill Clark of Westinghouse Corporation for his constant support and encouragement. We also acknowledge the use of the data published by Mr. Brown and Mr. DeNale of David Taylor Research Center. This research was supported by the Center for Nondestructive Evaluation at Iowa State University.

REFERENCES

1. International Institute of Welding, Handbook on the Ultrasonic Examination of Welds, Cambridge, England: The Welding Institute for the International Institute of Welding, 1977.

2. International Institute of Welding, The Evaluation of Ultrasonic Signals, Cambridge, England: The Welding Institute for the International Institute of Welding, 1987.

3. S. F. Burch, "Objective characterization of welding defects using physical based pattern recognition techiniques." in Review of Progress in Quantitative Nondestructive Evaluation, Vol. 7B, Eds. D. O. Thompson and D. E. Chimenti, pp. 1495-1502, New York: Plenum Press, 1988.

4. J. L. Rose, "Elements of a feature-based ultrasonic inspection system." Material Evaluation, Vol. 42, No. 2, pp. 210-218, 1984.

5. M. F. Whalen and A. N. Mucciardi. "Inversion of physically recorded ultrasonic waveforms using adaptive learning network models trained on theoretical data." in Proc. ARPA/AFML Review of Progress in Quantitative NDE. Ed. D. O. Thompson. Air Force Materials Laboratory Technical Report AFML-TR-78-205, pp. 341-367, 1979.

6. S. M. Nugen, L. W. Schmerr, K. M. Christensen, and B. K. Lovewell, "Design and implementation of an expert system for flaw classification," Microcomputer Applications, Vol. 9, pp. 1-8, 1990.

7. L. W. Schmerr, K. E. Christensen, S. M. Nugen, L.-S. Koo and C.-P. Chiou. "Ultrasonic Flaw Classification - An Expert System Approach." in Review of Progress in Quantitative Nondestructive Evaluation, Vol. 8A, Eds. D. O. Thompson and D. E. Chimenti, pp. 657-664, New York: Plenum Press, 1989.

8. S. J. Song and L. W. Schmerr, "Ultrasonic flaw classification in weldments using neural networks." in Review of Progress in Quantitative Nondestructive Evaluation, Vol. 10A, Eds. D. O. Thompson and D. E. Chimenti, pp. 697-704, New York: Plenum Press, 1990.

9. L. M. Brown and R. DeNale, "Classification of ultrasonic defect signatures using an artificial neural network." in Review of Progress in Quantitative

Nondestructive Evaluation, Vol. 10A, Eds. D. O. Thompson and D. E. Chimenti, pp. 705-712, New York: Plenum Press, 1990.

10. D. Berry, L. Udpa and S. S. Udpa, "Classification of ultrasonic signals via neural networks." in Review of Progress in Quantitative Nondestructive Evaluation, Vol. 10A, Eds. D. O. Thompson and D. E. Chimenti, pp. 697-704, New York: Plenum Press, 1990.

11. R. P. Lippmann, "An introduction to computing with neural nets." IEEE ASSP Magazine, pp. 4-22, April 1987.

12. Y. H. Pao, Adaptive Pattern Reconition and Neural Networks. Reading, MA: Addison-Wesley Publishing Co., Inc., 1989

13. D. E. Rumelhart, G. E. Hinton and R. J. Williams, "Learning internal representations by error propagation." in Parallel Distributed Processing, Eds. D. E. Rumelhart, J. L. McClelland and the PDP Research Group, Vol. 1, pp. 318-362, Cambridge, MA: MIT Press, 1986

14. D. F. Specht, "Probabilistic neural networks for classification, mapping, or associative memory." in Proceedings of the IEEE InternationalConference on Neural Networks, Vol. 1, pp. 525-532, 1988.

15. D. F. Specht, "Probabilistic neural networks." Neural Networks, Vol. 3, pp. 109-118, 1990.

16. D. F. Specht, "Probabilistic neural networks and polynomial adaline as complementary techniques for classification." IEEE Transactions on Neural Networks, Vol. 1, No. 1, pp. 111-121, 1990.

17. D. F. Specht and P. D. Shapiro, "Generalization accuracy of probabilistic neural networks compared with back-propagation networks." in Proceedings of the International Joint Conference on Neural Networks, Vol. 1, pp. 887-892, 1991.

18. T. P. Washburne, M. M. Okamura, D. F. Specht and W. A. Fisher, "The Lockheed probabilistic neural network processor." in Proceedings of the International Joint Conference on Neural Networks, Vol. 1, pp. 513-518, 1991.

19. R. O. Duda and P. E. Hart, Pattern Classification and Scene Analysis, New York: John Wiley & Sons, 1973.

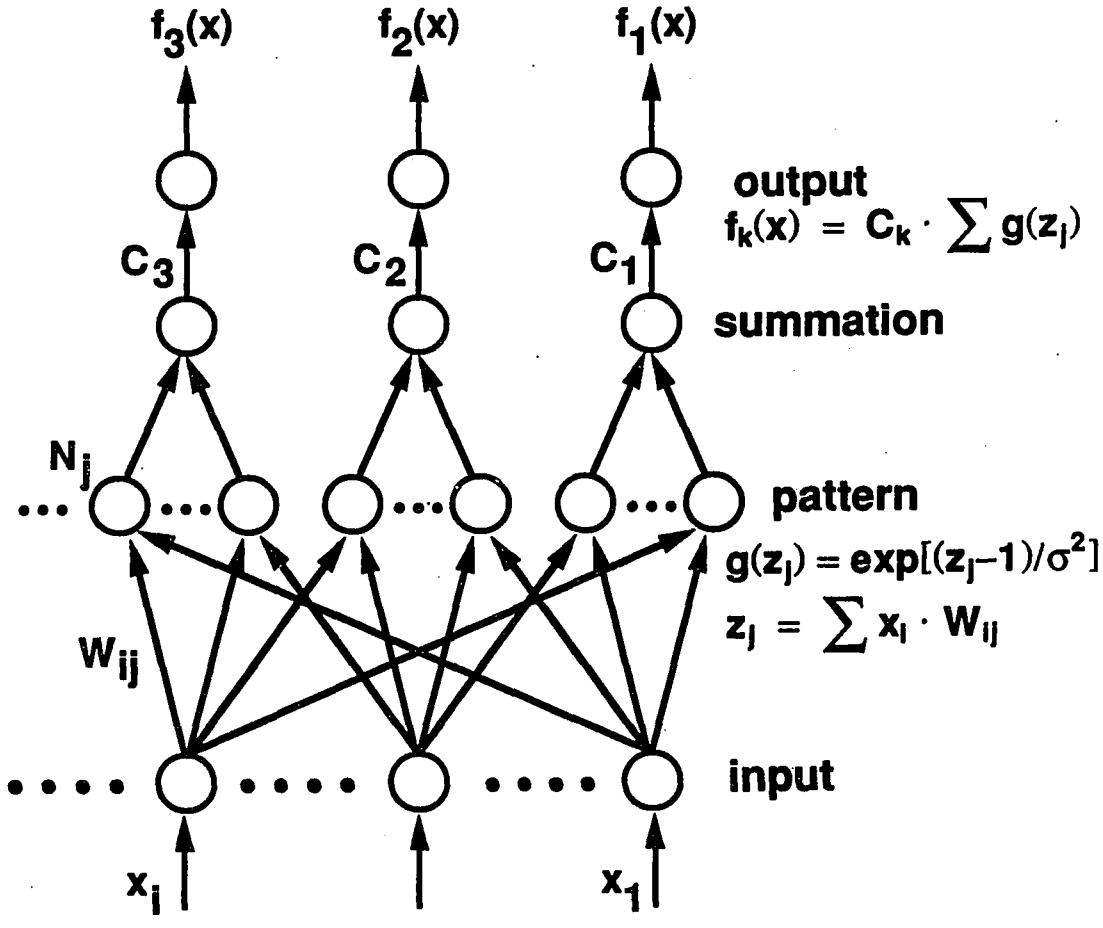

Figure 1. Probabilistic neural network architecture.

Table 1. Input features to the PNN

Time Domain Features
1) number of signal groups
2) pulse duration of the 1st group signal
3) pulse duration of the 2nd group signal
4) pulse duration of the 3rd group signal
5) energy of the 1st group signal
6) energy of the 2nd group signal
7) energy of the 3rd group signal
8) interval between the 1st and the 2nd groups
9) interval between the 2nd and the 3rd groups
10) antisymmetry of signal
Frequency Domain Features
11) number of maxima of the magnitude spectrum
12) number of minima of the magnitude spectrum
13) number of deep minima of the magnitude spectrum
14) number of shallow minima of the magnitude spectrum

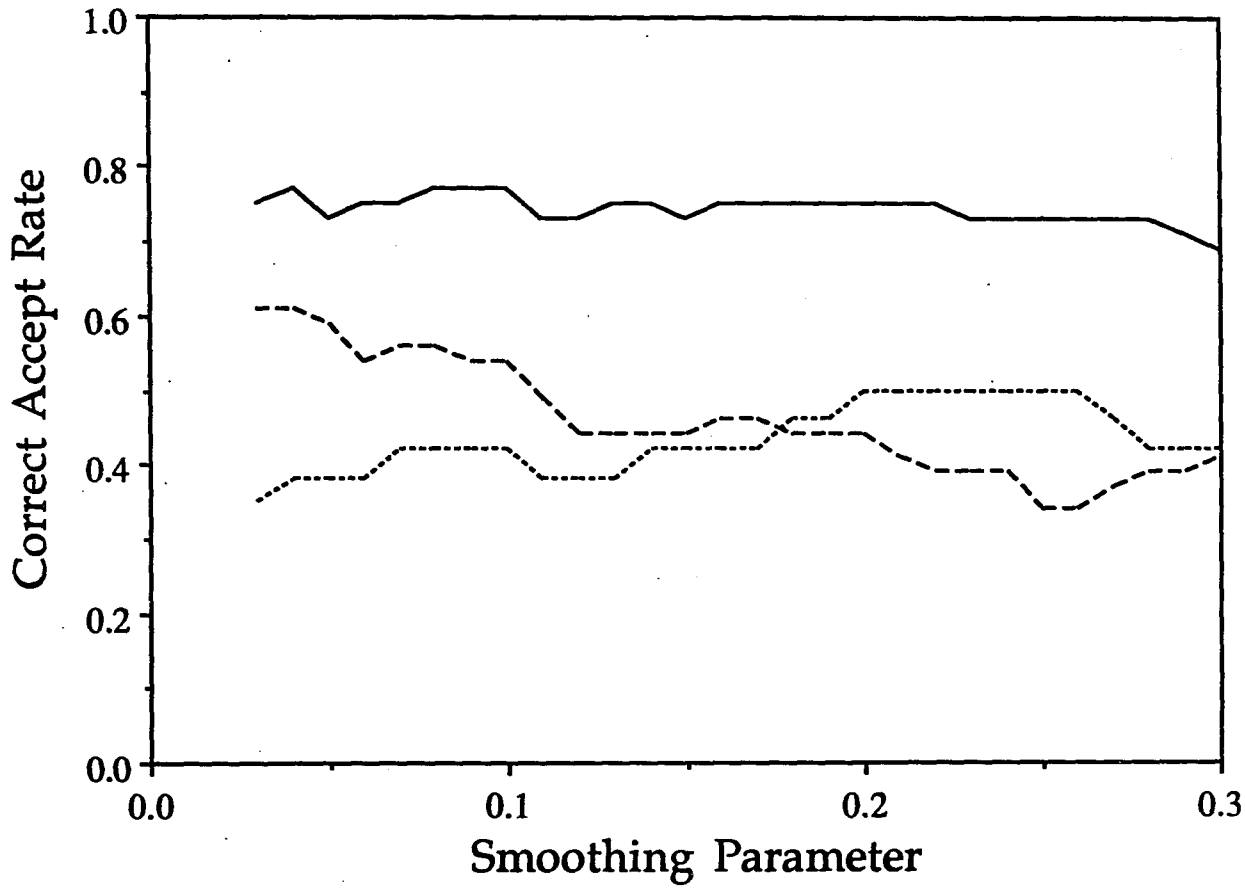

Figure 2a. Correct accept rates of welding defects by the PNN for different choices of the smoothing parameter σ and with $h_i l_i = 1$ for all.
Cases: cracks (solid line), porosity (small dashes), and slag inclusion (large dashes)

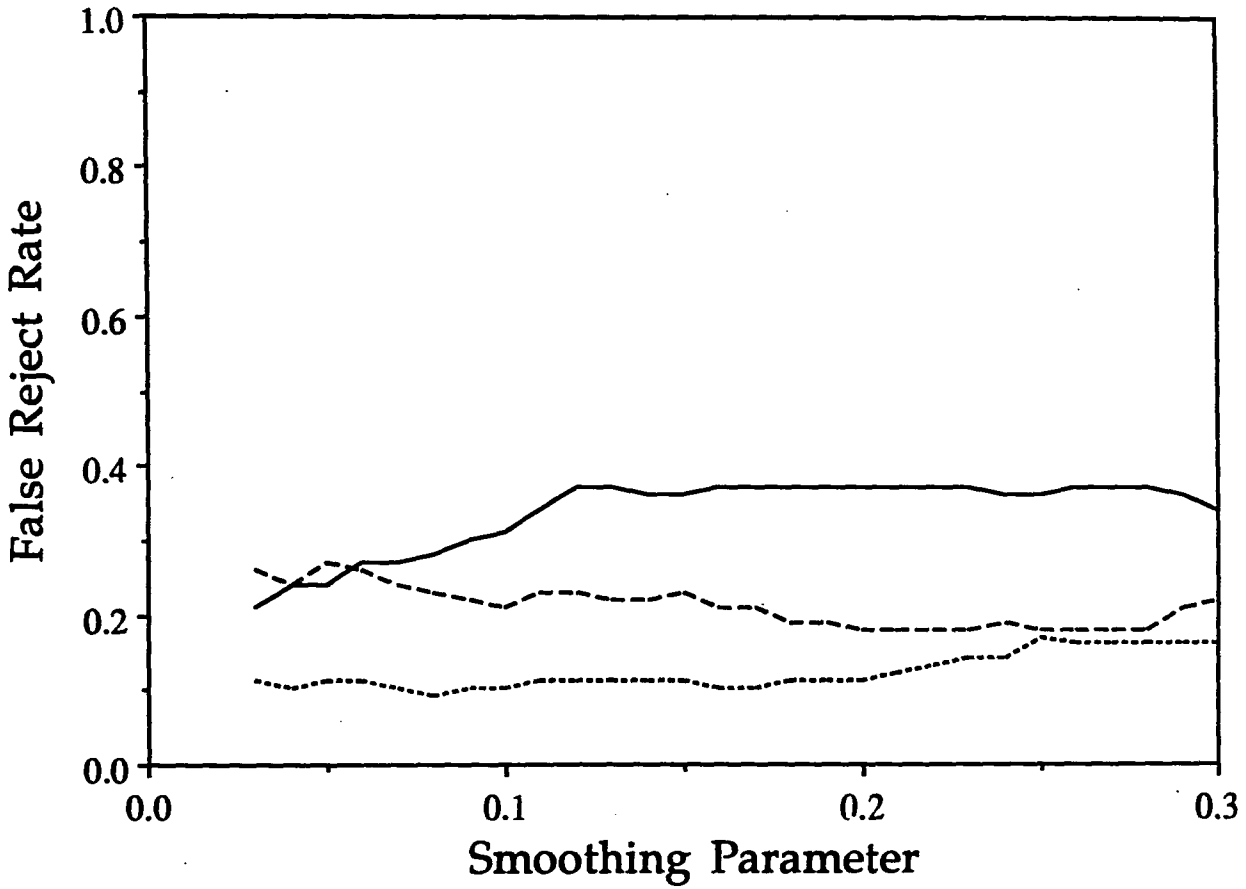

Figure 2b. False reject rates of welding defects by the PNN for different choices of the smoothing parameter σ and with $h_i l_i = 1$ for all.
Cases: cracks (solid line), porosity (small dashes), and slag inclusion (large dashes)

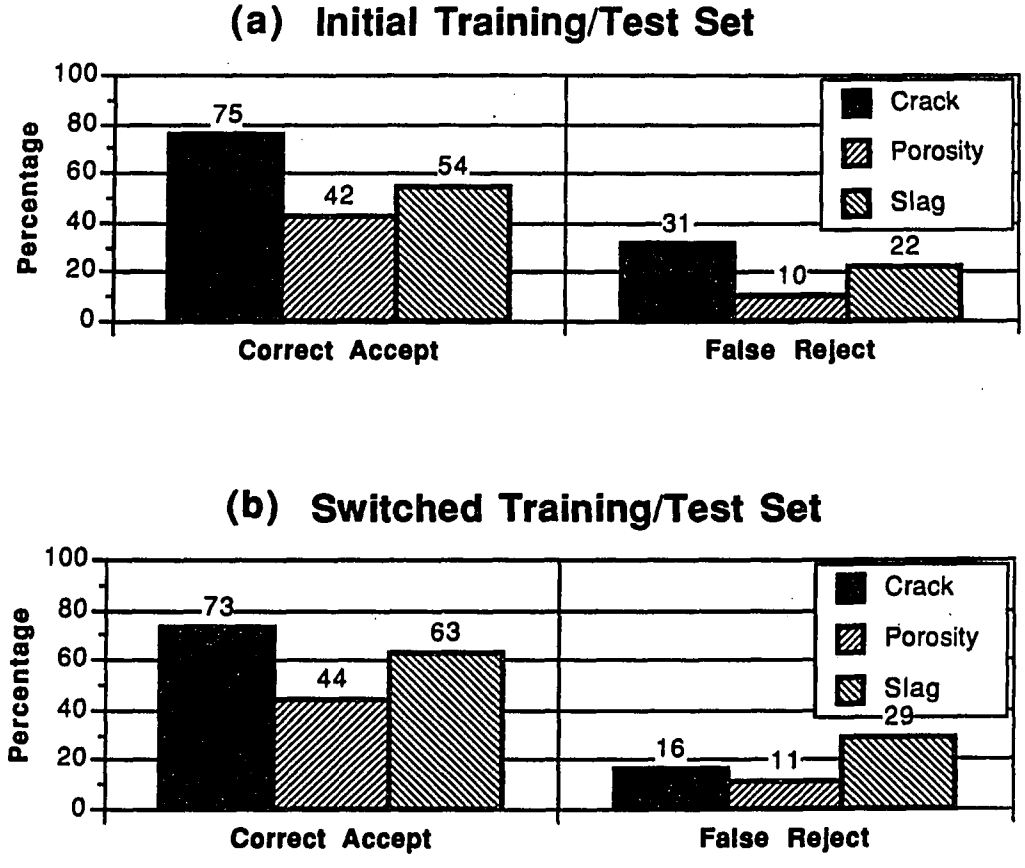

Figure 3. Summary of PNN performance for (a) original training/test sets and (b) switched training/test sets. Activation function: Gaussian, $h_i l_i = 1$ for all cases, $\sigma = 0.1$.

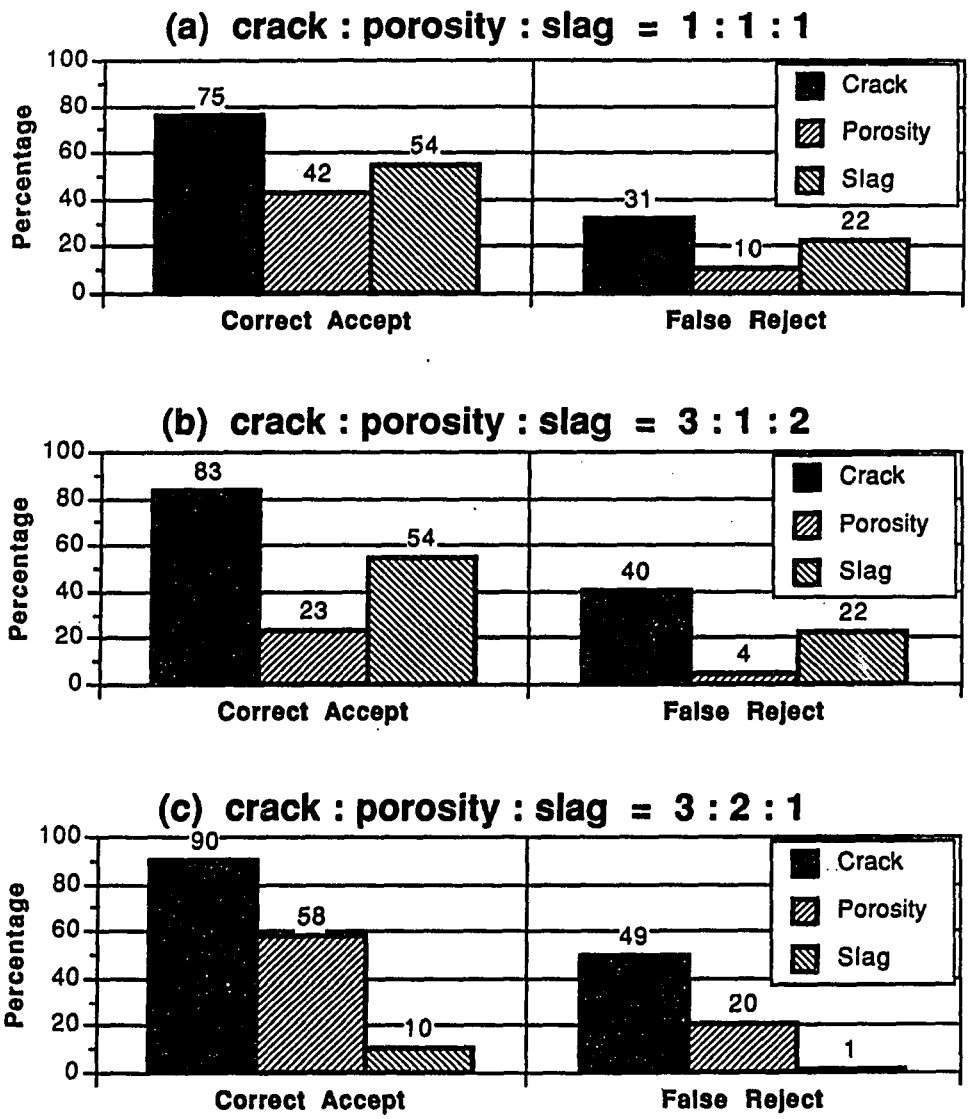

Figure 4. Influence of the choice of the h_i l_i parameter on PNN performance.

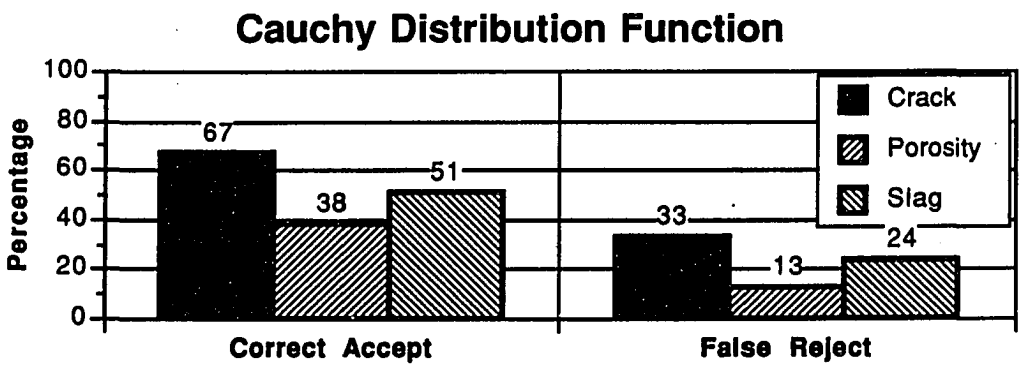

Figure 5. Summary of PNN performance when a Cauchy activation function is used in the pattern layer. $h_i l_i = 1$ for all cases, $\sigma = 0.1$.

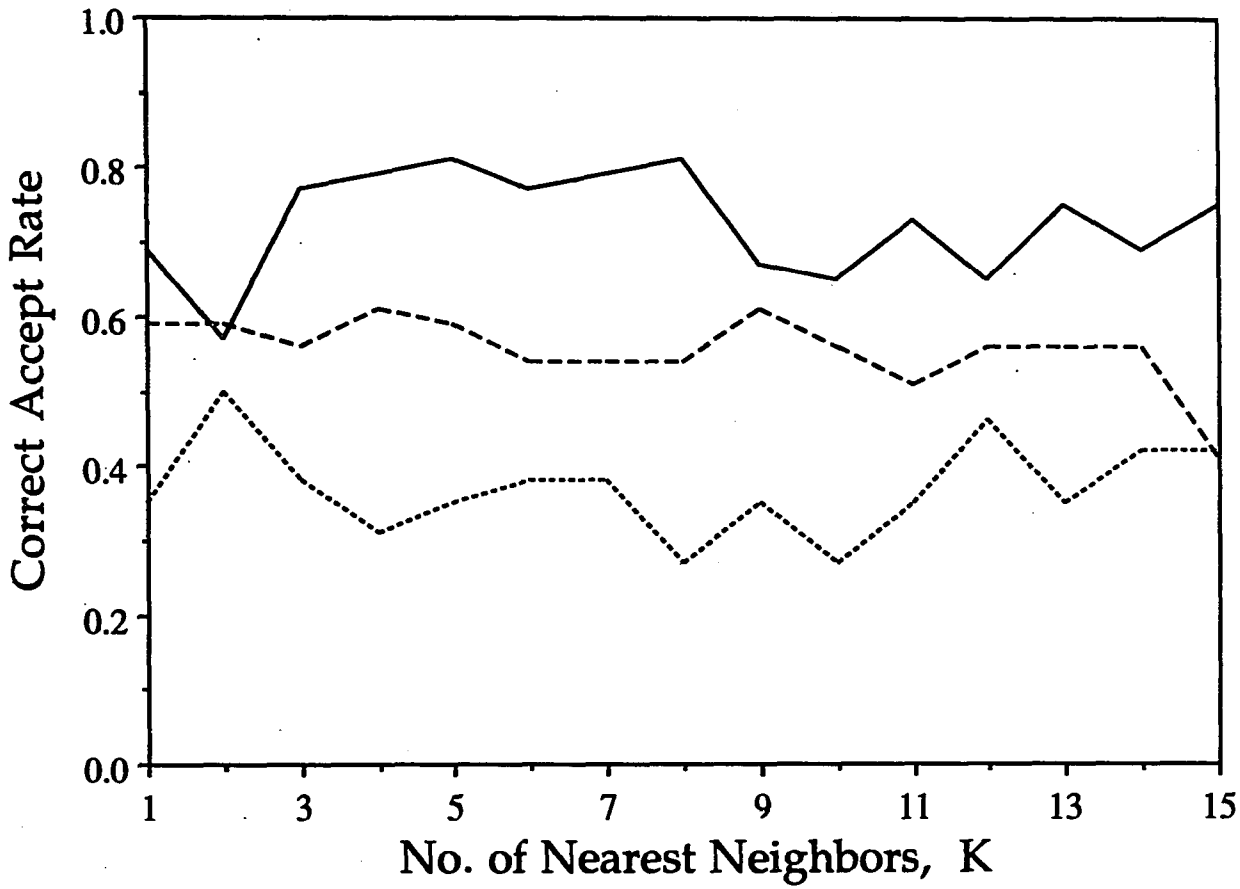

Figure 6a. Correct accept rates of welding defects by the KNN method for different choices of the parameter K, and with p_i equal for all.
Cases: cracks (solid line), porosity (small dashes), and slag inclusion (large dashes)

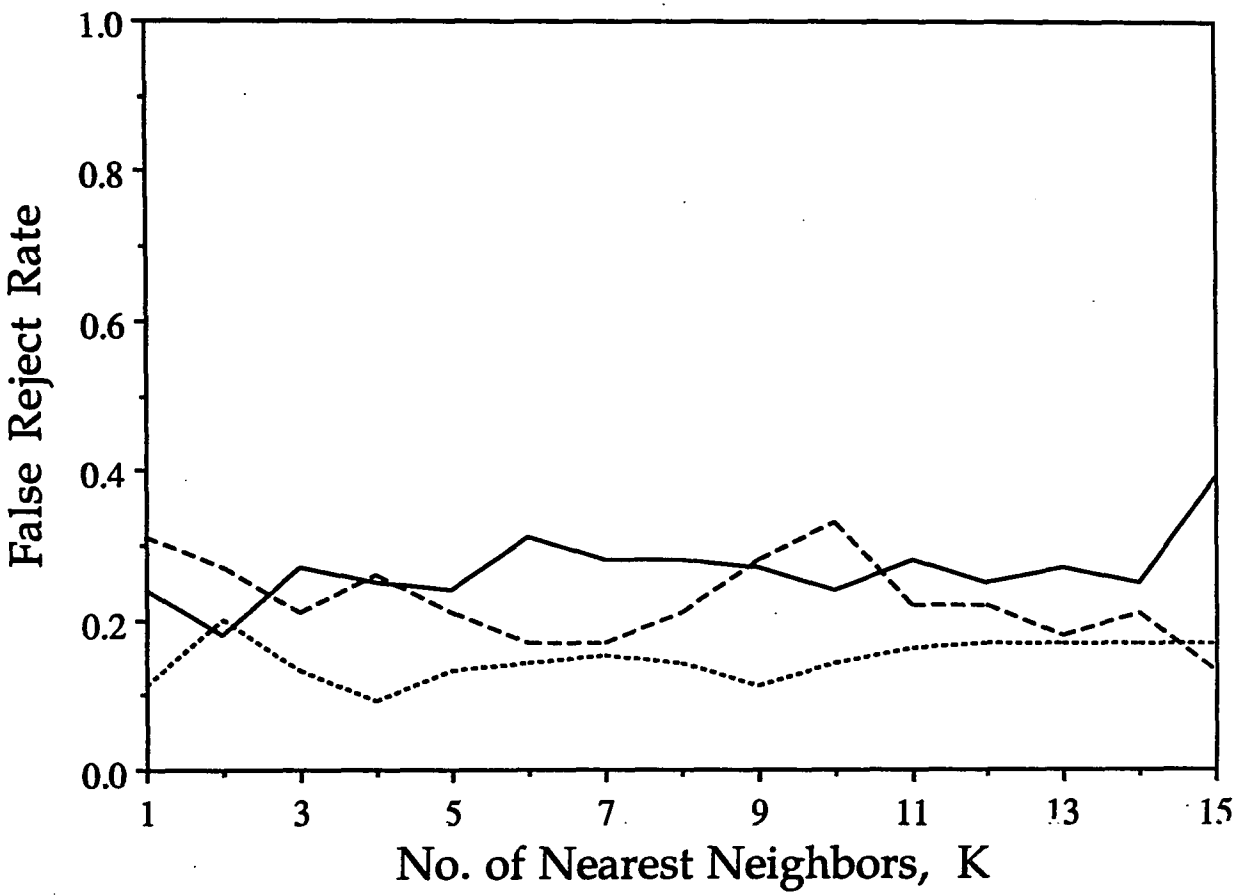

Figure 6b. False reject rates of welding defects by the KNN method for different choices of the parameter K, and with p_i for all.
Cases: cracks (solid line), porosity (small dashes), and slag inclusion (large dashes).

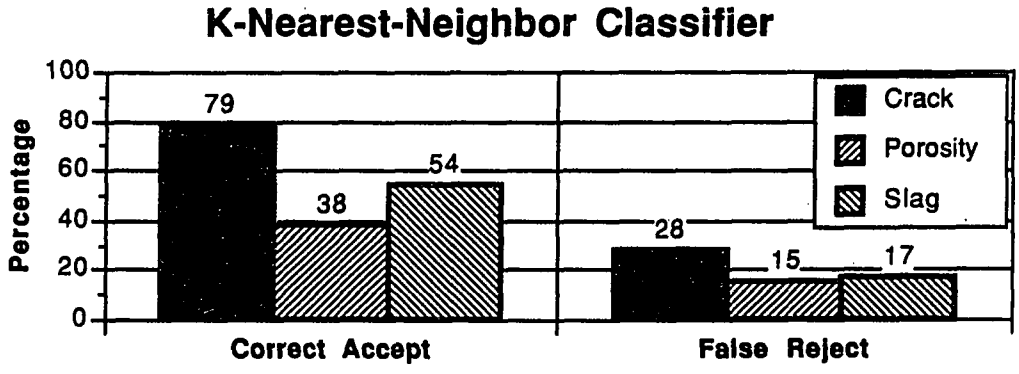

Figure 7. Summary of KNN method performance. p_i equal for all cases, K = 7.

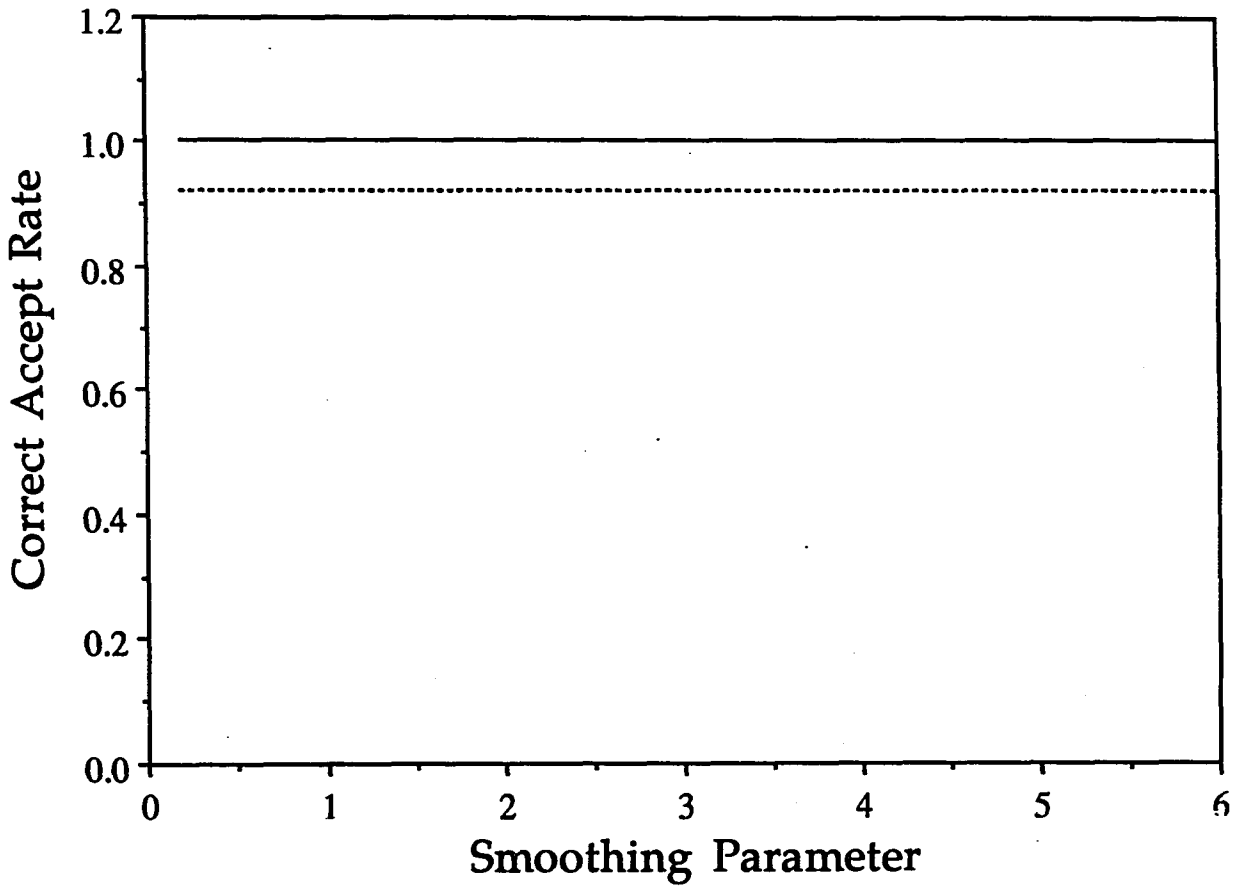

Figure 8a. Correct accept rates of welding "defects" in Brown and DeNale's problem for a PNN with different choices of the smoothing parameter σ and with $h_i l_i = 1$ for all.
Cases: planar defects (solid line), volumetric defects (dashed line).

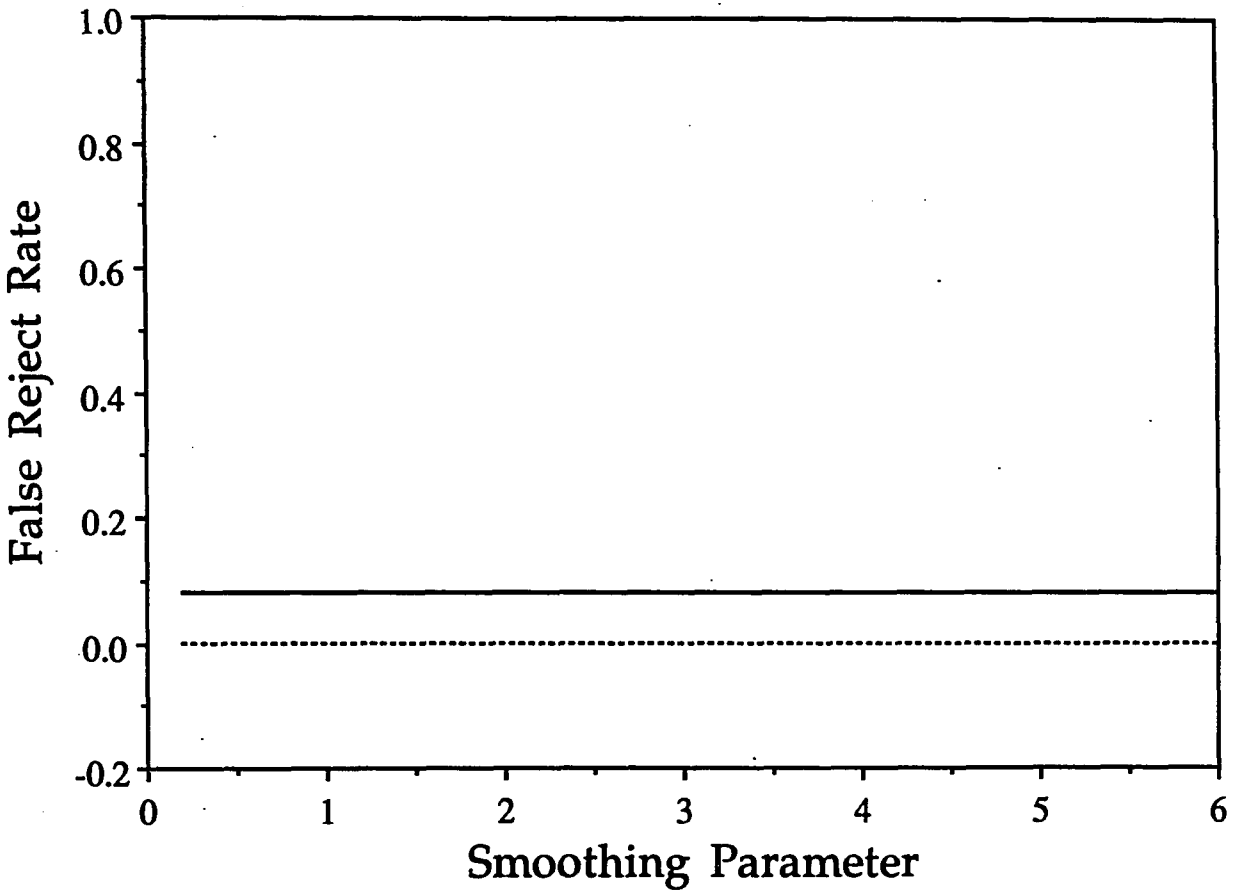

Figure 8b. False reject rates of welding "defects" in Brown and DeNale's problem for a PNN with different choices of the smoothing parameter σ and with $h_i l_i = 1$ for all.
Cases: planar defects (solid line), volumetric defects (dashed line).

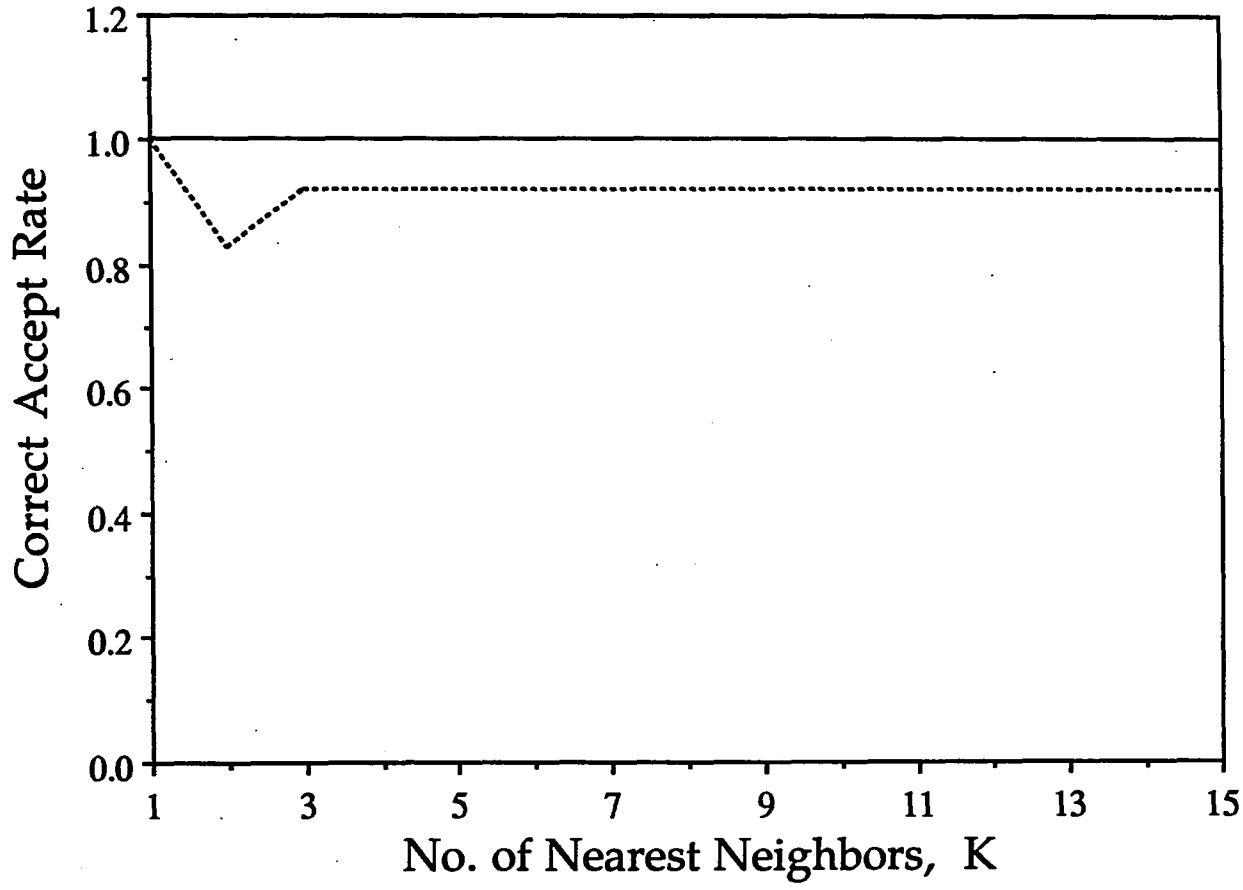

Figure 9a. Correct accept rates of welding "defects" in Brown and DeNale's problem for the KNN method with different choices of the parameter K and with p_i equal for all. Cases: planar defects (solid line), volumetric defects (dashed line).

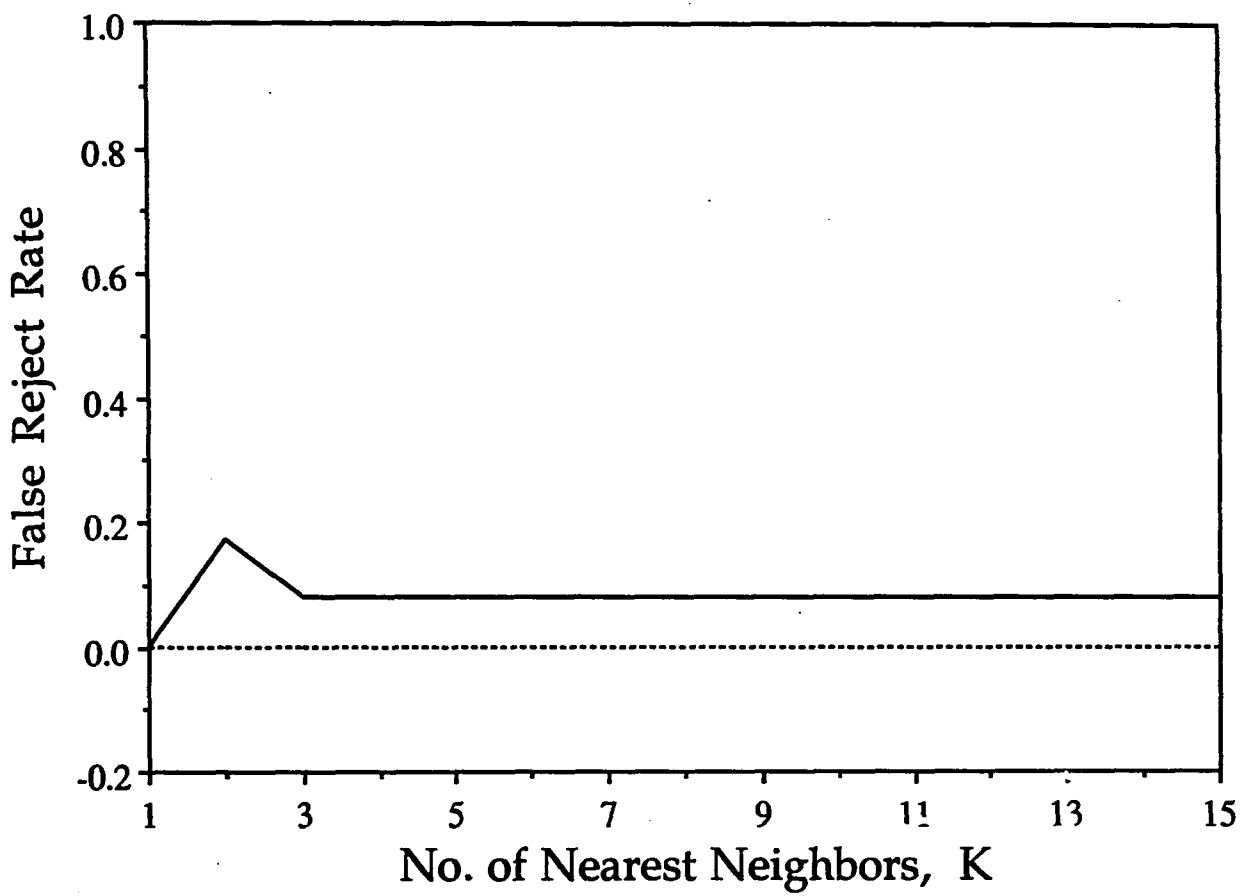

Figure 9b. False reject rates of welding "defects" in Brown and DeNale's problem for the KNN method with different choices of the parameter K and with p_i equal for all. Cases: planar defects (solid line), volumetric defects (dashed line).

PART II. DGS DIAGRAMS AND FREQUENCY RESPONSE CURVES FOR A FLAT-BOTTOM HOLE: A MODEL-BASED APPROACH

DGS diagrams and frequency response curves for a flat-bottom hole: a model-based approach

Sung-Jin Song and Lester W. Schmerr

Center for NDE and
Department of Aerospace Engineering and Engineering Mechanics
Iowa State University
Ames, Iowa 50011

Alexander Sedov

Department of Mechanical Engineering
Lakehead University
Thunder Bay, Ontario
Canada P7B5E1

ABSTRACT

Recently, we have developed analytical scattering models for predicting the pulse-echo response of a flat-bottom hole in both contact and immersion testing. Here, we present the results of a series of experimental validations of the immersion case model. It is shown that the model can be used to develop distance-gain-size (DGS) curves and frequency response curves that compare favorably with experiments even in the very near field of the transducer. In fact, the model is shown to reproduce the entire scattered waveform from the hole quite accurately. The quality of these results suggest that the model can serve as an important new theoretical reference standard for a variety of ultrasonic calibration and sizing applications.

INTRODUCTION

Recently, Schmerr and Sedov [1] and Sedov, Schmerr and Song [2] described ultrasonic scattering models for the pulse-echo response of a flat-bottom hole in contact and immersion testing, respectively. An important feature of these models is their ability to predict both near-field and far-field responses of a flat-bottom hole, whose axis is aligned with the axis of a piston transducer. In [2], these predictions were shown to be in good agreement with experiments, when single frequency distance-gain-size (DGS) curves were considered.

The single frequency DGS curves obtained in [2] were not "true" DGS curves since they were obtained from frequency domain measurements rather than the usual time-domain amplitude measurements [3]. Here we will show that such "true" DGS curves can also be developed easily from the models through deconvolution procedures and Fourier analysis. These theoretical DGS curves will be shown to be in good agreement with complimentary experiments. Finally, we will also use the models to predict frequency response curves, at fixed transducer-to-hole distances, that compare favorably with experimental results in both the near and far-fields.

The quality of all these results suggests that the flat-bottom hole models are sufficiently accurate to serve as a theoretical standard for many ultrasonic calibration, sensitivity and sizing applications, where the hole need not necessarily be located in the far-field region of the transducer.

DGS CURVES

Over thirty years ago, Krautkramer [3,4] first formulated and experimentally determined DGS diagrams for on-axis circular perfect reflectors in water. Using a simple model of the transducer/hole interaction, Krautkramer showed that in the far-field of the transducer the average pressure, <p>, received from the hole should be given by a form such as

$$<p> = p_o \exp(2i\kappa z) (A_b/\lambda z) (A_t/\lambda z) \quad (1)$$

(Here the phase term is included for comparison with the model results discussed later, although they were not included in Krautkramer's original form.) where z is the distance from the transducer face to the hole, κ is the wave number, $\lambda = 2\pi/\kappa$ is the wavelength, A_b and A_t are the cross-sectional areas of the hole and transducer, respectively, and

$$p_o = \rho \upsilon_o c \quad (2)$$

is a reference pressure, in terms of the density, ρ, and wavespeed, c, of the fluid, and the velocity υ_o on the face of the piston transducer. Note, however, that p_o is not the pressure on the face of the transducer [2].

If, in contrast, the flat-bottom hole is on-axis and very close to the transducer, Krautkramer argued that the average pressure received at the transducer should then be

$$\langle p \rangle = p_o \left(\frac{A_b}{A_t} \right) \tag{3}$$

Because the form of the response between these two limits was unknown, Krautkramer proposed linking the values predicted by Eqs (1) and (3) with experiments done in the near-field. For this to be accomplished, the reference pressure, p_o, must also be determined experimentally. For a large (larger than the radius of the transducer) perfect reflector, Krautkramer again showed in the far-field, this reference reflector would produce an average pressure, $\langle p \rangle_r$, given by

$$\langle p \rangle_r = p_o \exp(2i\kappa z) \, (A_t / 2\lambda z) \tag{4}$$

and in the very near-field

$$\langle p \rangle_r = p_o \tag{5}$$

From these results, therefore, the quantity p_o can be found [3,4].

The models presented in [1,2] essentially fill in the missing details for the near-field response of a flat-bottom hole and reference reflector that allows one to construct DGS diagrams and reference reflector curves without tedious experimental "fill-ins" of data in regions where Eqs. (1) and (3) or Eqs. (4) and (5) are not valid. Also, the model in [2] consistently includes the effect of the interface present in immersion testing.

Since detailed derivations of the new flat-bottom hole models have been given previously [1,2], in the next section we will only summarize the essential elements and results of the models.

IMMERSION TESTING FLAT-BOTTOM HOLE MODEL

Figure 1 shows a pulse-echo immersion testing configuration with a flat-bottom hole at normal incidence, where the center of the hole is assumed to be aligned with the central axis of the transducer.

Sedov, Schmerr and Song [2] have previously derived an approximate analytic expression for the average velocity received by an immersion compressional wave transducer from a flat-bottom hole for the geometry of Figure 1. The key approximations on which that model is based are:

1. The shear strength is neglected, i.e., the model replaces the elastic solid specimen by an equivalent fluid medium.
2. The interaction of the incident waves with the hole is treated via a Kirchhoff-like approximation of the boundary conditions.
3. The scattered waves transmitted to the hole and received back at the transducer are obtained via a generalization of the ordinary method of stationary phase that uses virtual source positions to properly account for the interface [2].

When the two media are the same, the result of [2] reduces to the single medium case considered in [1].

Using the above assumptions, the average velocity received by the transducer can be given as

$$
\begin{aligned}
\langle v_z \rangle \;=\; & v_o \left(\frac{b}{a}\right)^2 \Bigg[T_{12}\left(\frac{\pi}{2}\right) T_{21}\left(\frac{\pi}{2}\right) \cdot \exp\left(2i\kappa_1 h_1 + 2i\kappa_2 h_2\right) \\
& - \left(\frac{a}{\bar{R}_o}\right)^{1/2} \left(\frac{\sin^2 \bar{\theta}_1}{|\cos \bar{\theta}_1|}\right)^{1/2} T_{12}\left(\frac{\pi}{2}\right) T_{21}(\bar{\theta}_2) \; \frac{2 J_1 (b\kappa_1 \cos\bar{\theta}_1)}{b\kappa_1 \cos\bar{\theta}_1} \\
& \cdot \exp\left(i\kappa_1 h_1 + i\kappa_2 h_2 + i\kappa_1 \bar{d}_1 + i\kappa_2 \bar{d}_2\right) \\
& - \left(\frac{a}{\bar{R}_o}\right)^{1/2} \left(\frac{\sin^2 \theta_2}{|\cos \theta_2|}\right)^{1/2} T_{12}(\theta_1)\, T_{21}\left(\frac{\pi}{2}\right) \; \frac{2 J_1 (b\kappa_2 \cos\theta_2)}{b\kappa_2 \cos\theta_2} \qquad (6) \\
& \cdot \exp\left(i\kappa_1 d_1 + i\kappa_2 d_2 + i\kappa_1 h_1 + i\kappa_2 h_2\right) \\
& + \left(\frac{a}{\bar{R}_o}\right)^{1/2} \left(\frac{\sin^2 \bar{\theta}_1}{|\cos\bar{\theta}_1|}\right)^{1/2} \left(\frac{a}{R_o}\right)^{1/2} \left(\frac{\sin^2 \theta_2}{|\cos\theta_2|}\right)^{1/2} T_{12}(\theta_1)\, T_{21}(\bar{\theta}_2) \\
& \cdot \left(J_o^2 (b\kappa_1 \cos\theta_1) + J_1^2 (b\kappa_1 \cos\theta_1)\right) \cdot \exp\left(i\kappa_1 d_1 + i\kappa_2 d_2 + i\kappa_2 \bar{d}_2 + i\kappa_1 \bar{d}_1\right)
\end{aligned}
$$

where, as shown in Figure 2a, a is the radius of the transducer, b is the radius of the hole, v_o is the amplitude of the uniform normal velocity over the transducer face produced when the transducer is acting as a transmitter, T_{12}, T_{21} are plane wave transmission coefficients from medium 1 to medium 2, and medium 2 to medium 1, respectively, with the appropriate incident angle denoted as the argument, i.e.,

$$T_{12}\left(\frac{\pi}{2}\right) = \frac{2\rho_1 c_1}{\rho_1 c_1 + \rho_2 c_2} \qquad (7a)$$

$$T_{12}(\theta_1) = \frac{2\rho_1 c_1 \sin\theta_2}{\rho_2 c_2 \sin\theta_1 + \rho_1 c_1 \sin\theta_2} \qquad (7b)$$

$$T_{21}\left(\frac{\pi}{2}\right) = \frac{2\rho_2 c_2}{\rho_1 c_1 + \rho_2 c_2} \tag{7c}$$

$$T_{21}(\bar{\theta}_2) = \frac{2\rho_2 c_2 \sin\bar{\theta}_1}{\rho_1 c_1 \sin\bar{\theta}_2 + \rho_2 c_2 \sin\bar{\theta}_1} \tag{7d}$$

where ρ_i (i = 1,2) are the densities and c_i (i = 1,2) are the compressional wave velocities for the two media of Figure 2a. The quantities κ_1, κ_2 are wave numbers for longitudinal waves in medium 1 and in medium 2, respectively. The quantity h_1 is the distance in water from the transducer to the interface, i.e., the front surface of the specimen, and h_2 is the metal distance, or the distance from the interface to the hole bottom.

The quantities θ_1, θ_2, d_1, d_2 and R_o are defined for the incident wave from the transducer edge to the hole center, as shown in Figure 2a. These variables are determined as follows: θ_1, θ_2 are the incident angles of the edge wave at the transducer face and at the interface, respectively. These can be determined using a simple ray interpretation and the Snell's Law as

$$h_1 \cos\theta_1 - a \sin\theta_1 + \frac{c_2}{2c_1} \cdot \frac{h_2 \sin 2\theta_1}{\sqrt{1 - \frac{c_2^2}{c_1^2}\cos^2\theta_1}} = 0 \tag{8}$$

and

$$\theta_2 = \cos^{-1}\left(\frac{c_2}{c_1}\cos\theta_1\right) \tag{9}$$

The quantities d_1, d_2 are the distances from the transducer edge to the incident point at the interface (r_I), and from that point to the hole center, respectively. The distance r_I can be obtained from the geometry simply by

$$r_I = h_2 \cot\theta_2 \tag{10}$$

Using this r_I expression, d_1 and d_2 can then be calculated as

$$d_1 = \sqrt{(a - r_I)^2 + h_1^2} \tag{11a}$$

and

$$d_2 = \sqrt{r_I^2 + h_2^2} \tag{11b}$$

Also, R_o is the distance from the virtual source to the hole center. The location of the virtual source (r_v,z_v) can be given by

$$r_v = a - h_1\left[\left(\frac{c_2}{c_1}\right)^2 - 1\right]\frac{\cos^3\theta_1}{\sin^3\theta_1} \tag{12a}$$

$$z_v = h_1 - h_1\left(\frac{c_1}{c_2}\right)\frac{\sin^3\theta_2}{\sin^3\theta_1} \tag{12b}$$

in a coordinate system with the origin at the center of the transducer. Using these values, R_o can be obtained by

$$R_o = \sqrt{r_v^2 + (h_1 + h_2 - z_v)^2} \tag{13}$$

In a similar fashion, $\bar{\theta}_1, \bar{\theta}_2, \bar{d}_1, \bar{d}_2$ and $\bar{R}_o$ are defined for the reflected wave from the hole center to the transducer edge, as shown in Figure 2b. These variables are determined as follows: $\bar{\theta}_1, \bar{\theta}_2$ are the incident angles of the reflected edge wave at the hole face and at the interface, respectively. These angles are related to θ_1 and θ_2 by simply $\bar{\theta}_1 = \theta_1$ and $\bar{\theta}_2 = \theta_2$. $\bar{d}_1, \bar{d}_2$ are the distances from the incident point at the interface ($\bar{r}_I$) to the transducer edge, and from the hole center to that incident point, respectively. From the geometry, we see that $\bar{r}_I = r_I$, $\bar{d}_1 = d_1$, $\bar{d}_2 = d_2$. $\bar{R}_o$ is the distance from the hole center to that of the virtual source, whose location ($\bar{r}_v, \bar{z}_v$) can be given by

$$\bar{r}_v = -h_2\left[1-\left(\frac{c_1}{c_2}\right)^2\right]\frac{\cos^3\bar{\theta}_2}{\sin^3\bar{\theta}_2} \tag{14a}$$

$$\bar{z}_v = h_2 - h_2\left(\frac{c_2}{c_1}\right)\frac{\sin^3\bar{\theta}_1}{\sin^3\bar{\theta}_2} \tag{14b}$$

in a coordinate system where the origin is at the center of the hole. Using these relations, $\bar{R}_o$ is then obtained by

$$\bar{R}_o = \sqrt{(a-\bar{r}_v)^2 + (h_1+h_2-\bar{z}_v)^2} \tag{15}$$

Finally, J_o and J_1 are the Bessel functions of the first kind of order zero and one, respectively.

Special Cases

It is interesting to investigate the results of this model for some important cases and to compare those cases with earlier results by Krautkramer [4] and others [5]. First, consider the following limit:

Case (a): $h_1 = 0,\ h_2 \rightarrow 0$

Physically, this case corresponds to the response from the flat-bottom hole located immediately in front of the transducer in a single medium. In this case, the average velocity $\langle v_z \rangle$ is entirely due to a plane wave which comes directly from the transducer face, since the edge wave contributions vanish [2]. Therefore, Eq. (6) simply becomes

$$\langle v_z \rangle = v_o \left(\frac{b}{a}\right)^2 \tag{16}$$

A comparison of Eq. (16) and Krautkramer's result (Eq. 3) shows that they are identical in form. However, for a piston (i.e., constant velocity) source, the average pressure, $\langle p \rangle$, at the transducer face is not also of this same simple form. In fact, using the results of [1], one can show that in the case under consideration one obtains

$$\langle p \rangle = -\rho\, v_o\, c \left(\frac{b}{a}\right)^2 [\, 1 - \exp(i\kappa a)\,] \tag{17}$$

Thus, strictly speaking, Krautkramer's Eq. (3) is not valid for a piston transducer model. However, as Eq. (16) shows, Krautkramer's form is correct if

we consider the average velocity, $\langle v_z \rangle$, instead of the average pressure. It is for this reason that we have chosen to evaluate the average velocity rather than the average pressure in all our model calculations.

Case (b): $h_1/a \gg 1$ or $h_2/a \gg 1$

This case represent the response from the flat-bottom hole when either the water path or metal distance are large. Under either of these circumstance, Eq. (6) can be reduced to

$$\langle v_z \rangle = v_o \left(\frac{b}{a}\right)^2 T_{12}\left(\frac{\pi}{2}\right) T_{21}\left(\frac{\pi}{2}\right) \exp[\, 2i\, (\, \kappa_1 h_1 + \kappa_2 h_2\,)] \cdot \left[1 - \exp\left[i\omega \left(\frac{\sqrt{(a-r_I)^2 + h_1^2} - h_1}{c_1} + \frac{\sqrt{r_I^2 + h_2^2} - h_2}{c_2} \right) \right] \right]^2 \tag{18}$$

which can be rewritten in the form

$$\begin{aligned} \langle v_z \rangle = {} & v_o\, T_{12}\left(\frac{\pi}{2}\right) T_{21}\left(\frac{\pi}{2}\right) \\ & \cdot \exp(i\kappa_1 h_1 + i\kappa_2 h_2)\, C(h_1, h_2, \kappa_1, \kappa_2, a)\, A_s(\kappa_2, b) \\ & \cdot [\, 2 \exp(i\kappa_1 h_1 + i\kappa_2 h_2)\, C(h_1, h_2, \kappa_1, \kappa_2, a)\, c_2/(-ic_1\kappa_1 a^2)] \end{aligned} \tag{19}$$

where

$$C = \left[1 - \exp\left[i\omega \left(\frac{\sqrt{(a-r_I)^2 + h_1^2} - h_1}{c_1} + \frac{\sqrt{r_I^2 + h_2^2} - h_2}{c_2} \right) \right] \right]$$

is a diffraction coefficient for the transducer, and

$$A_s = \frac{-i\kappa_2 b}{2}$$

is the far-field pulse-echo scattering amplitude for v_z predicted by the Kirchhoff approximation for a circular reflector of radius b. (Note that the minus sign arises because the z-axis is taken in a direction from the transducer to the flaw.) In fact, Eq. (19) is identical in form to that predicted by the measurement model of Thompson and Gray [5].

More specificially, if h_1/a becomes large but h_2/a is fixed, since $r_I << a$ Eq. (19) can be reduced even further to give

$$\langle v_z \rangle = -v_o\, T_{12}\left(\frac{\pi}{2}\right) T_{21}\left(\frac{\pi}{2}\right) \cdot \exp(2i(\kappa_1 h_1 + \kappa_2 h_2)) \cdot \left(\frac{\pi a^2}{\lambda_1 h_1}\right)\left(\frac{\pi b^2}{\lambda_1 h_1}\right) \qquad (20)$$

where λ_i (i = 1, 2) are the wavelengths in the respective media. If h_1/a is fixed but h_2/a becomes large, since $a \sim r_I$, Eq. (19) reduces instead to

$$\langle v_z \rangle = -v_o\, T_{12}\left(\frac{\pi}{2}\right) T_{21}\left(\frac{\pi}{2}\right) \cdot \exp(2i(\kappa_1 h_1 + \kappa_2 h_2)) \cdot \left(\frac{\pi a^2}{\lambda_2 h_2}\right)\left(\frac{\pi b^2}{\lambda_2 h_2}\right) \qquad (21)$$

Eqs. (20) and (21) can be viewed as generalizations of the result found by Krautkramer (Eq. (11)), which corresponds to a small flaw far enough from the

transducer to be in the "spherical-wave" spreading region. We see that the current model appropriately includes the effects of transmission twice through the interface through both the transmission coefficients (T_{12}, T_{21}) and phase terms.

REFERENCE REFLECTOR MODEL AND SYSTEM EFFICIENCY FACTOR

In an actual ultrasonic experiment, the quantity that is usually measured is a voltage versus time, V(t), on an oscilloscope screen. If this voltage signal is digitized and Fourier transformed (typically by a Fast Fourier Transform (FFT)), then it is also possible to directly measure the voltage versus frequency, V(ω). For a linear ultrasonic measurement system we can assume that V(ω) is proportional to the average received velocity, i.e.

$$V(\omega) = \beta(\omega) [\langle v_z \rangle / v_o] \tag{22}$$

where β(ω) is called a system efficiency factor [5]. As pointed out in [2], if a reference experiment is performed under the same system settings as the flat-bottom hole measurements, β(ω) is unchanged so that

$$V_r(\omega) = \beta(\omega) [\langle v_z \rangle_r / v_o] \tag{23}$$

where $V_r(\omega)$ is the received voltage for the reference experiment and $\langle v_z \rangle_r$ is the average velocity from the reference scatterer. If we take the plane interface to be our reference reflector in our immersion testing setup (Figure 1), then $\langle v_z \rangle_r$ is given by [2]:

$$\begin{aligned} \langle v_z \rangle_r = {} & v_o R \exp(2i\kappa_1 h_1) \{ 1 - \exp(i\kappa_1 a^2/h_1) \\ & \cdot [J_o (\kappa_1 a^2/2h_1) - i J_1 (\kappa_1 a^2/2h_1)] \} \end{aligned} \tag{24}$$

where

$$R = (\rho_1 c_1 - \rho_2 c_2) / (\rho_1 c_1 + \rho_2 c_2)$$

is the plane wave reflection coefficient for the interface.

Special Cases

Case (a): $\kappa_1 a^2/h_1 << 1$

In this case the interface is in the far-field spherical wave region of the transducer and Eq. (24) reduces to

$$\langle v_z \rangle_r = -v_o R \left(\frac{i \kappa_1 a^2}{4 h_1} \right) \exp(2i\kappa_1 h_1) \qquad (25)$$

Case (b): $\kappa_1 a^2/h_1 >> 1$

For this situation, the interface is directly in front of the transducer where Eq. (24) gives

$$\langle v_z \rangle_r = v_o R \exp(2i\kappa_1 h_1) \qquad (26)$$

Comparing Eqs. (25), (26) with Krautkramer's results for a perfect reflector (Eqs. (4), (5)), we see that these equations are the generalizations of Krautkramer's results for our immersion testing configuration. Thus Eq. (24) is the extension of the reference reflector behavior to all transducer/plane distances.

Just as Krautkramer suggested that the response of a plane close to the transducer could be used to estimate the reference pressure, p_o, in his

expression, Eq. (24) can be used to obtain the efficiency factor $\beta(\omega)$. This is done by simply dividing the measured voltage, $V_r(\omega)$ by the expression in Eq. (24), i.e.

$$\beta(\omega) = V_r(\omega,h_1) / [<v_z(\omega,h_1)>_r/v_0] \qquad (27)$$

where we have explicitly shown the dependency of both V_r and $<v_z>_r$ on ω and h_1. This division is possible since $<v_z>_r$ is well behaved [2]. Note that $\beta(\omega)$ is independent of h_1 so that in principle the plane reflector can be at any distance from the transducer. However, due to experimental variability, it is often advisable to average a series of $\beta(\omega)$ calculations over different h_1 values [2].

In reference [2], we showed that a measurement of $\beta(\omega)$ through the use of this reference reflector model allowed us to calculate the quantity $V(\omega,h_1)/\beta(\omega)$ for different flat-bottom holes and distances h_1. From Eq. (21) we see that these experimental results are directly comparable to our theoretical flat-bottom hole responses $<v_z(\omega,h_1)>/v_0$. In [2], these results were refered to as single frequency DGS-like curves. In the next section, we will show that "true" DGS curves can also be generated from our models.

TIME DOMAIN DGS CURVES

To obtain "true" DGS curves, which are based on time domain amplitude measurements [3], a different procedure than was used in [2] to obtain single frequency DGS-like curves is needed. The steps in this procedure, which use many of the same ingredients as the single frequency results, are as follows:

1. Acquire the reference time domain waveform from the front surface, digitize it, and compute the reference frequency components $V_r(\omega,h_1)$.
2. Use this measured voltage and reference model results, $\langle \upsilon_z(\omega,h_1)\rangle_r / \upsilon_o$, to compute the efficiency factor, using an averaging process over M measurements, as described previously,

$$\beta(\omega) = \frac{1}{M}\sum_{i=1}^{M} \frac{V_r(\omega, h_{1i})}{\langle \upsilon_z(\omega, h_{1i})\rangle_r/\upsilon_o} \tag{28}$$

3. Multiply $\beta(\omega)$ and the model results for the flat-bottom hole response to produce a "theoretical" voltage versus frequency response, $V_f(\omega,h_1)$:

$$V_f(\omega,h_1) = \beta(\omega)\,[\,\langle \upsilon_z(\omega,h_1)\rangle/\upsilon_o\,] \tag{29}$$

4. Using the inverse FFT, compute a "theoretical" voltage versus time response, $V_f(t,h_1)$:

$$V_f(t,h_1) = \int_{-\infty}^{\infty} V_f(\omega,h_1)\, e^{i\omega t}\, d\omega \tag{30}$$

5. Measure the peak-to-peak values of $V_f(t,h_1)$ and plot these values versus h_1/N, where $N = a^2/\lambda_c$ is the near-field distance for the transducer based on its "center" frequency $\omega_c = 2\pi c_1/\lambda_c$.

In the same fashion, a "theoretical" time-domain DGS curve for the reference reflector can be developed by replacing $\langle v_z \rangle$ by $\langle v_z \rangle_r$ in steps (4) and (5) above.

Figure 3 shows an example of the type of variability that is seen in calculating efficiency factors from a water-steel interface at different distances h_1. Although the general shape of the curves at $h_1/N = 1.0$ and $h_1/N = 3.0$ are very similar, some amplitude differences do occur. Therefore, the averaging process in Eq. (20) tries to account for these differences.

In Figures 4 and 5 time domain DGS curves are plotted for wideband 0.5 inch and 0.25 inch diameter 5 MHz transducers, respectively. Also shown in these figures is the DGS curve (solid line) for the front surface reference. To compare these results with experimental DGS curves for flat-bottom holes, we considered two cases. In the first case (Figure 6a) a 5 MHz wideband transducer of 0.5 inch diameter was used to examine an ASTM E428 4340-5-0038 reference block, which was immersed in water and had a flat-bottom hole of 5/64" diameter with 0.38" metal distance. In the second case (Figure 7) a 5 MHz wideband transducer of 0.25 inch diameter was used to test an ASTM E428 4340-5-0012 reference block, which was immersed in water and had a flat-bottom hole of 5/64" diameter with 0.12" metal distance. (the system efficiency factors for this case were those shown in Figure 3).

Experimental values were obtained for peak-to-peak voltages, in both of these cases, at distances h_1 ranging from the very near-field ($h_1/N \sim 0.1$) to the

far-field ($h_1/N \sim 2.0$). Over this very wide range, as Figures 6a and 7 demonstrate, there is very good agreement between the experimental results and the theoretical DGS curves. It is interesting to compare the "true" DGS curve results of Figure 6a with the corresponding single frequency DGS-like curve (Figure 6b) obtained for the same case in [2] at the center frequency of 5 MHz. The time domain DGS curve has much less structure in the near-field because the time domain DGS curve involves the superposition of many different single frequency curves, which tends to "wash out" the severe dips and peaks, particularly when a wideband transducer is used. The results of Figures 4-7 suggest that the flat-bottom hole model, despite the many assumptions that went into its derivation, represents very well the flat-bottom hole response over all distances. To further illustrate the quality of results that can be obtained with the model, we have reproduced the full time-domain waveforms predicted by the model, for the two ASTM specimens described previously (Figures 8 and 9), at distance $h_1/N = 0.5$ and $h_1/N = 1.0$, respectively. As can be seen from Figures 8 and 9, the model not only adequately represents the peak-to-peak voltage, but also the shape of the entire waveforms as well.

FREQUENCY RESPONSE CURVES

One important application that the flat-bottom hole model might have in practical ultrasonic testing is to reduce the number of experiments needed on actual flat-bottom hole specimens. Thus, tests might be run on a 5/64" diameter hole specimen, for example, verified with the corresponding theoretical curves, and then the corresponding results for, say, a 3/64" diameter hole obtained directly from the appropriate theoretical curves. To guarantee that such a transfer process is valid, it would be useful to have a way of checking that the experimental setup corresponds to the assumptions of the model. One way to perform such a verification would be to compare theoretical and experimental results as a function of frequency at different fixed distance h_1. If good agreement was found for all frequencies, for both near and far-field values of h_1, one could be confident that the model is working properly. Such frequency response curves can also easily be found from the flat-bottom hole model, as will be shown here.

In principle, one can obtain such frequency response curves by measuring $\beta(\omega)$, as before, and then calculating

$$m(\omega,h_1) = V(\omega,h_1)/\beta(\omega) \qquad (31)$$

for fixed h_1 and variable ω. As Eq. (22) shows, this experimental frequency response curve should then be directly comparable to the model values $<v_z(\omega,h_1)>/v_o$. Although this process works well when generating DGS-like curves for fixed frequencies not too far from the transducer center frequency [2],

it fails if $\beta(\omega)$ becomes small at frequencies far-removed from the center frequency since then noise contaminates the division process. This is a well known problem encountered in deconvolution procedures, which the division in Eq. (31) represents [6]. One common way around this problem is to employ a Wiener filter [7], whereby we compute instead the quantity

$$m(\omega,h_1) = \frac{V(\omega,h_1)\,\beta^*(\omega)}{|\beta(\omega)|^2 + n^2} \tag{32}$$

where n is a small stabilizing constant that represents the average noise in the measurement process and ( )* denotes the process of complex conjugation. Rewriting Eq. (32) slightly, we see that we can express $m(\omega,h_1)$ as

$$m(\omega,h_1) = \frac{V(\omega,h_1)}{\beta(\omega)} \frac{|\beta(\omega)|^2}{|\beta(\omega)|^2 + n^2} \tag{33}$$

which shows explicitly that $m(\omega)$ is simply the original "ideal" ratio V/β multiplied by a Wiener filter, $W(\omega)$, given by

$$W(\omega) = \frac{|\beta(\omega)|^2}{|\beta(\omega)|^2 + n^2} \tag{34}$$

Figures 10-12 give the results for such filtered frequency response curves at distances $h_1/N = 0.4$, 1.0 and 3.0, respectively. Also shown are the theoretical curves $\langle v_z \rangle / v_o$ for the flat-bottom hole. In this case the hole had a 5/64" diameter and was in the ASTM 4340-5-0012 block mentioned previously. The

transducer used again was a broadband 5 MHz, 0.25" diameter probe. It can easily be seen that the theoretical and experimental curves agree only over a very limited range of frequencies. However, to legitimately make this comparison over all frequencies, since the Wiener filter $W(\omega)$ was applied to the experimental results, it should also be applied to the theoretical results. Thus also shown in Figures 10-12 are curves corresponding to the filtered theoretical values

$$m_T(\omega,h_1) = [<v_z(\omega,h_1)>/v_o] \cdot W(\omega) \qquad (35)$$

Such filtered results then agree much better over all frequencies even though there are large changes occuring in the frequency behavior from the near to far-field. Again, the quality of these results suggests that the model is performing very well indeed.

CONCLUSIONS

We have demonstrated that the flat-bottom hole model developed in [2] is capable of producing theoretical time domain DGS diagrams and frequency response curves that compare well with experiments, even in the near-field. The model, therefore, generalizes the Krautkramer model to a practical immersion testing geometry where no limitation is placed on the distance between the transducer and the hole. Similarly, we have shown that the definition of a system efficiency factor and modern deconvolution procedures can generalize the original Krautkramer procedures significantly. The model, although it is based on a number of strong assumptions, appears to capture all the essential physics of the transmission, scattering and reception processes for this geometrical arrangement. Thus, we feel it may be possible to reliably use the model as a theoretical "standard" for a variety of sensitivity, calibration, and sizing tasks. Currently, we are exploring such areas where the model may serve as a practical new tool for ultrasonic testing.

ACKNOWLEDGEMENTS

S. J. Song and L. W. Schmerr were supported in this work by the Center for Nondestructive Evaluation at Iowa State University. This work also supported, for A. Sedov, by the National sciences and Engineering Research Council of Canada.

REFERENCES

1. L. W. Schmerr and A. Sedov, "The flat-bottom hole: an ultrasonic scattering model." Research in Nondestructive Evaluation, Vol. 1, pp. 181-196, 1989.

2. A. Sedov, L. W. Schmerr, and S. J. Song, "Ultrasonic scattering of a flat-bottom hole in immersion testing: an analytical model." to appear in Journal of Acoustical Society of America.

3. J. Krautkramer, "Determination of the size of defects by the ultrasonic impulse echo method." British Journal of Applied Physics, Vol. 10, pp. 240-245, 1954.

4. J. Krautkramer and H. Krautkramer, Ultrasonic Testing of Materials, 3rd Edition, New York: Springer-Verlag, 1983.

5. R. B. Thompson and T. A. Gray, "A model relating ultrasonic scattering measurements through liquid-solid interfaces to unbounded medium scattering amplitudes." Journal of Acoustical Society of America, Vol. 74, pp. 1279-1290, 1983.

6. A. R. Davies, "On the maximum likelihood regularization of Fredholm convolution equations of the first kind." in Treatment of Integral Equations by Numerical Models, pp. 95-105, Eds. C. T. H. Baker and G. F. Miller, New York: Academic Press, 1982.

7. Y. B. Murakami, B. T. Khuri-Yakub, G. S. Kino, J. M. Richardson, and A. G. Evans, "An application of Wiener filters to nondestructive evaluation." Applied Physics letters, Vol. 33, pp.685-687, 1978.

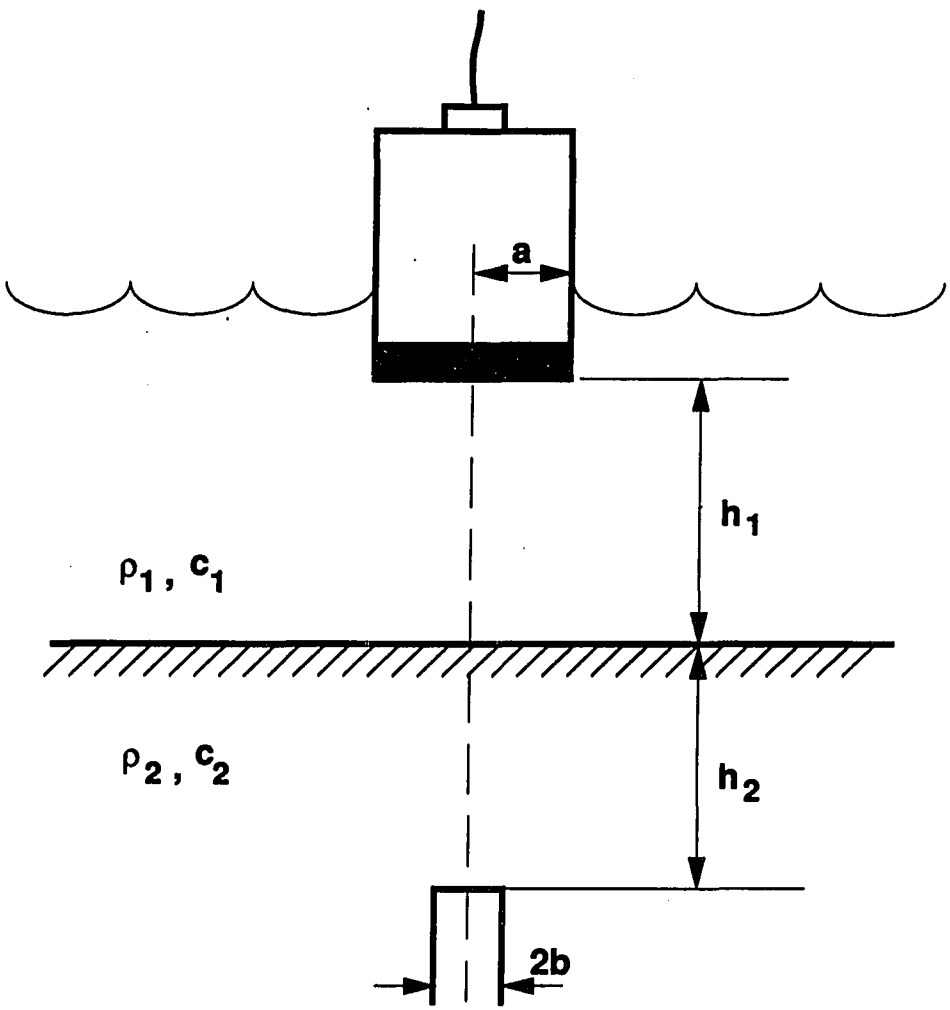

Figure 1. Immersion testing geometry

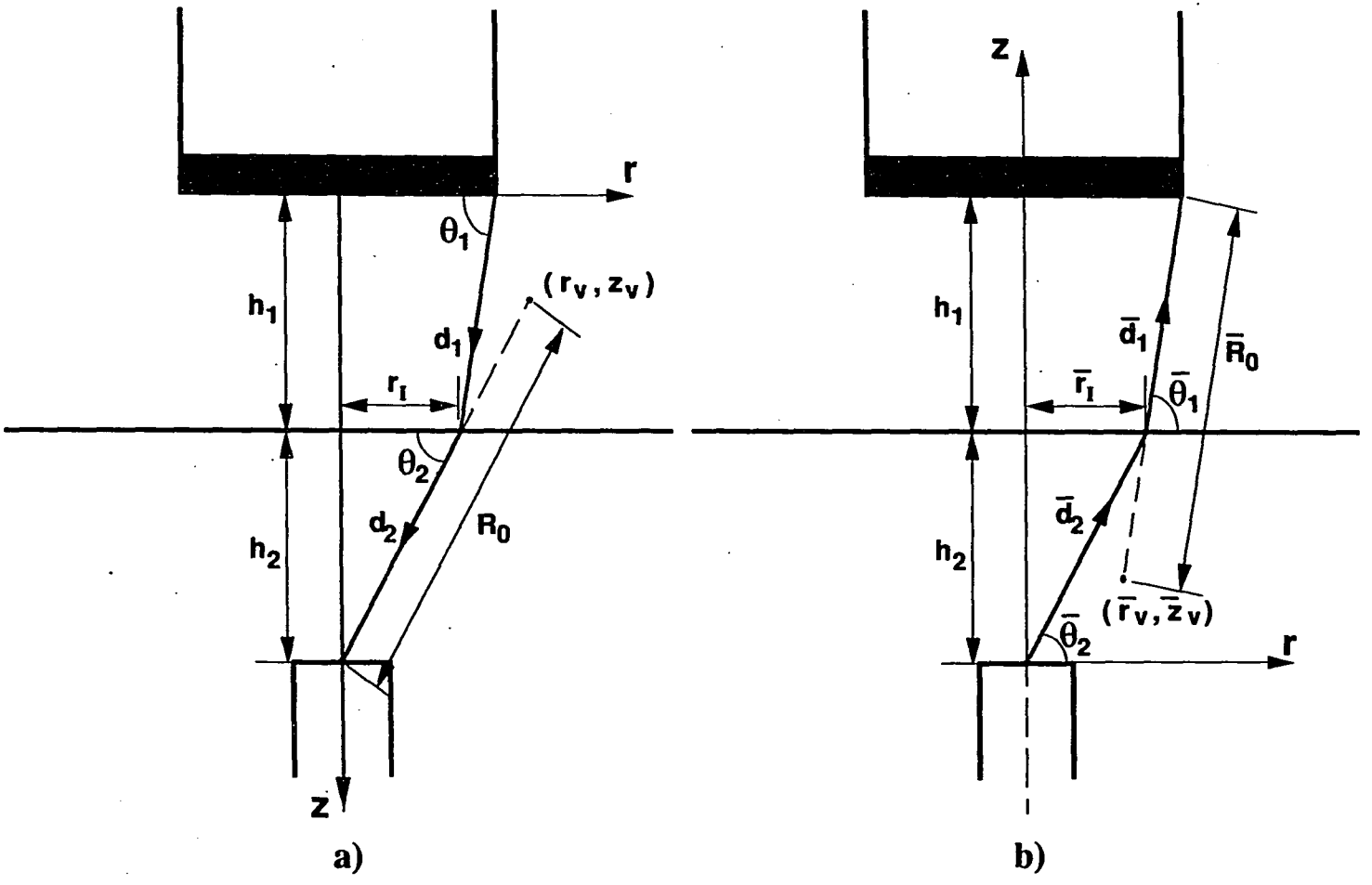

Figure 2. Model parameters for (a) transmitted waves and (b) received waves

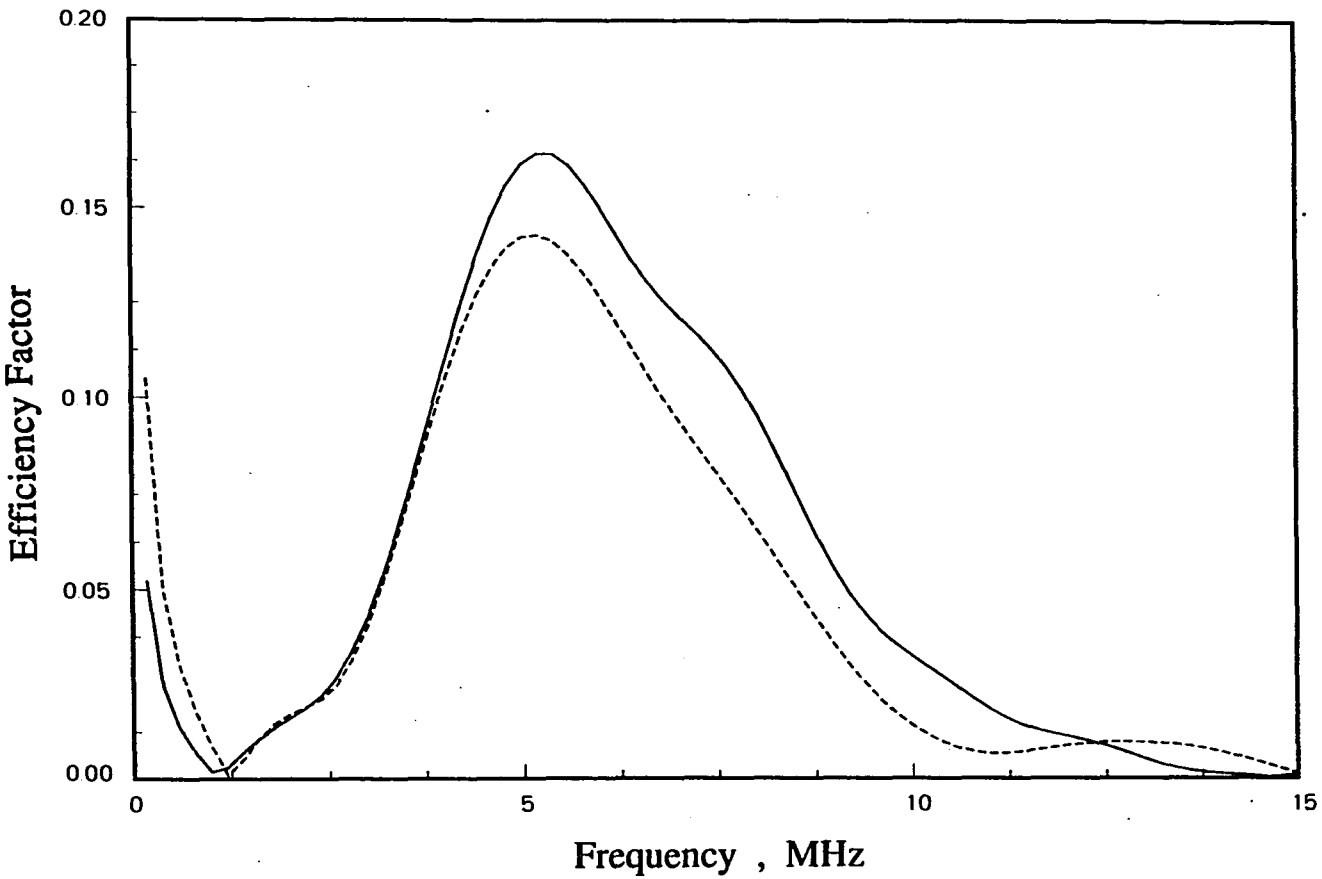

Figure 3. Transducer efficiency factor measured from the front surface reflection; transducer: 5 MHz, 0.25 inch diameter, $h_1/N = 1.0$ (solid line), $h_1/N = 3.0$ (dashed line).

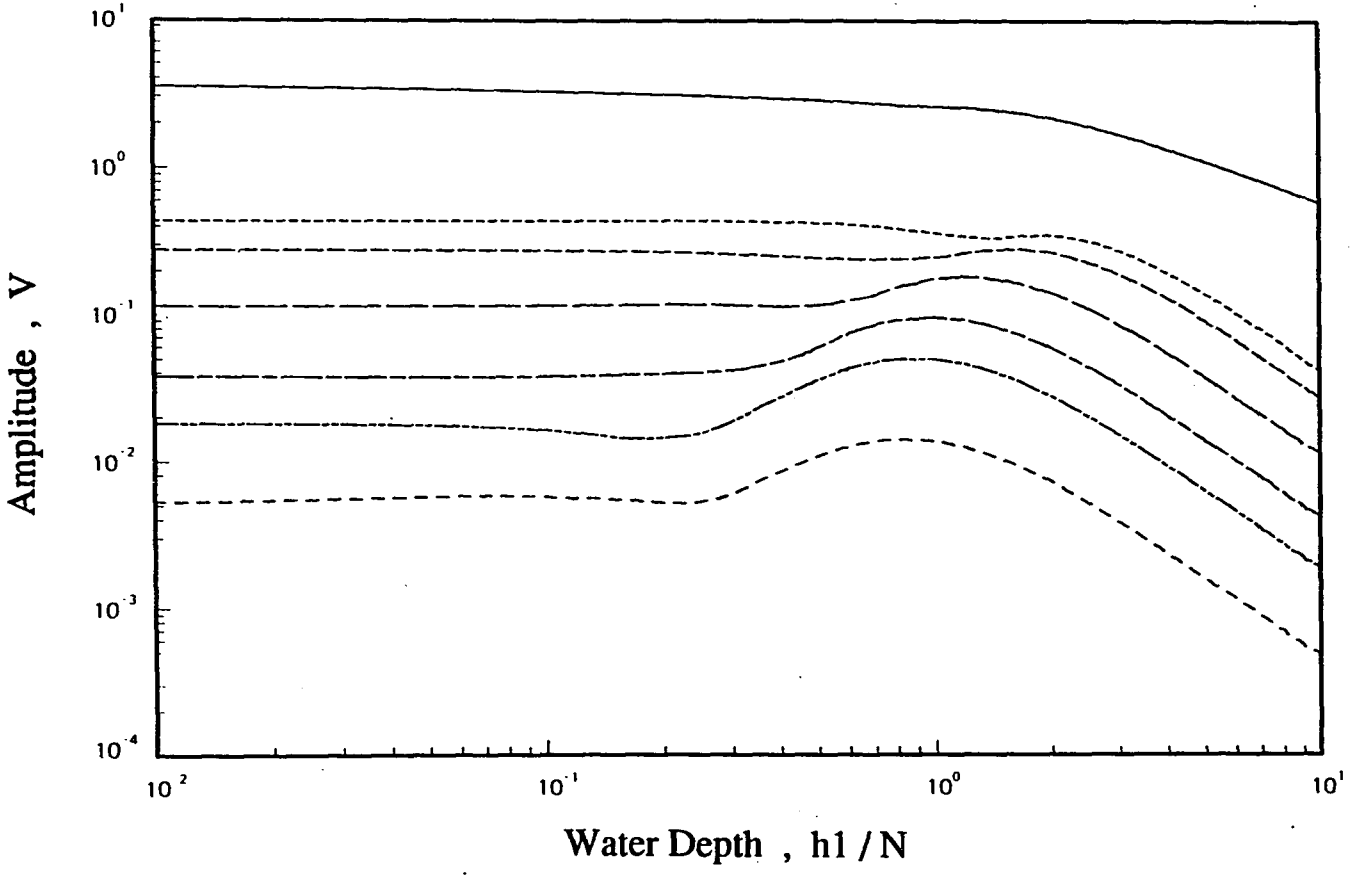

Figure 4. Time domain DGS diagram of flat-bottom holes in steel immersed in water; metal distance (h_2): 0.38 inch, transducer: 5 MHz, 0.5 inch diameter, solid line: front surface reflection, dashed lines: for b/a = 1.0, 0.8, 0.5, 0.3, 0.2, 0.1 respectively, from the top.

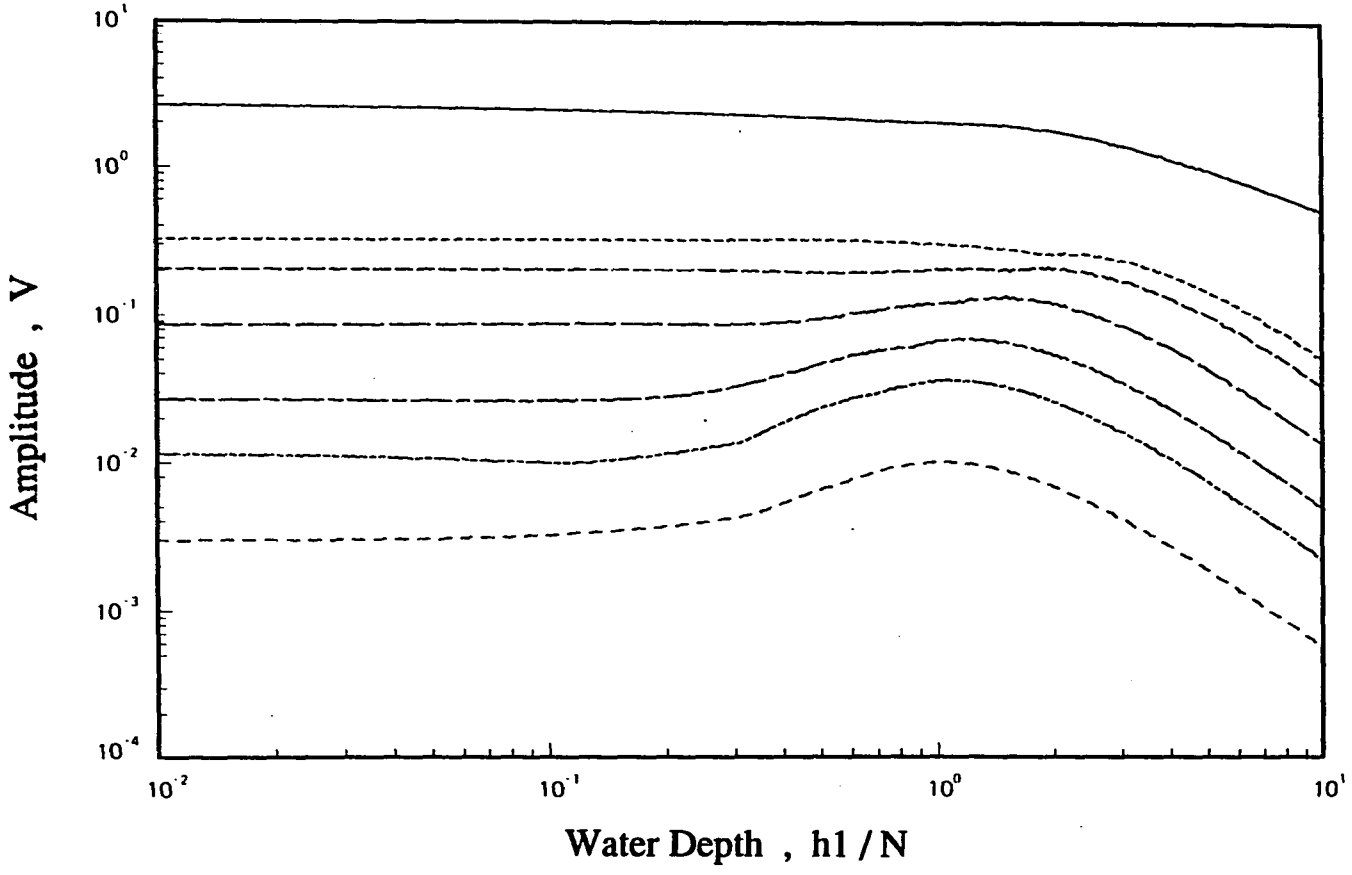

Figure 5. Time domain DGS diagram of flat-bottom holes in steel immersed in water; metal distance (h_2): 0.12 inch, transducer: 5 MHz, 0.25 inch diameter, solid line: front surface reflection, dashed lines: for b/a = 1.0, 0.8, 0.5, 0.3, 0.2, 0.1 respectively, from the top.

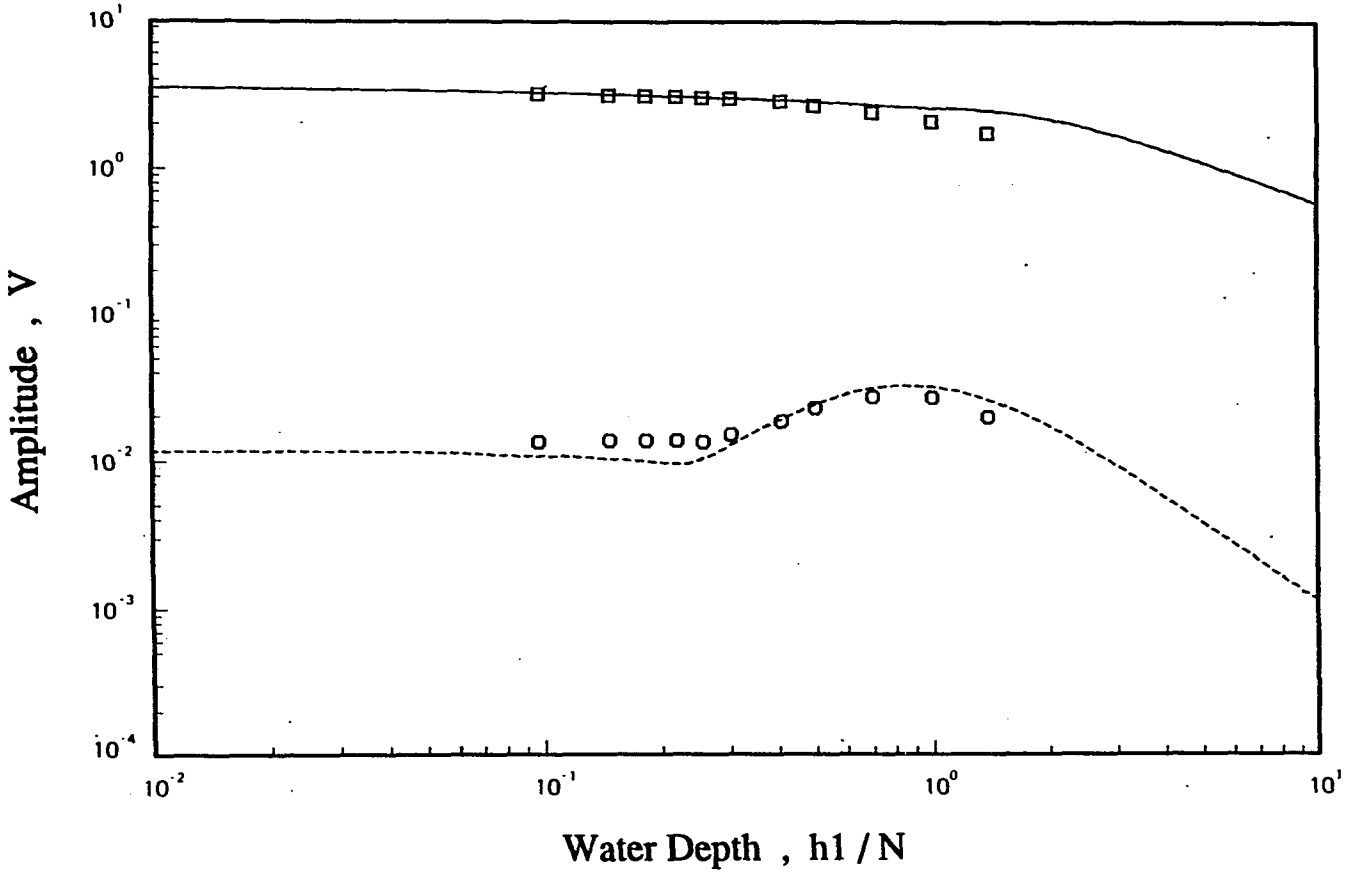

Figure 6a. Time domain DGS diagram of the flat-bottom hole in an ASTM 4340-5-0038 reference block immersed in water; metal distance (h_2): 0.38 inch, transducer: 5 MHz, 0.5 inch diameter, b/a = 0.156, Reference (solid line), FB hole (dashed line).

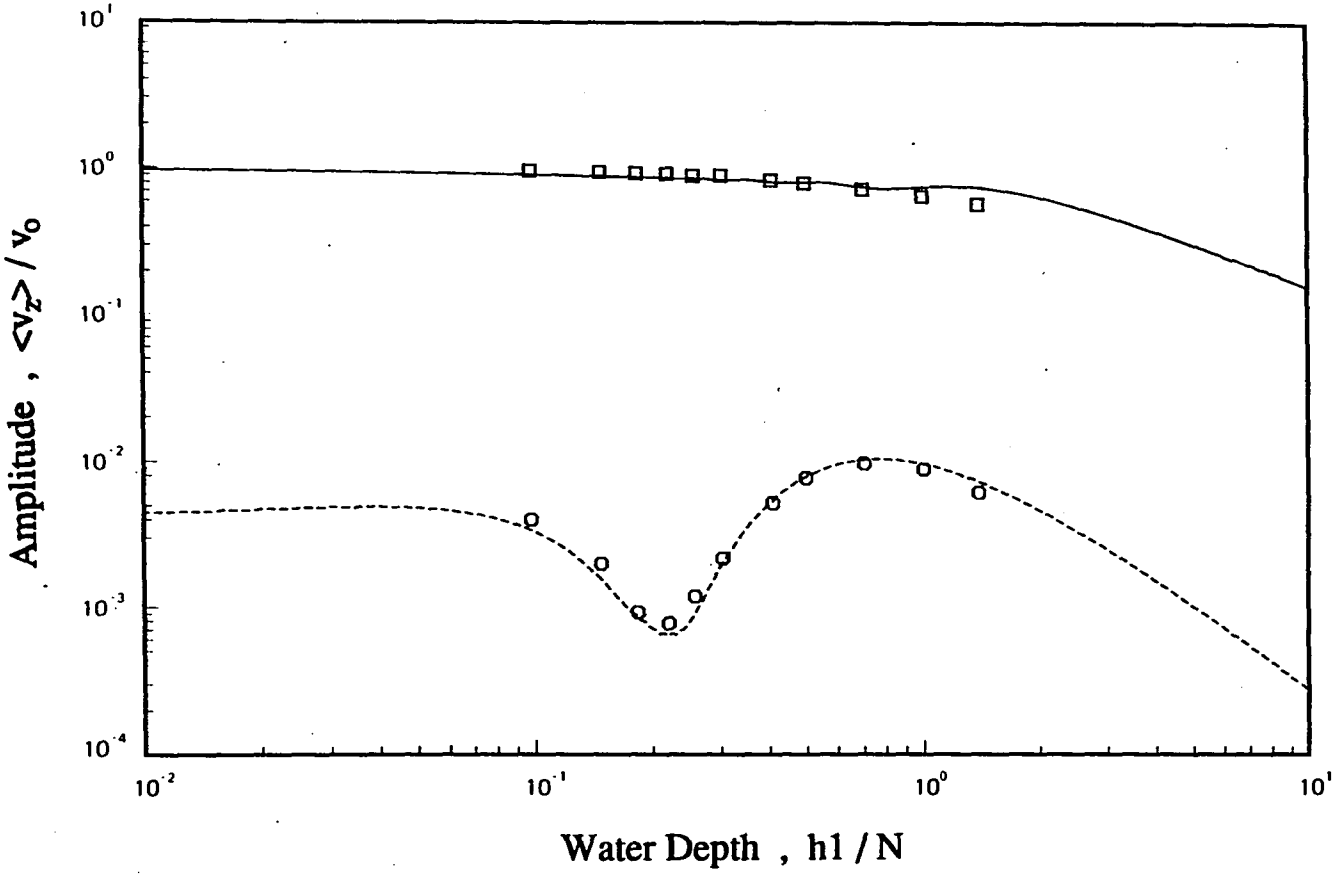

Figure 6b. Single frequency DGS diagram (at 5 MHz) of the flat-bottom hole in an ASTM 4340-5-0038 reference block immersed in water; metal distance (h_2): 0.38 inch, transducer: 5 MHz, 0.5 inch diameter, b/a = 0.156, Reference (solid line), FB hole (dashed line).

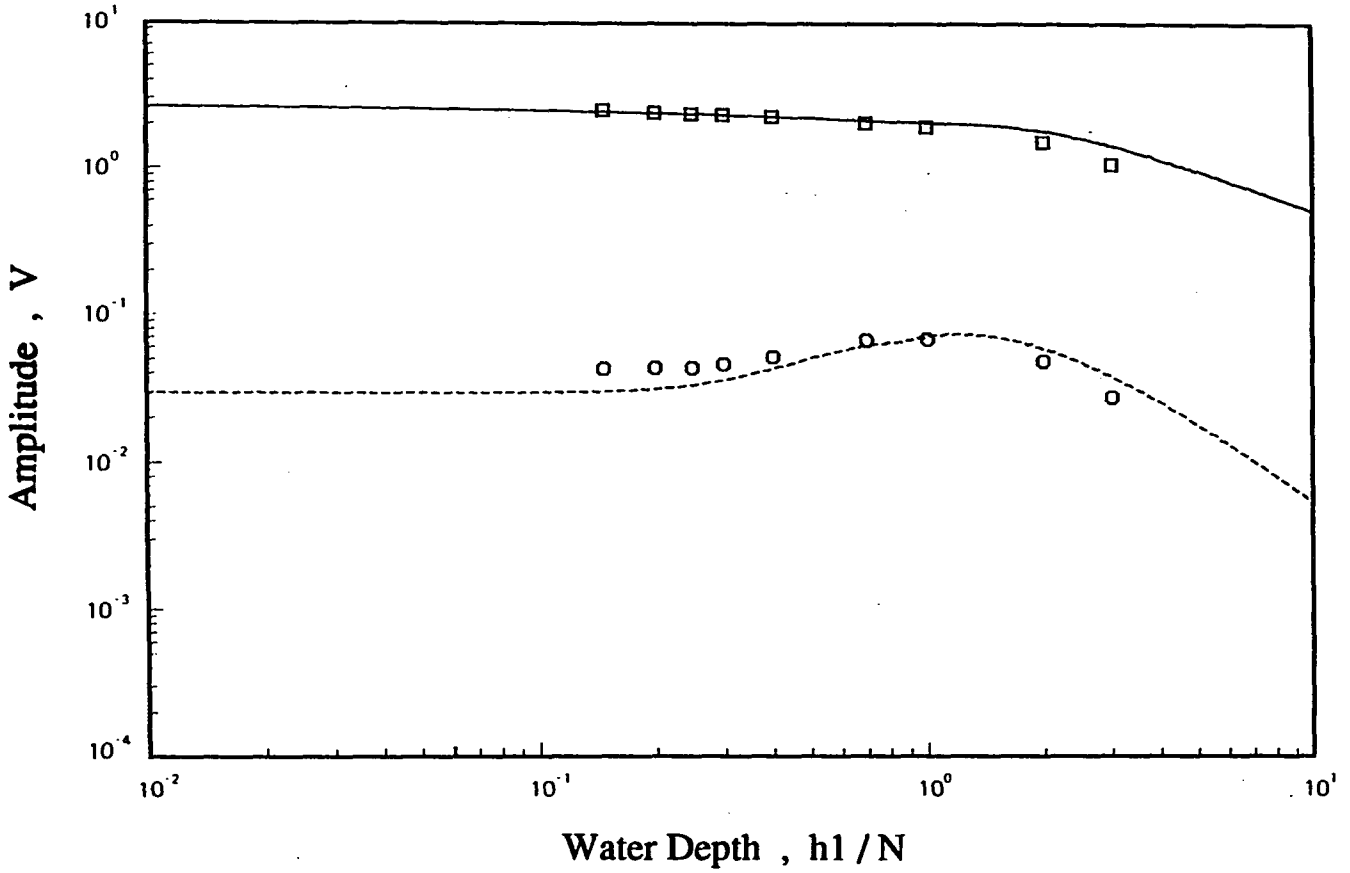

Figure 7. Time domain DGS diagram of the flat-bottom hole in an ASTM 4340-5-0012 reference block immersed in water; metal distance (h_2): 0.12 inch, transducer: 5 MHz, 0.5 inch diameter, b/a = 0.313, Reference (solid line), FB hole (dashed line).

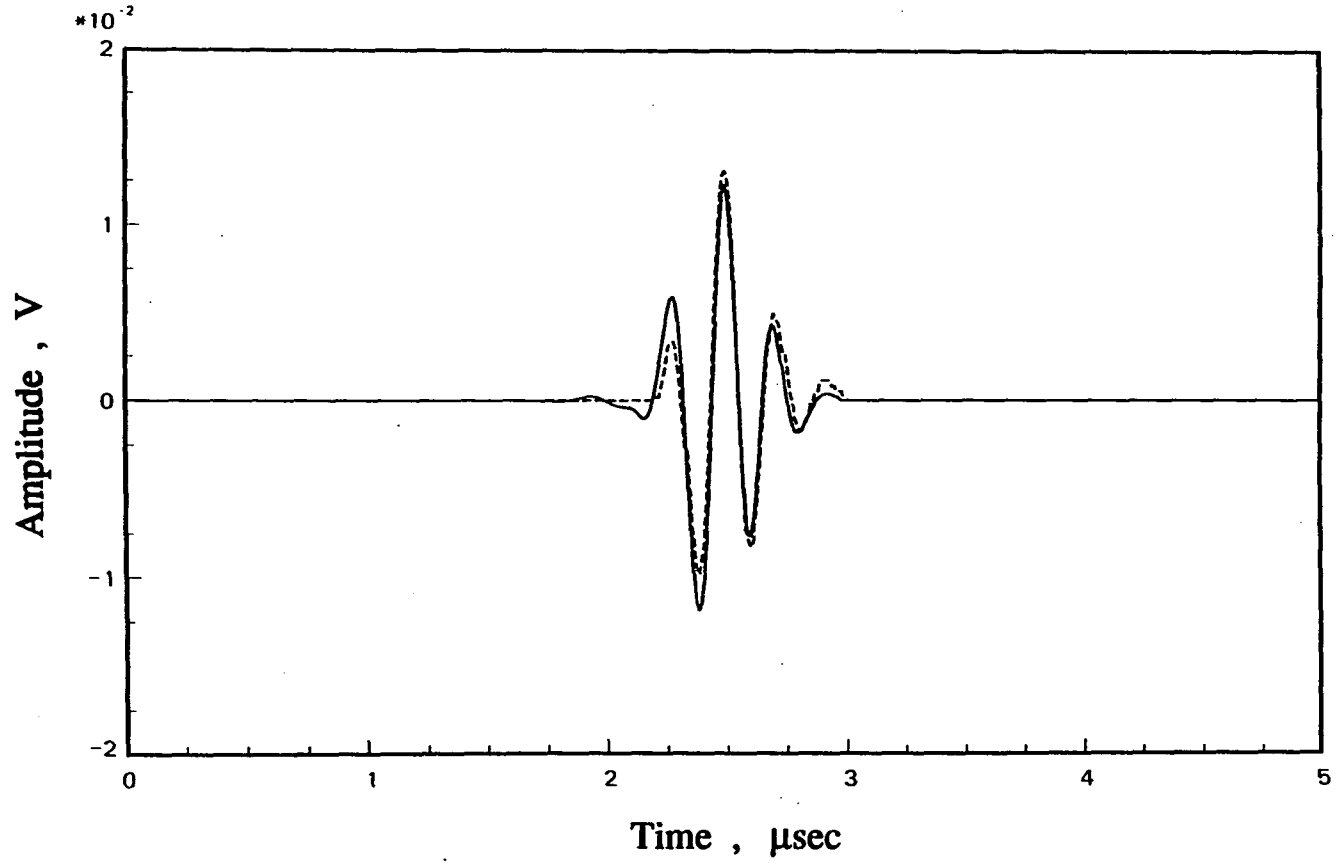

Figure 8. Time domain signal reflected from the flat-bottom hole in an ASTM 4340-5-0038 reference block immersed in water; transducer 5 MHz, 0.25 inch diameter, b/a = 0.156, $h_1/N = 0.5$, Theory (solid line), Experiment (dashed line).

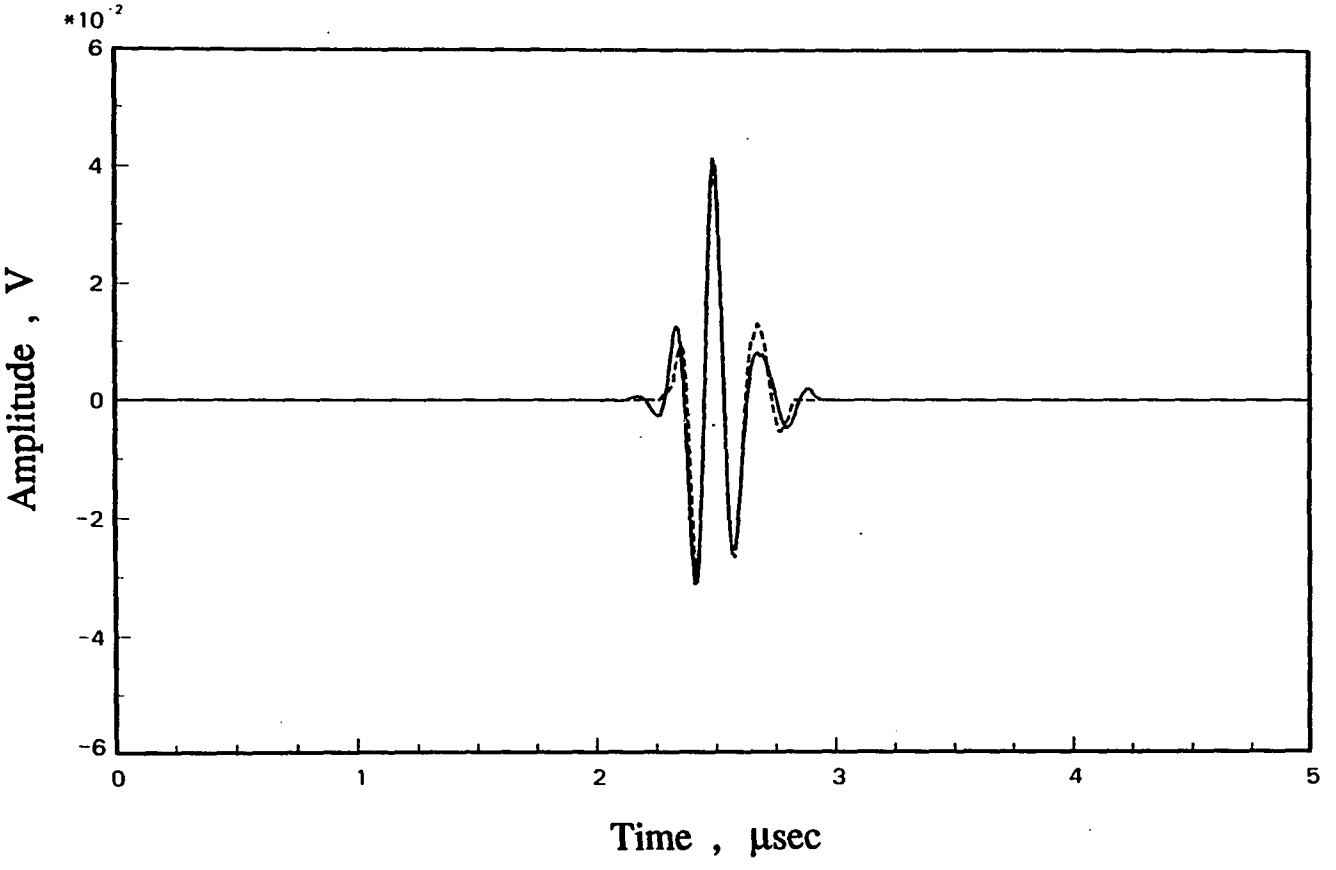

Figure 9. Time domain signal reflected from the flat-bottom hole in an ASTM 4340-5-0012 reference block immersed in water; transducer 5 MHz, 0.25 inch diameter, b/a = 0.313, $h_1/N = 1.0$, Theory (solid line), Experiment (dashed line).

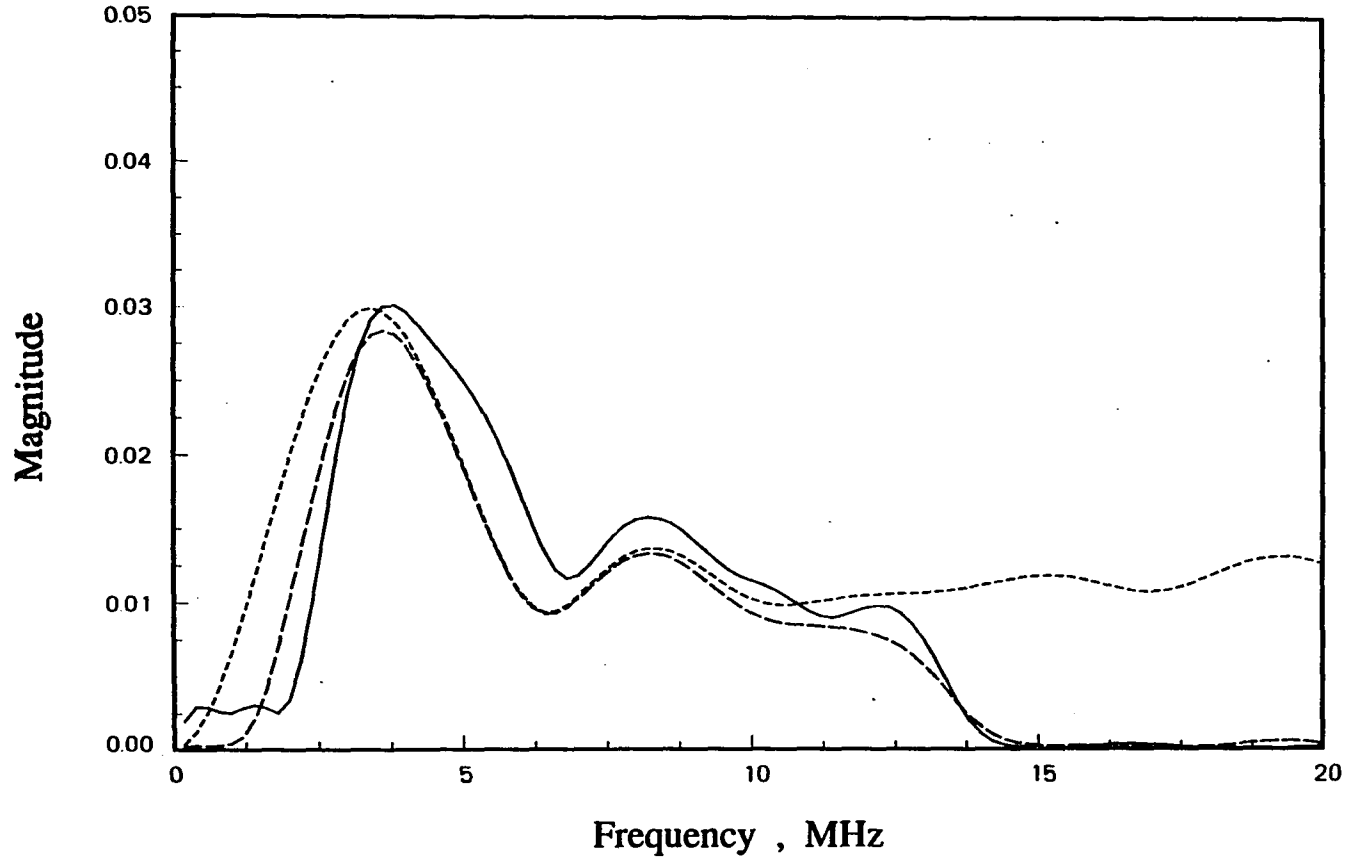

Figure 10. Frequency response of the flat-bottom hole in an ASTM 4340-5-0012 reference block immersed in water; transducer 5 MHz, 0.25 inch diameter, $h_1/N = 0.4$, Experiment (solid), Theory (short dashes), Theory w/filter (long dashes).

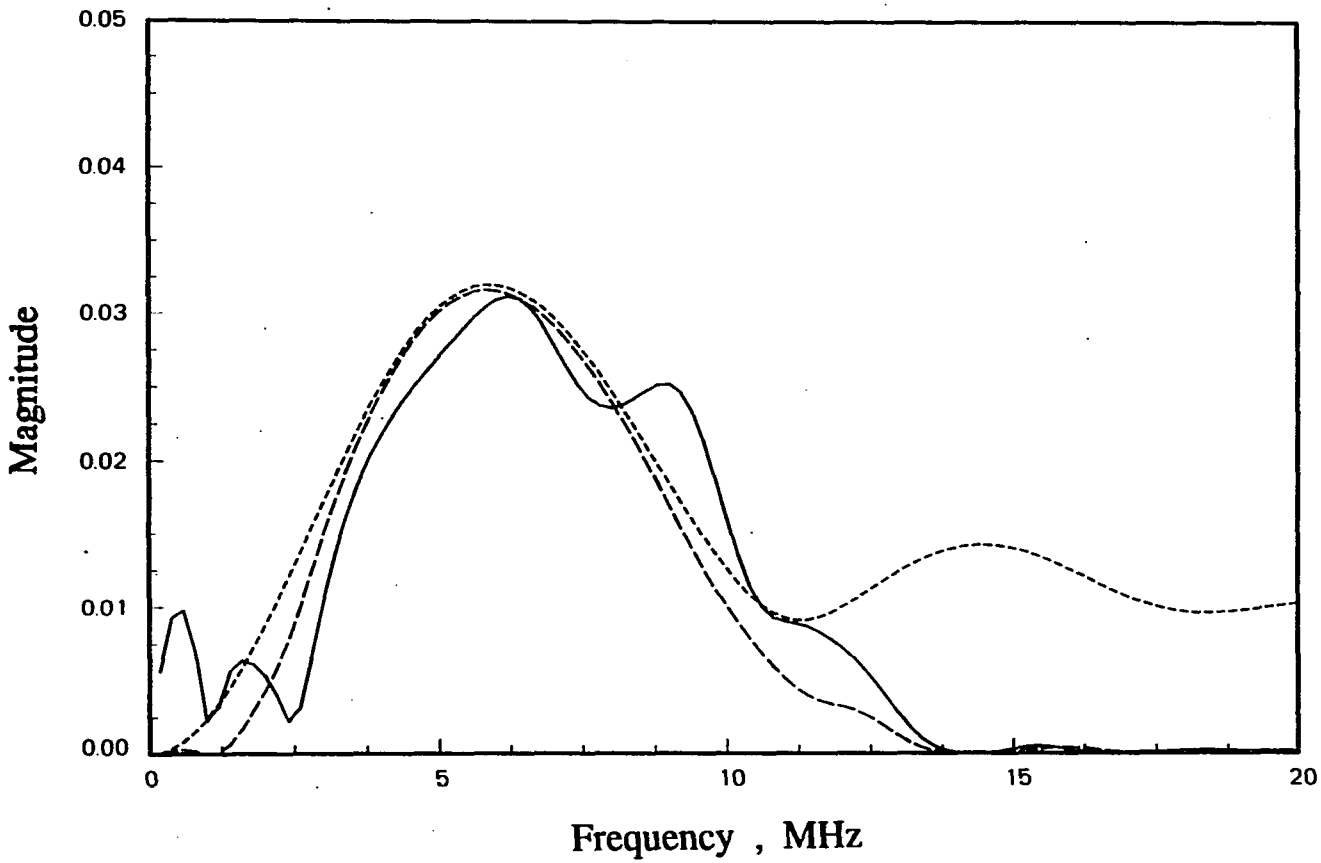

Figure 11. Frequency response of the flat-bottom hole in an ASTM 4340-5-0012 reference block immersed in water; transducer 5 MHz, 0.25 inch diameter, $h_1/N = 1.0$, Experiment (solid), Theory (short dashes), Theory w/filter (long dashes).

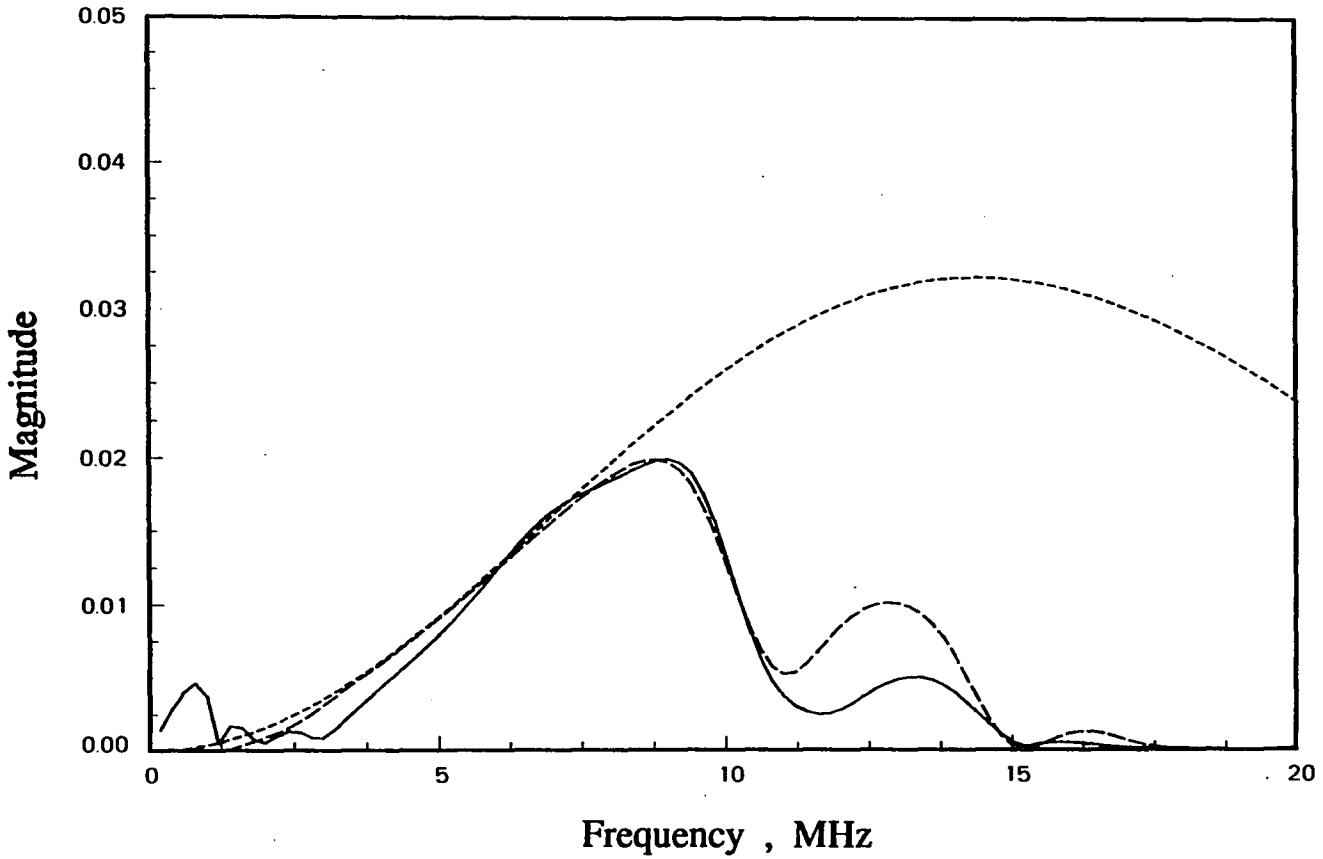

Figure 12. Frequency response of the flat-bottom hole in an ASTM 4340-5-0012 reference block immersed in water; transducer 5 MHz, 0.25 inch diameter, $h_1/N = 3.0$, Experiment (solid), Theory (short dashes), Theory w/filter (long dashes).

PART III. AN ULTRASONIC TIME-OF-FLIGHT EQUIVALENT FLAW SIZING METHOD

An ultrasonic time-of-flight equivalent flaw sizing method

Sung-Jin Song and Lester W. Schmerr

Center for NDE and
Department of Aerospace Engineering and Engineering Mechanics

Iowa State University

Ames, Iowa 50011

ABSTRACT

One of the challenging tasks in the field of ultrasonic NDE is to obtain quantitative flaw size, shape and orientation information. In an equivalent flaw sizing approach, flaws in a material are reconstructed in terms of a best-fit simple shape such as an ellipsoid or ellipse. In this work, a new time-of-flight equivalent (TOFE) flaw sizing method is developed for obtaining best-fit equivalent flaws from a relatively small number of timing measurements at different transducer orientations. The performance of the method is demonstrated on synthetic numerical data and with experiments, including examples of sizing in anisotropic composite materials and in welds.

INTRODUCTION

Conventional ultrasonic nondestructive evaluation (NDE) techniques have served for many years as an effective tool for the detection of flaws. These methods have been less effective, however, for the determination of the shape, size and orientation of flaws. Information of this type is essential in modern structural integrity evaluations using, for example, fracture mechanics. A wide variety of ultrasonic flaw sizing approaches [1,2,3] have been developed including amplitude-based and time-of-flight methods, detailed imaging methods, and equivalent sizing methods.

Most conventional methods use only the amplitude information of ultrasonic signals for flaw sizing. One example is the use of Distance-Gain-Size (DGS) curves to size flaws in terms of equivalent flat bottom holes [4,5]. Even though this scheme has a wide variety of applications, it is restricted to flaws smaller than the beam size of a transducer. For sizing relatively large flaws, echo dynamic patterns [6,7] can be used, based on mapping the amplitude variation as a function of position of a transducer scanning over a flaw. Unfortunately, these conventional schemes often cannot produce the size information needed for fracture mechanics calculations [8,9].

Errors in conventional flaw sizing methods mostly result from their strong reliance on amplitude information only. Some methods attempt to avoid these limitations by using time-of-flight information instead or a combination of time-of-flight and amplitude information. The Time-of-Flight Diffraction (TOFD) method [10,11] and the Satellite-Pulse technique [12,13] are examples of this approach.

The TOFD method uses the waves diffracted from the tips of a crack as the basis for sizing. In the most common configuration of this method, a transmitter and a receiver are placed separately around a suspect crack position, and the signals diffracted from the upper and lower tips of the crack are identified. The length of the crack can then be computed from the time difference between these two diffracted waves. This technique can be applied in several geometries, and can use both bulk waves and Rayleigh waves. A detailed discussion of this method can be found in [14]. The Satellite-Pulse technique is quite similar in principle to the TOFD method in the case of sizing planar crack-like flaws but uses a single transducer. This method has also been applied to sizing volumetric void-like flaws using the time difference between the specular reflection and the following creeping wave. Even though these techniques have achieved sucesses in some applications, they still have some important limitations in the information they extract about flaw geometry. For example, both the TOFD method and the Satellite-Pulse technique typically locate only the extreme borders of a flaw from one transducer orientation. Often this is not sufficient information to determine a flaw shape and orientation without making some very strong a priori assumptions.

To extract more complete information about flaw geometry, various detailed imaging techniques [15] have been developed. In general, techniques in this category can be divided into three subgroups; intensity mapping methods, pulse-echo imaging methods, and phase-amplitude imaging methods.

Intensity mapping methods produce a two-dimensional map of the transmission of sound through an object using amplitude information only. Sound is transmitted through an object and the intensity of sound on the other

side is measured as a function of lateral position. Then the image of flaws can be obtained as the resulting intensity map. The scanning acoustic microscope [16] is one of the practical applications of this concept. Most acoustical imaging methods currently used in NDE fall under the general category of the pulse-echo techniques, which extensively use combinations of amplitude and time-of-flight information. Conventional B-scan and C-scan methods are most common examples of these techniques. Among some advanced methods in this category, there are the synthetic aperture focusing technique (SAFT) [17,18] and the amplitude and transit time locus curves (ALOK) [19]. In addition to the amplitude and the time-of-flight information of ultrasonic signals, the phase information of these signals also can be used for sizing. Acoustical holography [20] is a typical example of such phase-amplitude imaging techniques.

Naturally, most of these ultrasonic imaging methods require detailed scanning and considerable data processing, thus they take time to get final information about flaw geometries.

In between the two extremes of conventional methods and detailed scanning methods, there is a model-based approach called equivalent flaw sizing [21,22,23]. In this method, flaws are reconstructed in terms of "best-fit" equivalent ellipsoids (for volumetric flaws) or ellipses (for cracks) obtained from a relatively small number of ultrasonic measurements at different transducer orientations and locations. Previous work in this area has shown that it is a viable sizing scheme provided that the location of the center of the flaw can be found and the equivalent flaw "radius" estimated at different transducer "look-angles" [24,25]. This information is normally obtained directly

from the ultrasonic waveform itself, using models based on the Born or Kirchhoff approximations and signal processing methods [21-25].

Here, we will demonstrate that for relatively large flaws all the information required to perform equivalent flaw sizing can be obtained from a few time-of-flight measurements made at different transducer locations and orientations. We refer to this new sizing method as the time-of-flight equivalent (TOFE) sizing method. First, we will briefly review the equivalent flaw sizing method used previously for small flaws and describe how the concepts can be extended to TOFE sizing for large flaws. The performance of the TOFE method will be demonstrated on both synthetic and experimental data. In the latter case, examples will be given for sizing flaws in both composite materials and in weldments.

EQUIVALENT FLAW SIZING

Our new TOFE sizing method is an extension of existing equivalent flaw sizing methods to relatively large flaws. Thus in this section, some key aspects of current equivalent flaw sizing techniques will be mentioned briefly, including some very recent enchancements [25].

Key Issues

As mentioned previously, ultrasonic equivalent flaw sizing is an approach which determines a "best-fit" simple geometry that is able to represent the major aspects of the flaw. This approach has been developed based on ultrasonic scattering models such as the Born approximation for volumetric flaws [21,22] or the Kirchhoff approximation for cracks [23]. Recently, a unified algorithm that can be applied to both volumetric flaws and cracks has been developed by Schmerr et al. [24].

The basic parameter that must be found in most equivalent flaw sizing methods is the the equivalent flaw radius, r_e, which is the distance from the flaw centroid to the front surface tangent plane (where the incident wavefront (assumed plane) first touches the flaw). For an ellipsoid, r_e, is determined by three factors; the flaw size parameters (a,b,c), the flaw orientation parameters ($\underline{e}_a$, $\underline{e}_b$, $\underline{e}_c$), and a known incident wave direction ($\underline{e}_q$) (Figure 1a). Specifically, for an ellipsoid we have:

$$(1) \qquad r_e = [\, a^2(\underline{e}_q \cdot \underline{e}_a)^2 + b^2(\underline{e}_q \cdot \underline{e}_a)^2 + c^2(\underline{e}_q \cdot \underline{e}_c)^2 \,]^{\frac{1}{2}}$$

The relationship of Eq. (1) is also true for the case of an elliptical flat crack with one semi-radius, say c, taken equal to zero. Once a number of equivalent radius data at different incident wave angles are available, this information can be used, as will be shown shortly, to obtain the best-fit flaw geometry. Hence, most equivalent flaw sizing schemes currently involve: 1) the measurement of the scattered waveforms from a number of different transducer orientations, 2) the extraction of the equivalent radius, r_e, from these waveforms, and 3) the determination of the best-fit ellipsoid, using Eq. (1), that matches the measured r_e data.

Accurate measurement of the equivalent radius is the one of the most crucial steps in the equivalent flaw sizing method. Once this is done, determination of the best-fit flaw parameters can be obtained in a straightforward manner. Most of the difficulties associated with obtaining r_e accurately are connected to the difficulty in measuring the absolute phase of the ultrasonic response accurately with respect to some fixed spatial location (also called the zero-of-time problem). [26]. To solve this problem various approaches, such as the area function method [27], low frequency extrapolation [28], and the flash point distance measurement [24] have been developed, but all of those schemes still have some difficulty in practical applications. Recently, Song and Schmerr [29] proposed a new approach, the first moment method, which has shown very good performance in some initial experimental verifications.

In many previous equivalent flaw sizing schemes, a nonlinear optimization approach was used to determine the best-fit flaw geometry from

r_e data. For N measurements of r_e at different transducer orientations ($\underline{e}_q$), one can form up the function

$$(2) \qquad I(a,b,c,\underline{e}_a,\underline{e}_b,\underline{e}_c) = \sum_{i=1}^{N} [\,(r_e^{exp})_i - (r_e^{model}(a,b,c,\underline{e}_a,\underline{e}_b,\underline{e}_c))_i\,]^2$$

and search for the best-fit parameters (a, b, c, $\underline{e}_a$, $\underline{e}_b$, $\underline{e}_c$) that match the measurements, by minimizing the function I. Here $(r_e^{exp})_i$ are the experimentally measured r_e values and $(r_e^{model})_i$ is obtained from Eq. (1). As Chiou and Schmerr [24] have pointed out, solving Eq. (2) is difficult because of the very complicated nonlinear nature of the problem. Fortunately, such difficulty can be avoided entirely through a reformulation of the sizing problem into a two-step procedure [25]. Here we describe briefly that procedure.

Linear Least Squares / Eigenvalue Problem Approach

Instead of using Eq. (1) directly as a nonlinear relation between the equivalent radius r_e and flaw parameters (a, b, c, $\underline{e}_a$, $\underline{e}_b$, $\underline{e}_c$), we can define a linear relationship by relating r_e^2 to a set of six C parameters as

$$(3) \qquad r_e^2 = C_{xx}L_x^2 + C_{yy}L_y^2 + C_{zz}L_z^2 + 2C_{xy}L_xL_y + 2C_{xz}L_xL_z + 2C_{yz}L_yL_z$$

where

$$(3.a) \qquad \begin{aligned} L_x &= \cos\theta\cos\phi \\ L_y &= \cos\theta\sin\phi \\ L_z &= \sin\theta \end{aligned}$$

are the Cartesian components of $\underline{e}_q$ in terms of spherical coordinate angles (θ,ϕ) (Figure 1b) and the C-parameters are explicitly given by

$$
\begin{aligned}
C_{xx} &= a^2 a_x^2 + b^2 b_x^2 + c^2 c_x^2 \\
C_{yy} &= a^2 a_y^2 + b^2 b_y^2 + c^2 c_y^2 \\
C_{zz} &= a^2 a_z^2 + b^2 b_z^2 + c^2 c_z^2 \\
C_{xy} &= a^2 a_x a_y + b^2 b_x b_y + c^2 c_x c_y \\
C_{xz} &= a^2 a_x a_z + b^2 b_x b_z + c^2 c_x c_z \\
C_{yz} &= a^2 a_y a_z + b^2 b_y b_z + c^2 c_y c_z
\end{aligned}
\tag{3.b}
$$

in which a, b, c are the three semi-axis sizes and m_x, m_y, m_z (m = a, b, c) are three sets of unit vector components along the three semi-axes. Using Eq. (3) we can form up the function

$$
J(C_{xx}, C_{yy}, \ldots) = \sum_{i=1}^{N} \left[(r_e^{exp})_i^2 - (C_{xx}L_x^2 - C_{yy}L_y^2 - \ldots)_i \right]^2 \tag{4}
$$

and find the best-fit C coefficients that fit the measured data. The advantage of Eq. (4) over Eq. (2) is that now we need only solve a much simpler and well-behaved linear least squares problem.

Once the 6 C's are obtained, a real symetric matric C can be formed as

$$
\underset{\sim}{C} = \begin{bmatrix} C_{xx} & C_{xy} & C_{xz} \\ C_{xy} & C_{yy} & C_{yz} \\ C_{xz} & C_{yz} & C_{zz} \end{bmatrix} \tag{5}
$$

By solving the eigenvalue problem of this matrix C, i.e.

(6) $$\underset{\sim}{C} - \lambda \underset{\sim}{I} = 0$$

all the equivalent flaw parameters can be obtained since the eigenvalues of C are just the squares of the three semi-axis sizes (a^2, b^2, c^2) and the three eigenvectors of C are the corresponding three orientation unit vectors ($\underline{e}_a$, $\underline{e}_b$, $\underline{e}_c$). Chiou and Schmerr [25] have already shown the excellent performance of this approach using both synthetic and experimental data.

TIME-OF-FLIGHT EQUIVALENT FLAW SIZING METHOD

In this section, we will show how the equivalent flaw sizing concept can be combined with simple time-of-flight measurements to produce a new time-of-flight equivalent (TOFE) sizing method. In later experimental verifications, it will be shown that TOFE sizing is indeed a viable method provided that the flaw is relatively large.

The TOFE Sizing Algorithm

In the case of small flaw sizing, experimental determination of the equivalent radius by measuring the absolute phase of the scattered response (or, equivalently the time-of-flight) from the transducer location is not practical, since even small unknown percentage changes in the material wavespeed can introduce errors greater than the flaw size itself. However, for large flaws the distance from the transducer to the front surface tangent plane of a given flaw (H) can be measured with sufficient accuracy from a simple pulse-echo time-of-flight measurement, $\Delta T = 2H/c$, between the transducer location and the front surface of the flaw, where c is the wavespeed in the surrounding medium (Figure 2a). Thus, the TOFE sizing method is a scheme which can determine the best-fit ellipsoid and flaw centroid location simutaneously using just information about this time-of-flight and the transducer location. Like the Linear Least Squares / Eigenvalue approach mentioned above, the TOFE sizing method also involves a two-step approach.

The j-th pulse-echo time-of-flight measurement, $\Delta T^j = 2H^j/c$, for a flaw embedded in a single medium (Figure 2a), can be related to the transducer and flaw parameters through:

$$(7) \qquad (\underline{x}_T^j - \underline{x}_c) \cdot \underline{n}^j = H^j + r_e^j$$

where

$\underline{x}_T^j$ is the location of the transducer for the j-th measurement, $\underline{x}_C$ is the location of flaw centroid, $\underline{n}^j$ is the unit vector parallel to the wave propagation direction for the j-th measurement, H^j is the distance from the transducer to the tangent plane to a flaw for the j-th measurement.

If we place into Eq. (7) the r_e relation of Eq. (3), which can be written using the matrix C of Eq. (5) as

$$(8) \qquad (r_e^j)^2 = \underline{n}^j \cdot \underset{\sim}{C}\, \underline{n}^j$$

we can show that

$$(9) \qquad \begin{aligned} F_j &= (\underline{x}_c \cdot \underline{n}^j)^2 - 2(\underline{x}_T^j \cdot \underline{n}^j - H^j)(\underline{x}_c \cdot \underline{n}^j) - \underline{n}^j \cdot \underset{\sim}{C}\, \underline{n}^j + (\underline{x}_T \cdot \underline{n}^j - H^j)^2 \\ &= 0 \end{aligned}$$

where F_j is a nonlinear function of the location of a flaw centroid, $\underline{x}_C$, and a linear function of the six C parameters of Eq. (5). However, the nonlinearity in this function is of a simple quadratic form so that as a first step we can still use it to define a well behaved optimization problem. This optimization problem, for N measurements of transducer locations $\underline{x}_T^j$ and directions $\underline{n}^j$, is to form up the function

$$(10) \qquad I(\underline{x}_c, \underline{\underline{C}}) = \sum_{j=1}^{N} [F_j(\underline{x}_c, \underline{\underline{C}}, \underline{x}_T^j, \underline{n}^j)]^2$$

and find the 9 best-fit parameters (the flaw centroid location $\underline{x}_C$, and the 6 indirect parameters, C_{xx}, C_{yy}, C_{zz}, C_{xy}, C_{xz}, C_{yz}) by solving the non-linear optimization problem. Here, we see that the information about flaw centroid location is separated from the flaw size parameters and determined explicitly.

Thus, the TOFE sizing method does not require an apriori estimate of this location and hence does not suffer from the zero-of-time problem. However, since the TOFE sizing method uses time-of-flight measurements to estimate the distance parameters appearing in Eq. (9), it is essential that the wavespeed be determined accurately or the TOFE sizing method will produce unacceptably large errors. For example, if there is an error Δc in the measurement of the wavespeed over a path length H then there will be an error in the estimation of the flaw surface location given by $\Delta H = (\Delta c/c)\, H$. If the wavespeed were only known to within, say, 2% over a 2 inch (25.4 mm) path in steel, ΔH would be approximately 1 mm. Because of this fact, we can say that TOFE will typically work only for "relatively large" flaws. The precise meaning of "relatively large," of course, is a function of how accurately the wavespeeds are known and path lengths involved in a particular problem.

The next step is to determine the flaw size and orientation parameters. This can be done, as shown previously, by solving the eigenvalue problem of Eq. (6) for the real symmetric matrix C of Eq. (5), which can be formed from the 6 indirect parameters. Then, we can get the square of the three semi-axis sizes as

the three eigenvalues, and the three orientation unit vectors as the corresponding normalized eigenvectors.

Even though our discussion of the TOFE sizing method considered only a flaw embedded in a single medium (Figure 2a), this method is not restricted to that case only. For the case of sizing a flaw embedded in a second medium, such as in the case of immersion testing (Figure 2b), this method can be also applied using, instead of Eq. (7), the following distance relation as

$$(\underline{x}_I^j - \underline{x}_c) \cdot \underline{n}_2^j = H_2^j + r_e^j \tag{11}$$

where

$\underline{x}_I^j$ is the location of beam entrance point into the second medium for the j-th measurement, $\underline{n}_2^j$ is the unit vector parallel to the wave propagation direction in the second medium for the j-th measurement, H_2^j is the distance from the entrance point to the tangent plane of a flaw for the j-th measurement.

In this case, if information about the transducer location ($\underline{x}_T^j$), the transducer look-angle in the first medium ($\underline{n}_1^j$), and the time-of-flight in the first medium ($\Delta T^j = 2H_1^j$) are obtained, then $\underline{x}_I^j$ can be determined directly by

$$\underline{x}_I^j = \underline{x}_T^j + H_1^j \underline{n}_1^j \tag{12}$$

and the procedure to get the best-fit flaw parameters for the two media case is exactly the same as that for a single medium case, with Eq. (11) replacing Eq. (7).

Implementation

The TOFE sizing algorithm has been implemented in FORTRAN 77 on a VAX computer. In this program, an IMSL subroutine, DUNLSJ, which can solve a non-linear least squares problem using a modified Levenberg-Marquardt algorithm and a user-supplied Jacobian, was adopted to solve the non-linear optimization problem of Eq. (10). Another IMSL subroutine, DEVCSF, was selected as a tool for solving the eigenvalue problem of Eq. (6). As inputs, this program requires at least 9 time-of-flight measurements at different look-angles to iteratively determine the flaw centroid location and C parameters starting from a set of initial guesses for each of these 9 variables. Once the C parameters are obtained, this program then computes the size and the orientation of the best-fit ellipsoid from those C parameters.

PERFORMANCE OF THE TOFE SIZING METHOD

In this section, the performance of the TOFE sizing method will be demonstrated using synthetic and experimental data.

Initial Testing with Synthetic Data

For the initial test of the TOFE method, "exact" synthetic data were generated for known flaws immersed in a single medium using 19 simulated time-of-flight measurements over a one-sided scanning aperture angle of 120 degrees (Figure 3). Four different flaw shapes were considered: a round ellipsoid, a pancake-like flat ellipsoid, a circular crack, and an elliptical crack , all which have the same location and the same orientation but different sizes. For all flaws the best-fit flaw parameters were determined by the TOFE sizing algorithm using the same set of initial guesses of the flaw centroid location (x_{cx} = 0.0, x_{cy} = 0.0, x_{cz} = 0.0) and the C parameters (C_{xx} = 10.0, C_{yy} = 10.0, C_{zz} = 10.0, C_{xy} = 10.0, C_{xz} = 10.0, C_{yz} = 10.0). As shown in Table 1, the TOF method gave the "exact" results (flaw centroid location, size, and orientation) with only 7-16 iterations. Using different sets of initial guesses produced the same results with only slight variations in the number of iterations. Thus, the TOFE sizing method is essentially insensitive to the choice of initial guesses, as expected from the quadratic nonlinearity of Eq. (9).

As mentioned previously, one of the important parameters in equivalent sizing using the TOFE sizing scheme is the ultrasonic velocity in the material, since this is an essential factor for converting the time-of-flight from the transducer to the tangent plane to the corresponding distance, H. Thus the wave velocity in the material should be known a priori for application of the

TOFE sizing method. This information is usually available from other independent experiments.

To investigate the effect of error in velocity information on the TOFE sizing result, a systematic error was introduced into the synthetic data by increasing the wavespeed in the y-direction by 2%. Then the TOFE method was applied to the resulting synthetic data for the round ellipsoid in Table 1 using the same initial guesses as those used previously. The sizing results are shown in Table 2. In the case of one-sided scanning (where we used the same measurement points and the transducer look-angles as those used in the case of error free synthetic data (Figure 3)), the best-fit ellipsoid turned out to be an ellipsoid greatly expanded along both the y and z coordinates as shown in the first diagram of Figure 4. Clearly, this result is not acceptable and comes from the fact that the TOFE algorithm has a relatively large number (9) of degrees of freedom to match the data set. Thus, while the expanded ellipsoid matches the data points very nicely within the aperture angle of the scanning plan , its overall shape is grossly in error (Figure 4).

To overcome this difficulty, two kinds of alternatives were considered. The first alternative was to keep one-sided scanning but instead fit the data to the best-fit equivalent sphere. Since the sphere has only 4 independent variables (3 centroid locations and 1 size parameter) this presumably would stabilize the algorithm. As shown in Table 2 and Figure 4, the best-fit sphere does indeed match the original round ellipsoid quite well in this particular case. Unfortunately, in the use of the best-fit sphere assumption, we lose some of the detail in the shape determination.

The second approach was to employ two-sided scanning where some of the data is taken from the "back" side of a flaw as shown in the last diagram in Figure 4. For the synthetic data set mentioned above, the two-sided scanning data were simulated by simply locating the transducer at the other side of the flaw and changing the transducer look-angle properly. Only 6 data were taken from the "back" side of the flaw with an aperture angle of 120 degrees, and 13 data were taken from the "front" side of the flaw within an aperture angle of 90 degrees. As shown in Table 2 and Figure 4, this resulted in a best-fit ellipsoid expanded only along the y-coordinate as expected. It should be pointed out that we have found even a single data point from the "back" side of a flaw can stabilize the TOFE method for sizing volumetric flaws. Another interesting result that we discovered with the TOFE algorithm was that for cracks, the fact that one of the dimensions of the best-fit ellipsoid is zero (and the center of the flaw is thus constrained to be in the plane of the crack) also stabilized the algorithm, like the sphere assumption, even with only one-sided scanning. This result has been verified experimentally, as will be described shortly.

Spheres Immersed in Water

As an initial experimental verification of the TOFE method, equivalent flaw sizing was done for three steel spheres (with diameters of 1/2 inch (12.7 mm), 3/8 inch (9.53 mm), and 1/4 inch (6.35 mm)) immersed in water. A schematic diagram for the testing geometry is given in Figure 5. The specific experimental apparatus used in this work was an automated multiviewing ultrasonic transducer system developed by Thompson et. al. [30]. This fully automated system can provide the very precise information about the location and the tilting angle of the transducer which is needed for the application of

the TOFE method. As mentioned earlier, two-sided scanning of the sphere is desired, so we have used the reflection from the bottom surface of the supporting plate to obtain the "back side" data. In Figure 5, α denotes the transducer tilting angle in conical scanning for the upper side of the sphere (α = 0 means vertical incidence), and β represents that for conical scanning on the back side of the sphere.

For the 1/2 inch (12.7 mm) diameter sphere, using two-sided conical scanning, a total of 17 measurements were taken; one at normal incidence, 8 from the upper surface of the sphere with $\alpha = 30^{o}$, and 8 from the back surface of the sphere with $\beta = 30^{o}$. As shown in Table 3a, the TOFE method produced a final answer in which the maximum error was only about 0.2 mm and required only 4 iterations from a given set of initial guesses of the flaw centroid location ($x_{cx} = 0.0$, $x_{cy} = 0.0$, $x_{cz} = 0.0$) and the C parameters ($C_{xx} = 1.0$, $C_{yy} = 1.0$, $C_{zz} = 1.0$, $C_{xy} = 1.0$, $C_{xz} = 1.0$, $C_{yz} = 1.0$). For the same data set, the best-fit equivalent sphere also agreed well (~ 0.05 mm error).

For the 3/8 inch (9.53 mm) and the 1/4 inch (6.35 mm) diameter spheres, again using two-sided conical scanning, 17 data points were taken; one with $\alpha = 0^{o}$, 6 points with $\alpha = 22.5^{o}$, another 6 points with $\alpha = 40^{o}$, and finally 4 points with $\beta = 40^{o}$. Using the same initial guesses as those for the case of the 1/2 inch diameter sphere, the TOFE method gave the estimated sizes shown in Tables 3b, c. In both cases convergence was obtained in only 2 iterations, and the maximum error in the size estimation for the semi-axes was 0.4 mm. For both cases, the equivalent best-fit spheres also agreed very well with the actual ones as shown in Tables 3b,c.

Experiments for Flaws in Samples Immersed in Water

These initial experimental tests of the TOFE method were very encouraging, so we also applied this method to more realistic geometries and flaws. In modern engineering applications, composite materials and welded structures are very important and the accurate flaw sizing in these materials is an important element needed to improve the reliability of these structures. Thus, in this study, "flaws" in these two materials were selected; 1) a circular teflon tape insert embedded in an uniaxial graphite/epoxy composite plate, and 2) flat-bottom holes placed in a welded specimen. Such scatterers are typically the types of deliberate "flaws" used to represent real cracks in these structural materials. The automated multiviewing ultrasonic transducer system mentioned previously was again used in these tests.

Sizing of Flaws in Composites

In Figure 6, the schematic diagram for the immersion testing of a teflon tape insert in the composite plate is given. The composite plate was 0.75 cm thick and had the same fiber direction for all layers, which made the composite transversely isotropic. The elastic constants of this plate were determined ultrasonically, and using a coordinate system with the x-axis along the fibers were found to be, c_{11} = 139 GPa, $c_{12} = c_{13}$ = 7.2 GPa, c_{23} = 7.6 GPa, $c_{22} = c_{33}$ = 15.6 GPa, c_{44} = 4.0 GPa, $c_{55} = c_{66}$ = 7.4 GPa, and the density was measured as ρ = 1.61 gm/cm^3 [31]. The plate contained a 1/4 inch (6.35 mm) diameter circular teflon tape parallel to the plate surface, at the depth of 0.34 cm from the top surface.

As mentioned before, in the case of sizing flaws embedded in a specimen immersed in water, the TOFE algorithm requires information on the location of the beam entrance point into the composite ($\underline{x}_I$), and the wavespeed and the

propagation direction of group velocity ($\underline{n}_2$), and the time-of-flight in the composite (refer to Figure 2b). The beam entrance point ($\underline{x}_I$) was determined by simply identifying the reflection from the front surface of the composite. Even in the case of oblique incidence, this was able to be done because of the small tilting angle in the water. Once this incident point was calculated, the time-of-flight information required for the TOFE method could be obtained directly from the oscilloscope A-scan.

Since the composite is anisotropic in material properties, the wave velocity is a strong function of the wave propagation direction. In this case, the slowness surface can be used to calculate wave properties such as the propagation direction, polarization, and phase and group velocity [32]. In this study, these properties of the wave refracted into the composite were calculated with the software package developed by A. Minachi at the Center for NDE, Iowa State University.

In one-sided conical scanning, a total of 13 data points were taken at different look-angles; 1 point at normal incidence, 4 points each at $\alpha = 2.5^{\circ}$ and 5.0°, and another 2 points each at $\alpha = 7.5^{\circ}$ and 10°. For this data set the TOFE algorithm was applied with the given initial guesses of the flaw centroid location ($x_{cx} = 0.0$, $x_{cy} = 0.0$, $x_{cz} = 0.0$) and the C parameters ($C_{xx} = 1.0$, $C_{yy} = 1.0$, $C_{zz} = 1.0$, $C_{xy} = 0.0$, $C_{xz} = 0.0$, $C_{yz} = 0.0$). As shown in Table 4, it produced a nearly circular crack with correct orientation and location with only 11 iterations when we used the wave properties considering anisotropy of the composite sample. In this case the maximum error was 0.5 mm in the size of the semi-axes.

Table 4 also presents the TOFE sizing result for the same flaw under the condition where anisotropy of the composite sample was neglected. In this case the composite sample was considered as an isotropic plate with the longitudinal wavespeed of 0.3122 cm/μsec (the longitudinal wavespeed through thickness of the composite plate at the normal incidence). The TOFE method produced a round elliptical crack (with correct orientation) with 1.2 mm offset in the center location. A total of 14 iterations were required from the same initial guesses mentioned above. This result is somewhat poorer than that of the above case where precise wavespeeds were used. This implies that correct characterization of the wavespeed of a host medium is important for the accurate sizing using the TOFE method.

Sizing of Flaws in Weldments

Figure 7 shows a schematic diagram for immersion testing of a flat-bottom hole in a welded specimen. The welded specimen was fabricated by the submerged arc welding process with the deposition of two weld passes, which completely filled the 60 degree double-V weld groove prepared on pieces of 1/2 inch (12.7 mm) thick mild steel plate. After the welding, the weld reinforcements were removed to get a smooth and flat specimen with a thickness of 11.5 mm. After this machining, 5 mm diameter flat-bottom holes with a 3 mm depth were fabricated both in the weldment and in the base metal.

As in the composite case, the TOFE algorithm here requires the wavespeed, propagation direction, and the time-of-flight in the welded specimen, as well as the location of the beam entrance point into the specimen. Obviously, the welded joint has inhomogeneous and anisotropic material properties in general. But in the case of a mild steel welded joint, these

inhomogeneities and anisotropy are not expected to be large and have been neglected. Thus, the welded specimen was treated as a homogeneous and isotropic steel plate, and its wavespeed was assumed to be constant in all directions. The beam entrance location into the specimen and the time-of-flight of the wave in the welded specimen were determined in a manner similar to that used for the composite plate.

For each flat-bottom hole, a total of 19 data points were taken using one-sided conical scanning; 1 data at normal incidence, and 6 at each tilting angle of $\alpha = 2.5^{o}, 4.9^{o}, 7.2^{o}$ which corresponds to a refracted angle in the welded specimen of $10^{o}, 20^{o}, 30^{o}$, respectively. Using these data, the TOFE scheme determined the best-fit parameters, as shown in Table 5, with only 14 and 44 iterations for the flat-bottom holes in the weldment and in the base metal, respectively, from a given set of initial guesses of the flaw centroid location ($x_{cx} = 0.0$, $x_{cy} = 0.0$, $x_{cz} = 0.0$) and the C parameters ($C_{xx} = 0.0$, $C_{yy} = 0.0$, $C_{zz} = 0.0$, $C_{xy} = 0.0$, $C_{xz} = 0.0$, $C_{yz} = 0.0$). The final result very nicely described the major features of the bottom of the flat-bottom holes (which appear to the algorithm as flat cracks) such as the crack shape, size of the semi-axes, and orientation. The errors in the size estimates were 0.1-0.2 mm for the hole in the base metal, and 0.4-1.0 mm for the hole in the weldment.

CONCLUSIONS

We have described a new time-of-flight equivalent (TOFE) sizing method for relatively large flaws in materials. We have shown that for volumetric flaws the algorithm is stable and fast provided that time-of-flight information is available in two-sided scanning or the equivalent shape is restricted to that of a sphere for one-sided scanning. For cracks, the method is always stable and fast, even in one-sided scanning.

This method uses the time-of-flight information in ultrasonic signals, which is easily available and relatively insensitive to various sources of measurement error. Since the TOFE method falls into the category of an equivalent flaw sizing approach, it requires relatively few ultrasonic measurements to obtain the major features of flaws in terms of a best-fit ellipsoid, which then can be directly used in fracture mechanics calculations.

From our tests of the TOFE method in both a composite material and a weldment we have shown that the method is accurate provided that the wave speed in the material is well characterized. Finally, the excellent performance of the TOFE method observed in this study suggest that it can serve as a robust sizing tool for many practical applications.

ACKNOWLEDGEMENTS

One of the authors, S. J. Song, would like to thank Dr. C. P. Chiou for his valuable discussions. This research was supported by the Center for Nondestructive Evaluation at Iowa State University.

REFERENCES

1. R. B. Thompson and D. O. Thompson, "Ultrasonics in nondestructive evaluation." Proceedings of the IEEE, Vol. 73, pp. 1716-1755, 1985.

2. R. B. Thompson, "Quantitative ultrasonic nondestructive evaluation methods." Transactions of ASME/ Journal of Applied Mechanics, Vol. 50, pp. 1191-1201, 1983.

3. J. Krautkramer and H. Krautkramer, Ultrasonic Testing of Materials, 4th Edition, New York: Springer-Verlag, 1990.

4. J. Krautkramer, "Determination of the size of defects by the ultrasonic impulse echo method.", British Journal of Applied Physics, Vol. 10, pp. 240-145, 1954.

5. International Institute of Welding, Handbook on the Ultrasonic Examination of Welds, Cambridge, England: Welding Institute for the International Institute of Welding, 1977.

6. International Institute of Welding, The Evaluation of Ultrasonic Signals, Cambridge, England: Welding Institute for the International Institute of Welding, 1987.

7. H. J. Meyer, "The international state of the art in nondestructive inspection of welds with special emphasis on flaw characterization." Materials Evaluation, Vol. 42, pp. 793-802, 1984.

8. D. Heinrich, K. H. Mayer, G. Muller and W. Prestel, "Manual and mechanized ultrasonic inspection of large components in respect of flaw estimation by fracture mechanics." Nuclear Engineering and Design, Vol. 112, pp. 127-137, 1989.

9. M. G. Silk, A. M. Stoneham and J. A. G. Temple, The Reliability of Non-Destructive Inspection, Bristol, England: Adam Hilger, 1987.

10. M. G. Silk, "Sizing crack-like defects by ultrasonic means." in Research Techniques in Nondestructive Testing, Vol. 2, Ed. R. S. Sharpe, Ch. 2, London: Academic Press, 1977.

11. M. G. Silk, "The use of diffraction based time-of-flight measurements to locate and size defects." British Journal of NDT, Vol. 26, pp. 208-213, 1984.

12. G. J. Gruber, "Defect identification and sizing by the ultrasonic satellite-pulse technique." Journal of Nondestructive Evaluation, Vol. 1, pp. 263-273, 1980.

13. G. J. Gruber, G. J. Hendrix and W. R. Schick, "Characterization of flaws in piping welds using satellite pulses." Materials Evaluation, Vol. 42, pp. 426-432, 1984.

14. J. P. Charlesworth and J. A. G. Temple, Engineering Applications of Ultrasonic Time-of-Flight Diffraction, Somerset, England: Research Studies Press, 1989.

15. C. F. Schueler, H. Lee and G. Wade, "Fundamentals of digital ultrasonic imaging." IEEE Transactions on Sonics and Utrasonics, Vol. SU-31, pp. 195-217, 1984.

16. C. F. Quate, A. Atalar and H. K. Wickramasinghe, "Acoustic Microscopy with mechanical scanning - a review." Proceedings of IEEE, Vol. 67, pp. 1092-1114, 1979.

17. J. Seydel, "Ultrasonic synthetic-aperture focusing techniques." in Research Techniques in Nondestructive Testing, Vol. VI, Ed. R. S. Sharpe, New York: Academic Press, pp. 1-48, 1982.

18. S. O. Harrold, "Ultrasonic focusing techniques." in Research Techniques in Nondestructive Testing, Vol. VI, Ed. R. S. Sharpe, New York: Academic Press, pp. 49-106, 1982.

19. B. Grohs, O. A. Barbian, W. Kappes, H. Paul, R. Licht and F. W. Hoh, "Characterization of flaw location, shape, and dimensions with the ALOK system." Materials Evaluation, Vol. 40, pp. 84-89, 1982.

20. B. P. Hildebrand and B. B. Brenden, An Introduction to Acoustical Holography, New York: Plenum Press,1972.

21. D. K. Hsu, J. H. Rose and D. O. Thompson, "Reconstruction of inclusions in solids using ultrasonic Born inversion." Journal of Applied Physics, Vol. 55, pp. 162-168, 1984.

22. D. K. Hsu, D. O. Thompson and S. J. Wormley "Reliability of reconstruction of arbitrarily oriented flaws using multiview transducers."

IEE Transactions of Ultrasonics, Ferroelectrics, and Frequency Control, Vol. UFFC-34, pp. 508-514, 1987.

23. A. Sedov and L. W. Schmerr, "The time domain elastodynamic Kirchhoff approximation for cracks: the inverse problem," Wave Motion, Vol. 8, pp. 15-26, 1986.

24. L. W. Schmerr, A. Sedov and C. P. Chiou, "A unified constrained inversion model for ultrasonic flaw sizing." Research in Nondestructive Evaluation, Vol. 1, pp. 77-97, 1989.

25. C. P. Chiou and L. W. Schmerr, "New approaches to model-based ultrasonic flaw sizing." submitted to Journal of Acoustical Society of America.

26. L. J. Bond, C. A. Chaloner, S. J. Wormley, S. P. Neal, and J. H. Rose, "Recent advances in Born Inversion (weak scatterers)." in Review of Progress in Quantitative Nondestructive Evaluation, Eds. D. O. Thompson and D. E. Chimenti, Vol. 7A, pp. 437-444, 1988.

27. C. A. Chaloner and L. J. Bond, "Investigation of the 1-D inverse Born technique." IEE Proceedings, Vol. 134, Pt. A, pp. 257-265, 1987.

28. L. S. Koo, "Ultrasonic flaw classification: an approach using modelling, signal processing, and adaptive learning." Ph.D. Dissertation, Iowa State University, 1987.

29. S. J. Song and L. W. Schmerr, "Ultrasonic flaw sizing - some new approaches", to appear in Review of Progress in Quantitative Nondestructive Evaluation, Eds. D. O. Thompson and D. E. Chimenti, Vol. 11, 1992.

30. D. O. Thompson, S. J. Wormley, and D. K. Hsu, "Apparatus and technique for reconstruction of flaws using model-based elastic wave inverse ultrasonic scattering." Review of Scientific Instruments, Vol. 57, pp. 3089-3098, 1986.

31. B. P. Newberry, "Paraxial approximations for ultrasonic beam propagation in liquid and solid media with applications to nondestructive evaluation." Ph. D. Thesis (unpublished), Iowa State University, 1988.

32. B. A. Auld, Acoustic Fields and Waves in Solids, Vol. II, Ch. 9, New York: A Wiley-Interscience Publication, 1973.

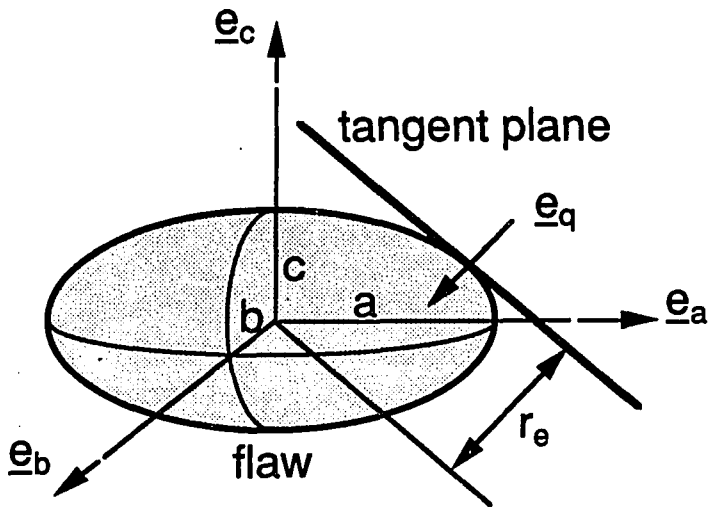

Figure 1a. Ellipsoidal geometry and the definition of the equivalent radius, r_e

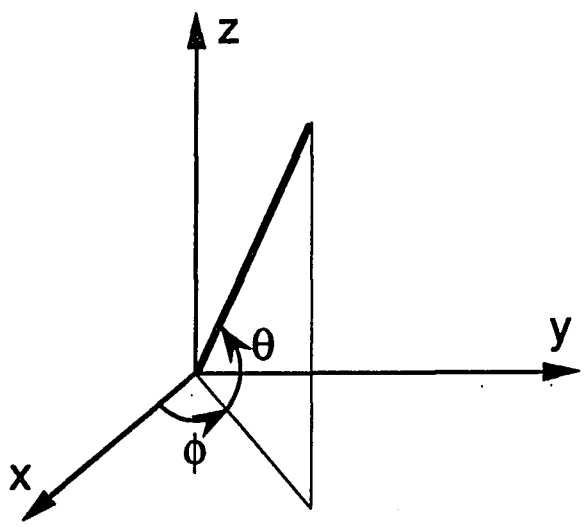

Figure 1b. Spherical coordinate system used for the unit vector $\underline{e}_q$

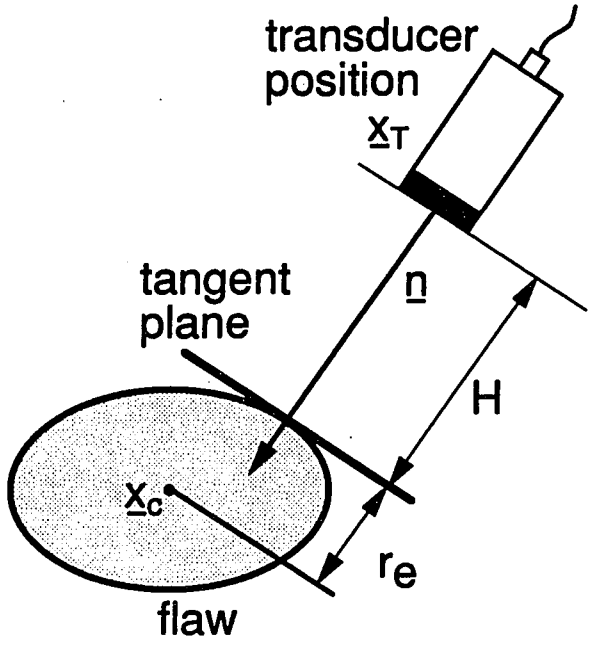

Figure 2a. The measurement geometry of the TOFE sizing method for a flaw embedded in a single medium.

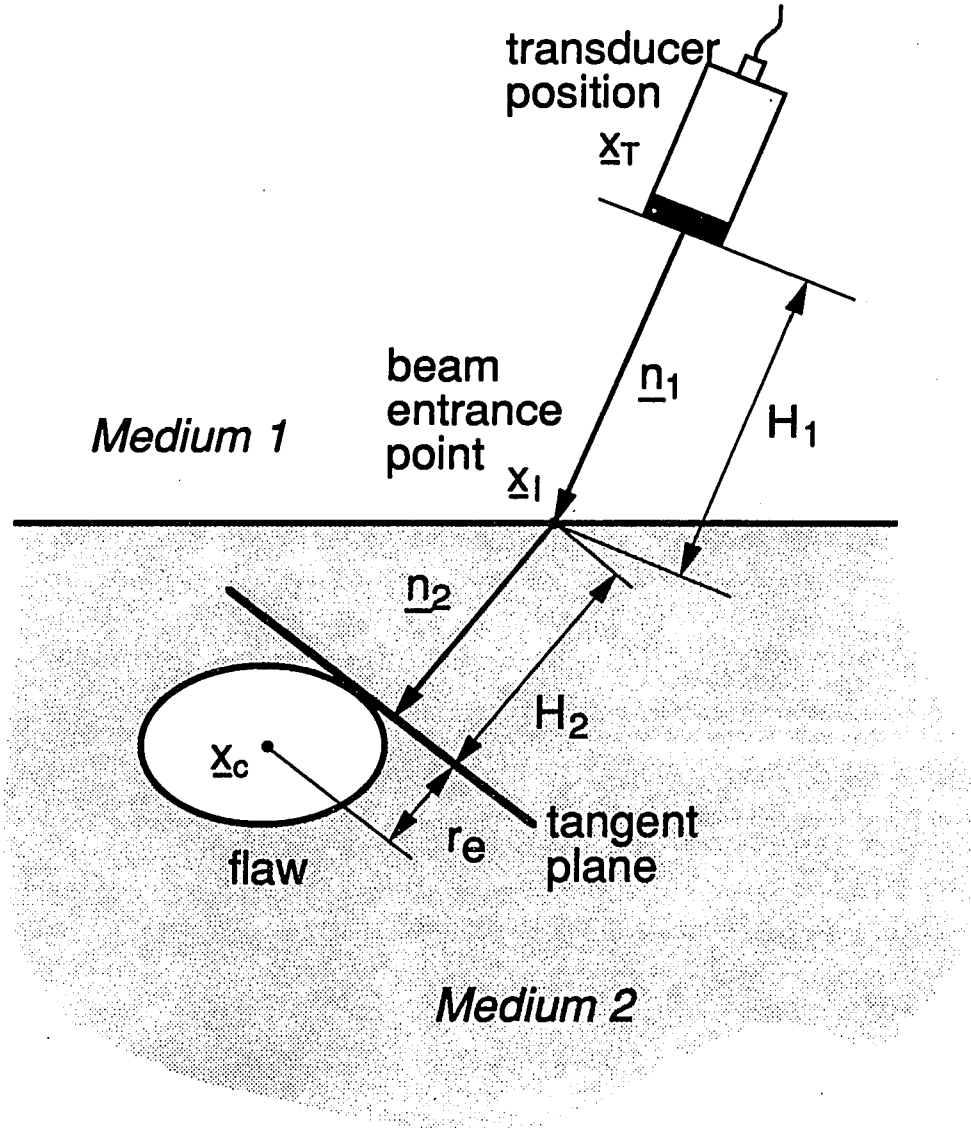

Figure 2b. The measurement geometry of the TOFE sizing method for a flaw embedded in a second medium.

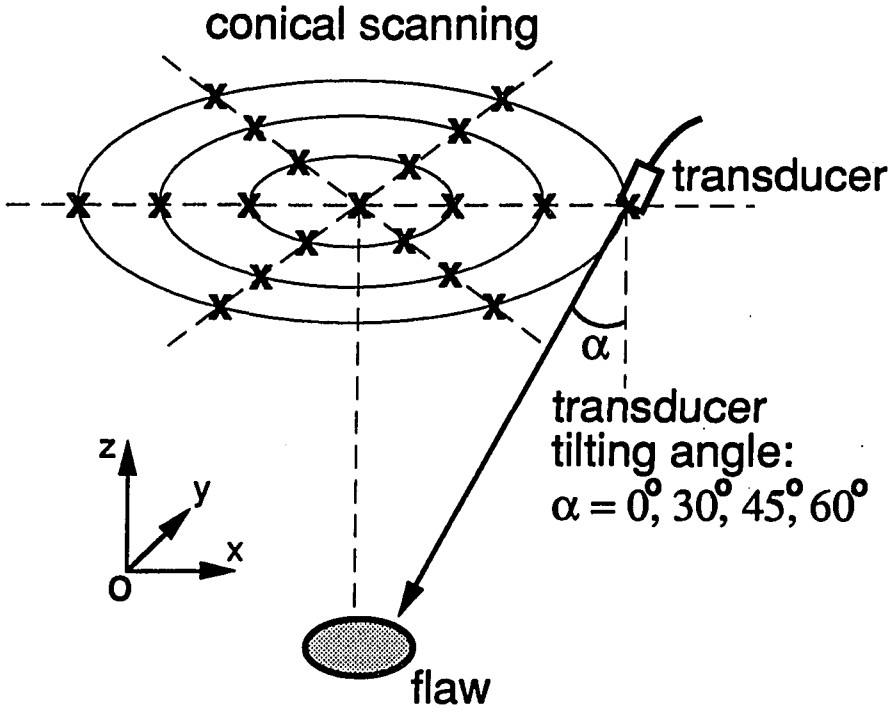

Figure 3. Schematic diagram of one-sided conical scanning with synthetic data for a known flaw ("x" denotes a measurement point in a single medium).

Table 1. TOFE sizing results for error free synthetic data.

(unit : mm)

shape	a	b	c	# of iterations
Ellipsoid				
round	20	25	30	16
pancake	10	5	0.5	9
Crack				
circular	10	10	0	7
elliptical	10	5	0	8

Table 2. TOFE sizing results for synthetic data with systematic error.

(unit : mm)

	Actual	Two-side Scan (ellipsoid)	One-side Scan (ellipsoid)	(sphere)
x	3.0	3.0	2.9	3.0
y	5.0	5.0	4.7	5.0
z	- 6.0	- 6.8	- 45.9	- 1.9
a	20.0	19.3	28.9	
b	25.0	31.3	44.4	25.6
c	30.0	30.8	70.0	

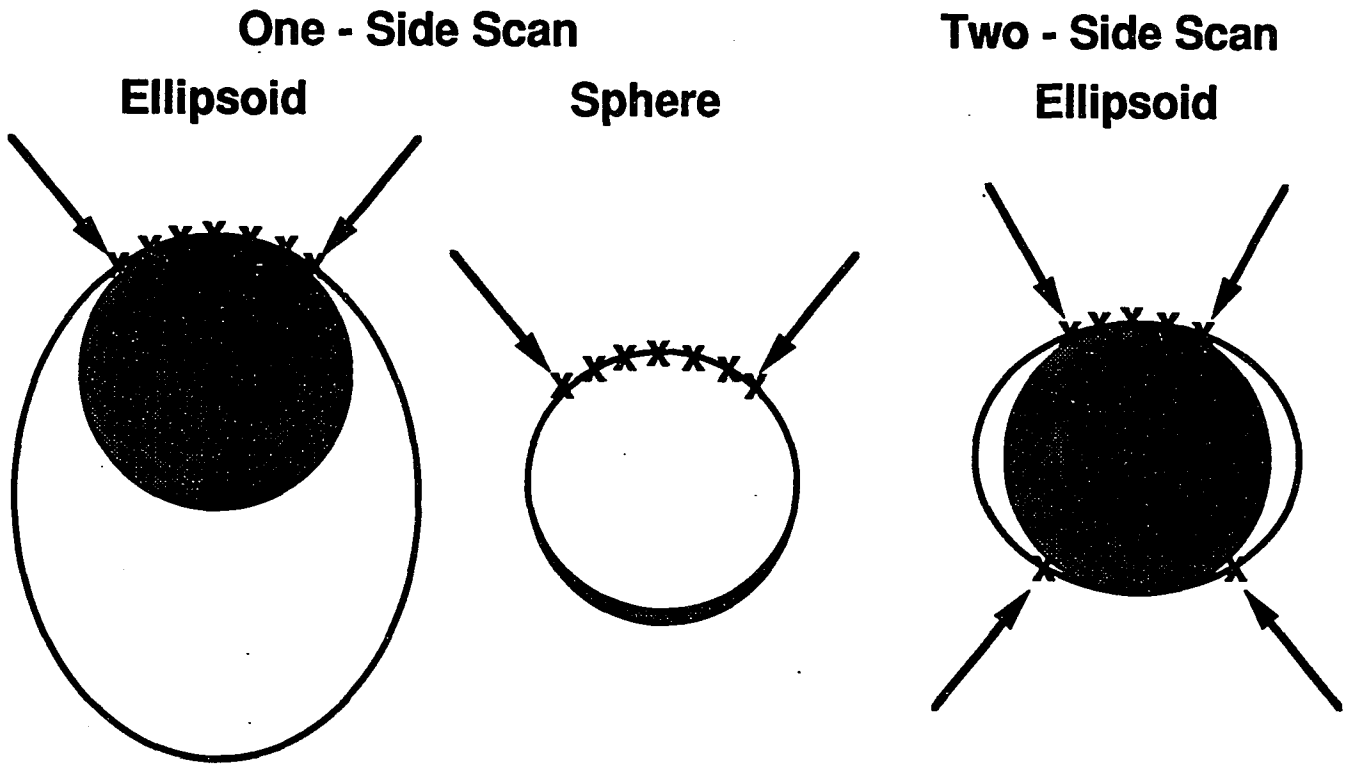

Figure 4. Schematic diagrams of the TOFE sizing results for synthetic data with a systematic error ("x" denotes the data points). actual shape: shaded figure, reconstructed shape: open figure.

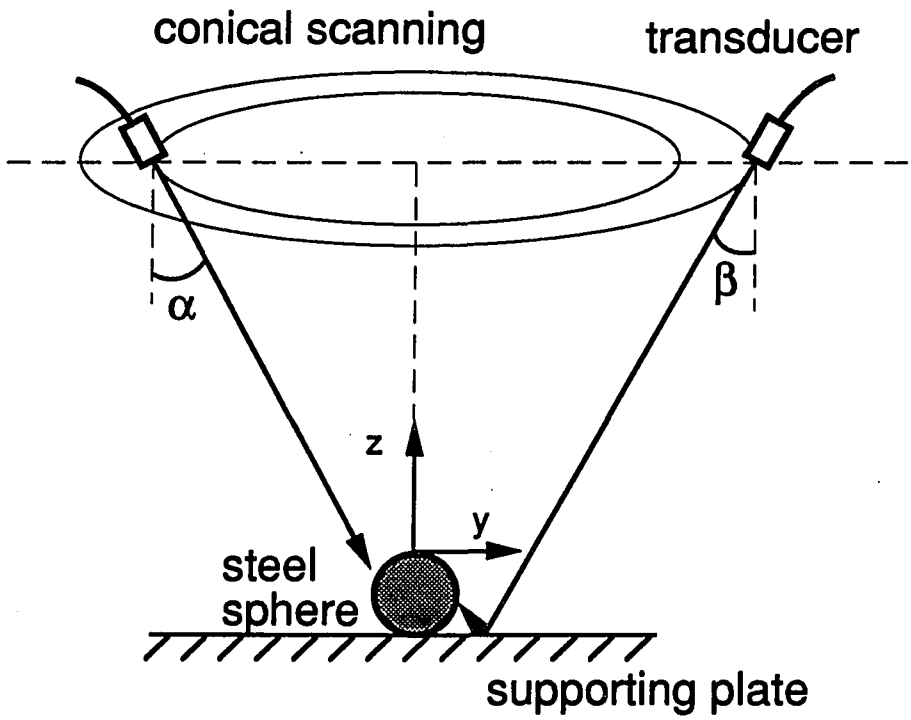

Figure 5. Schematic diagram of the TOFE sizing setup for a steel sphere immersed in water.

Table 3a. TOFE sizing results for a 1/2 inch (12.7 mm) diameter steel sphere immersed in water.

(unit : cm)

Parameter		Actual	Ellipsoid	Sphere
location	x	0.0	0.05	0.05
	y	0.0	0.03	0.03
	z	-0.635	-0.65	-0.65
size	a	0.635	0.60	
	b	0.635	0.64	0.64
	c	0.635	0.66	

Table 3b. TOFE sizing results for a 3/8 inch (9.53 mm) diameter steel sphere immersed in water.

(unit : cm)

Parameter		Actual	Ellipsoid	Sphere
location	x	0.0	0.05	0.04
	y	0.0	0.00	0.00
	z	-0.476	-0.48	-0.48
size	a	0.476	0.46	
	b	0.476	0.45	0.48
	c	0.476	0.50	

Table 3c. TOFE sizing results for a 1/4 inch (6.35 mm) diameter steel sphere immersed in water.

(unit : cm)

Parameter		Actual	Ellipsoid	Sphere
location	x	0.0	0.04	0.03
	y	0.0	0.01	0.01
	z	-0.318	-0.33	-0.32
size	a	0.318	0.28	
	b	0.318	0.30	0.32
	c	0.318	0.34	

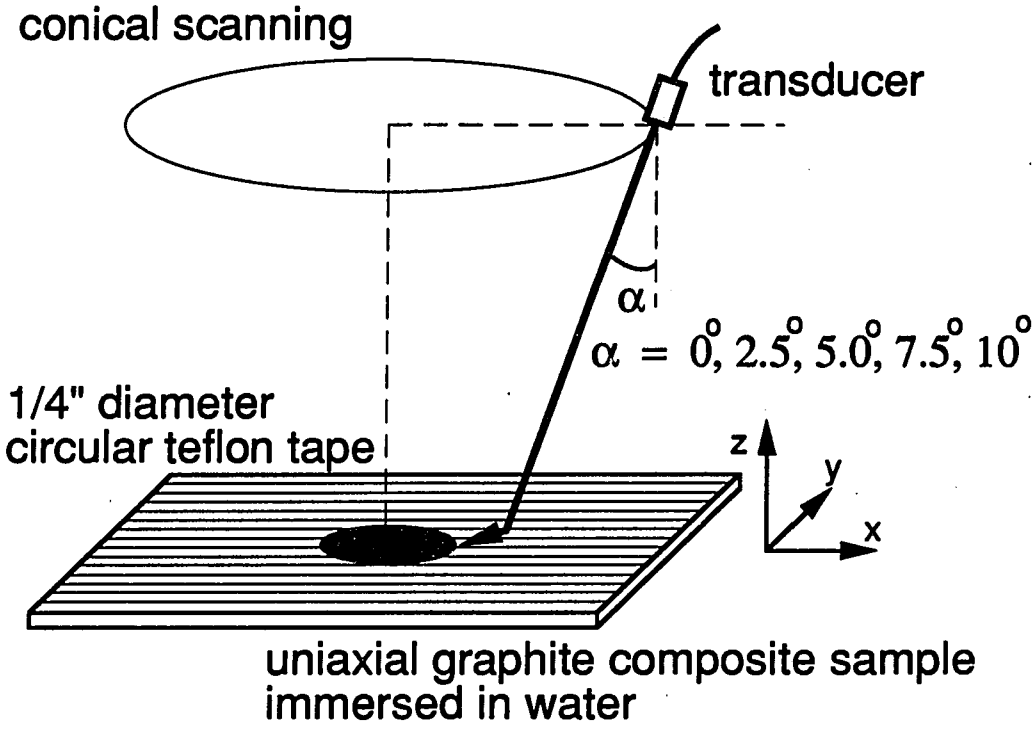

Figure 6. Schematic diagram of the TOFE sizing setup for a 1/4 inch (6.35 mm) diameter circular teflon tape insert embedded in an uniaxial graphite/epoxy composite sample (immersion testing).

Table 4. TOFE sizing result for a 1/4 inch (6.35 mm) diameter circular teflon tape insert embedded in an uniaxial graphite/epoxy composite sample (immersion testing).

(unit : cm)

Parameter		Actual	Best-fit ellipsoid (1)	Best-fit ellipsoid (2)
location	x	0.0	-0.02	-0.11
	y	0.0	0.05	0.05
	z	-0.340	-0.34	-0.34
size	a	0.318	0.27	0.30
	b	0.318	0.26	0.26
	c	0.0	0.00	0.00

(1) Consider the composite sample as an anisotropic material.

(2) Consider the composite sample as an isotropic material.

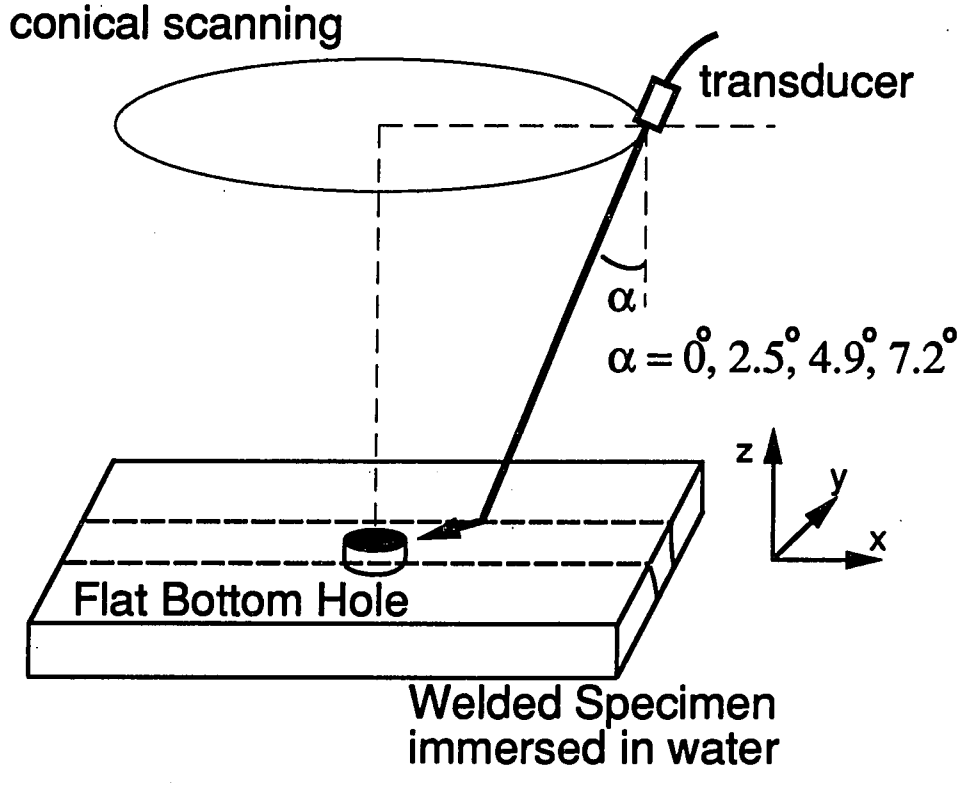

Figure 7. Schematic diagram of the TOFE sizing setup for 5mm diameter flat-bottom holes fabricated in in a mild steel welded specimen (immersion testing).

Table 5. TOFE sizing results for 5 mm diameter flat-bottom holes fabricated in a mild steel welded specimen (immersion testing).

(unit : cm)

Parameter		Actual	Flat Bottom Hole in Weldment	Flat Bottom Hole in Base Metal
location	x	0.0	0.00	0.01
	y	0.0	-0.03	0.06
	z	-0.89	-0.85	-0.87
size	a	0.25	0.21	0.24
	b	0.25	0.15	0.27
	c	0.0	0.00	0.00

PART IV. NEW APPROACHES TO ULTRASONIC EQUIVALENT SIZING FOR SMALL FLAWS

New approaches to ultrasonic equivalent sizing for small flaws

Sung-Jin Song and Lester W. Schmerr

Center for NDE and
Department of Aerospace Engineering and Engineering Mechanics

Iowa State University

Ames, Iowa 50011

ABSTRACT

Ultrasonic equivalent flaw sizing methods size defects in a material by obtaining a best-fit simple defect shape (such as an ellipsoid or ellipse) from relatively small amounts of ultrasonic data. In these equivalent flaw sizing methods, it is essential that the origin of time be determined precisely with respect to a fixed spatial location. Current methods for this determination are not entirely adequate, leading to an important "zero-of-time" problem.

In this work, two new approaches to equivalent flaw sizing for relatively small flaws are developed: 1) an amplitude-based equivalent (ABE) sizing method for obtaining best-fit equivalent flaws by the use of amplitude ratios measured at different transducer orientations, and 2) a first moment (FM) method for estimating the equivalent radius from a first moment calculation of the time domain flaw response. We show how these approaches can address the zero-of-time problem and demonstrate the performance of these methods with experiments.

INTRODUCTION

Modern high performance systems, such as jet engines, operate under extreme conditions where flaws of even small size can eventually cause catastopic failures. To guarantee the safety and reliability of these systems, their integrity is often evaluated using nondestructive evaluation (NDE) methods such as ultrasonics. These NDE techniques must provide quantitative information on the geometry of a flaw (location, shape, size, and orientation) that can be used in conjunction with methods for evaluating the significance of the flaw, such as fracture mechanics. Unfortunately, conventional ultrasonic NDE techniques [1] which use mainly peak amplitude information of ultrasonic signals, are not adequate for these purposes, particularly as the size of a flaw decreases to the dimension of the wavelength of the probing ultrasonic wave. Thus, a variety of alternate approaches have been sought for the sizing of small flaws from ultrasonic measurements.

Imaging techniques have been sucessful in obtaining more complete information about the geometry of relatively large flaws, using detailed scanning and massive data processing [2]. However, for small flaws these methods also have been inadequate.

In between the two extremes of conventional methods and detailed imaging techniques, there is a model-based approach called equivalent flaw sizing [3,4,5]. In this method, flaws are reconstucted in term of "best-fit" equivalent ellipsoids (for volumetric flaws) or ellipses (for cracks) obtained from a relatively small number of ultrasonic measurements made at different transducer orientations and locations. This approach has been developed based on ultrasonic scattering models such as the Born approximation for volumetric

flaws [3,4] or the Kirchhoff approximation for cracks [5]. Recently, a unified algorithm that can be applied to both volumetric flaws and cracks has been developed by Schmerr and et. al. [6]. Previous work in this area has shown that it is a viable sizing tool if the equivalent radius, r_e, which is defined as the distance from the flaw centroid to the front surface tangent plane (Figure 1a) can be extracted accurately from the ultrasonic measurements [6,7]. For large flaws, this information can be obtained directly from time-of-flight measurements [8]. For small flaws, r_e is normally obtained directly from the ultrasonic waveform itself, using models based on the Born and Kirchhoff approximations and signal processing methods [3-7]. Here "large" and "small" are defined in the following manner. If the errors in measuring r_e from time-of-flight measurements between the transducer and the flaw are unacceptable for r_e less than some length d, then the flaw will be said to be "small" if $r_e < d$ and "large" if $r_e > d$. In this manner we have in effect defined as "small" any flaw where simple time-of-flight methods [8] fail. In most cases the value of d is determined by the accuracy of the transducer positioning device and the accuracy of the determination of the wavespeed(s) of the propagating materials [8]. In the small flaw case, it is crucial to determine the absolute phase of the measured response with respect to a fixed spatial location near the flaw or, alternatively, to relate a time origin (i.e., the "zero-of-time") in the ultrasonic waveforms with respect to a fixed spatial location, usually taken as the centroid of the flaw. Current methods for determining the zero-of-time, however, are not entirely adequate [9,10].

In this work, two new approaches will be addressed: The first one is an amplitude-based equivalent (ABE) sizing method, which can determine the

best-fit equivalent flaw geometry using ratios of pulse-echo amplitude measurements taken at different transducer orientations. We show how this method reduces the zero-of-time determination problem to a linear least squares estimation of a single parameter. The second approach is called the first moment (FM) method. In this case we demonstrate how the equivalent radius and the corresponding zero-of-time can be determined simply from a calculation based on the first moment of the ultrasonic waveform [11]. Both of these new algorithms will be described in detail and their performance will be evaluated on synthetic and experimental data.

EQUIVALENT FLAW SIZING

This section will briefly address some key aspects of current equivalent flaw sizing techniques , the zero-of-time problem, and some very recent developments [7].

Major Elements

The basic parameter that must be found in equivalent flaw sizing methods is the equivalent flaw radius, r_e, which is the distance from the flaw centroid to a surface tangent plane where the incident wavefront (assumed plane) first touches the flaw (Figure 1). For an ellipsoid, r_e, is determined by three factors; the flaw size parameters (a,b,c), the flaw orientation parameters ($\underline{e}_a$, $\underline{e}_b$, $\underline{e}_c$), and a known incident wave direction ($\underline{e}_q$) as shown in Figure 1. Specifically, for an ellipsoid we have:

$$(1) \qquad r_e = [\, a^2(\underline{e}_q \cdot \underline{e}_a)^2 + b^2(\underline{e}_q \cdot \underline{e}_b)^2 + c^2(\underline{e}_q \cdot \underline{e}_c)^2 \,]^{\frac{1}{2}}$$

The relationship of Eq. (1) is also true for the case of an elliptical flat crack with one semi-radius, say c, taken equal to zero. Once a number of equivalent radius data at different incident wave angles are available, this information can be used, as will be shown shortly, to obtain the best-fit flaw geometry. Hence, most equivalent flaw sizing schemes currently involve: 1) the measurement of the scattered waveforms from a number of different transducer orientations, 2) the extraction of the equivalent radius, r_e, from these waveforms, and 3) the determination of the best-fit ellipsoid, using Eq. (1), that matches the measured r_e data.

Measurement of the Equivalent Radius

Accurate measurement of the equivalent radius is the one of the most important steps in equivalent flaw sizing. A variety of algorithms have been developed based on ultrasonic scattering models such as the Born and Kirchhoff approximation. Here current available techniques will be reviewed briefly.

The Born approximation [12] has previously been employed to solve the direct scattering problem for volumetric flaws in the weak scattering limit. Using the Born approximation, an inversion scheme called the inverse Born approximation (IBA) [13,14] has also been developed for the determination of the flaw characteristics from ultrasonic scattering data. The IBA involves a 3-D inverse Fourier transform of the scattering amplitudes measured at different angles and frequencies. For the case of flaws with spherical symmetry, the 3-D inverse Fourier transform reduces to a simple one dimensional inverse transform (called the 1-D IBA) given by

$$\gamma(r) = \text{constant} \times \int_0^\infty A(k) \frac{\sin 2kr}{2kr} \, dk \tag{2}$$

where

$\gamma(r)$ is the characteristic function for the flaw defined as $\gamma(r) = 1$ inside the flaw and $\gamma(r) = 0$ outside, $A(k)$ is the far-field scattering amplitude calculated from the far-field scattered time response in a coordinate system with its origin located at the flaw centroid, and k is the wavenumber defined by $k = \omega/c$.

Eq. (2) can provide an estimate of the radius of spherical inclusions through the characteristic function. For flaws with more complicated shape, Eq. (2) produces an estimate of the equivalent radius depicted in Figure 1 [15]. Even though the IBA has originally been derived under the weak scattering assumption, it has been shown that the same algorithm can also size strong scatterers, such as voids [16].

Practical implementation of the IBA requires the determination of the absolute phase of the scattered response with respect to a fixed spatial location so that A(k) in Eq. (2) can be calculated unambiguously. In Eq. (2), this fixed spatial location is the centroid of the flaw. In the scattered wave time domain response, this absolute phase determination is equivalent to locating the time origin (the zero-of-time) at the flaw centroid. Solving for the zero-of-time, therefore, is essential to make equivalent flaw sizing approaches, like the IBA, work and has been an important research topic [9,10]. For determination of the zero-of-time, the area function method [6,17] has been developed based on the Born scattering model. Chaloner and Bond [10] have discussed this and other methods such as a maximum flatness method, a minimization of imaginary part method, and a low frequency examination.

It has been pointed out that the IBA requires a broad band pulse because the high frequency data are useful to detect the front surface of a flaw while low frequency data are needed to find the flaw centroid [17]. In practice, the bandlimited nature of the transducer response causes a loss of low frequency information, which introduces a major difficulty in the determination of the flaw centroid. To overcome this, various low frequency extrapolation techniques [17,18,19] have been developed.

Once the center of flaw location is determined, the equivalent radius can be estimated via Eq. (2). Since the accuracy of flaw size prediction is so sensitive to the zero-of-time problem, there have also been developed some schemes which can estimate the equivalent radius directly from ultrasonic measurements without explicit determination of the flaw centroid location. Bond et al [9] have proposed a method which uses the flaw radius variation curve with respect to a variety of time-shifts. Based on the Kirchhoff approximation, Schmerr and his co-workers [5,6] have developed a method which uses the time separation between the flashpoints for cracks. More recently, Yang and Bond [20] proposed a simple heuristic scheme which uses the distance between the minimum and the maximum of the area function curves.

Unfortunately, no entirely satisfactory and general solution to this problem currently exists. Thus, one important part of the sizing methods described here will be to demonstrate new and robust methods for solving the zero-of-time problem.

Determination of the Best-Fit Equivalent Flaw Geometry

Once the equivalent radius data have been obtained for all available ultrasonic measurements, it is necessary to use this data to determine the best-fit equivalent flaw parameters. In many previous equivalent flaw sizing schemes, a nonlinear optimization approach was used for this purpose. For N measurements of r_e at different transducer orientations ($\underline{e}_q$), one can form up the function

$$(3) \qquad I(a,b,c,\underline{e}_a,\underline{e}_b,\underline{e}_c) = \sum_{i=1}^{N} [\,(r_e^{exp})_i - (r_e^{model}(a,b,c,\underline{e}_a,\underline{e}_b,\underline{e}_c))_i\,]^2$$

and search for the best-fit parameters (a, b, c, $\underline{e}_a$, $\underline{e}_b$, $\underline{e}_c$) that match the measurements, by minimizing the function I. Here $(r_e^{exp})_i$ are the experimentally measured r_e values and $(r_e^{model})_i$ are obtained from Eq. (1). As Chiou and Schmerr [6] have pointed out, solving Eq. (3) is difficult because of the very complicated nonlinear nature of the problem. Fortunately, this difficulty can be avoided entirely through a reformulation of the sizing problem into a two-step procedure [7]. Here we describe briefly that procedure which is called the linear least squares / eigenvalue problem approach.

Instead of using Eq. (1) directly as a nonlinear relation between the equivalent radius r_e and flaw parameters (a, b, c, $\underline{e}_a$, $\underline{e}_b$, $\underline{e}_c$), we can define a linear relationship by relating r_e^2 to a set of six C parameters as

$$(4) \qquad r_e^2 = \underline{e}_q \cdot \underset{\sim}{C}\,\underline{e}_q$$

where

$$\underset{\sim}{C} = a^2 \underline{e}_a \otimes \underline{e}_a + b^2 \underline{e}_b \otimes \underline{e}_b + c^2 \underline{e}_c \otimes \underline{e}_c$$

is a symmetric second order tensor. (Here, $\otimes$ denotes a diadic product operator.) Using Eq. (4) we can form up the function

$$(5) \qquad J(\underset{\sim}{C}) = \sum_{i=1}^{N} [(r_e^{exp})_i^2 - (\underline{e}_q^i \cdot \underset{\sim}{C}\,\underline{e}_q^i)]^2$$

and find the best-fit coefficients that fit the measured data taken at N different transducer orientations $\underline{e}_q^i$ (i = 1,2, ... ,N). The advantage of Eq. (5) over Eq. (2) is that now we need only solve a much simpler and well-behaved linear least squares problem.

Once the tensor C is obtained in a given fixed (x,y,z) coordinate system, a real symmetric matrix C can be formed as

$$(6) \qquad \underset{\sim}{C} = \begin{bmatrix} C_{xx} & C_{xy} & C_{xz} \\ C_{xy} & C_{yy} & C_{yz} \\ C_{xz} & C_{yz} & C_{zz} \end{bmatrix}$$

By solving the eigenvalue problem of this matrix C, i.e.

$$(7) \qquad \underset{\sim}{C} - \lambda \underset{\sim}{I} = 0$$

all the equivalent flaw parameters can then be obtained since the eigenvalues of C are just the squares of the three semi-axis sizes (a^2, b^2, c^2) and the three eigenvectors of C are the corresponding three orientation unit vectors ($\underline{e}_a$, $\underline{e}_b$, $\underline{e}_c$). Chiou and Schmerr [7] have already shown the excellent performance of this approach using both synthetic and experimental data.

KIRCHHOFF APPROXIMATION

Our two new sizing approaches for small flaws, which will be discussed in the following sections, are both based on the Kirchhoff approximation. Thus, in this section, some aspects of that approximation will be discussed.

We first consider the scalar wave scattering problem for a homogeneous, isotropic fluid inclusion (having wavespeed c_2 and density ρ_2) in a homogeneous, isotropic 3-dimensional fluid medium (having wavespeed c_1 and density ρ_1). Figure 2 shows explicitly the geometry of this scattering problem where a smooth inclusion of arbitrarily convex shape is bounded by a closed surface S embedded in an unbounded surrounding medium.

As is well known, the pressure in the waves scattered from this inclusion can be written in the far-field as

$$p^{sc}(\underline{x}_o) = f \cdot \frac{e^{ikr_o}}{r_o} \tag{8}$$

where, f, the far-field scattering amplitude is given by

$$f = -\frac{1}{4\pi} \int_S [\, \partial p(\underline{x})/\partial n(\underline{x}) + ik(\underline{e}_s \cdot \underline{n})\, p(\underline{x})\,] \exp(-ik\underline{x} \cdot \underline{e}_s)\, dS(\underline{x}) \tag{9}$$

Evaluation of Eq. (9) requires both $p(\underline{x})$, and its normal derivative on the boundary S of the scatterer. In general, these are unknown. One way to obtain these quantities is via assumptions, such as those made in the Born [12] and Kirchhoff [21] approximations.

In the high frequency limit, the boundary S can be sharply divided into a lit side S_l and a dark side S_d. The Kirchhoff assumptions then are:

(1) S_l is locally considered as a perfectly planar reflector so that on S_l,

$$p(\underline{x}) = p^{in}(\underline{x}) + p^{r}(\underline{x}) \tag{10}$$

where $p^r(\underline{x})$ is the wave field as predicted by the reflection of the incident plane wave, $p^{in}(\underline{x})$, from an infinite planar free surface whose normal coincides with that of the flaw at point $\underline{x}$.

(2) The dark side S_d is in deep shadow so that $p(\underline{x}) = 0$ on S_d. This reduces the integration range in Eq. (9) to S_l only.

Noting that all the waves are in-phase on S_l, Eq. (10) becomes

$$p(\underline{x}) = (1 + R_f(\theta)) \exp(ik\, \underline{e}_i \cdot \underline{x}) \tag{11}$$

where $R_f(\theta)$ is the reflection coefficient

$$R_f(\theta) = \frac{\rho_2 c_2 \cos\theta - \rho_1 c_1 \cos\phi}{\rho_2 c_2 \cos\theta + \rho_1 c_1 \cos\phi} \tag{12}$$

and where θ is the incident angle and ϕ is the refracted angle ($\sin\phi = \kappa \sin\theta$ where $\kappa = c_1/c_2$) (Figure 3).

With the result of Eq. (11), the Kirchhoff assumption (2), and Eq. (9), we arrive at an explicit form for the far-field scattering amplitude given by

$$(13) \qquad f = -\frac{1}{4\pi}\int_{S_1} ik[(\underline{e}_s+\underline{e}_i)\cdot\underline{n} + R_f(\theta)(\underline{e}_s-\underline{e}_i)\cdot\underline{n}]\exp\{ik\,\underline{x}\cdot(\underline{e}_i-\underline{e}_s)\}\,dS(\underline{x})$$

Specular Reflection from an Inclusion

At high frequencies, Eq. (13) can be further evaluated by use of the method of stationary phase. In this case the far-field scattering amplitude is given by [22]

$$(14) \qquad f = \frac{1}{2} R_f(\theta)(R_1 R_2)^{\frac{1}{2}} \exp\{-ik(\underline{e}_s-\underline{e}_i)\cdot\underline{x}^s\}$$

where, $\underline{x}^s$ is the position vector of the specular reflection point, and R_1 and R_2 are the principal radii of the curvature of S at $\underline{x}^s$. In fact, this represents the front surface specular reflection from the flaw, which is the most significant part of the scattering signal. For an ellipsoid, we have

$$(15) \qquad f = \frac{1}{2} R_f(\theta)\frac{abc}{r_e^2}\exp\{-ik(\underline{e}_s-\underline{e}_i)\cdot\underline{x}^s\}$$

since, in this case $(R_1 R_2)^{\frac{1}{2}} = \dfrac{abc}{r_e^2}$

This result shows that the specular reflection is completely determined by the reflection coefficient and the local geometry of the scattering surface near the specular point. In the following section, we will show how Eq. (15) can be used in the development of the ABE sizing method.

Back Scattering from a Spherical Inclusion

For the special case of back scattering $\underline{e}_s = -\underline{e}_i$, Eq. (13) can be further reduced to

$$(16) \qquad f = -\frac{ik}{2\pi}\int_{S_1} \exp(2ik\,\underline{x}\cdot\underline{e}_i)\,R_f(\theta)\cos\theta\; dS(\underline{x})$$

where θ is the incident angle of the wave into the boundary (Figure 3). For a spherical inclusion with radius a, Eq. (16) gives

$$(17) \qquad f = -ika^2\int_{\theta=0}^{\pi/2} \exp(-2ika\cos\theta)\,R_f(\theta)\sin\theta\cos\theta\; d\theta$$

where θ is the angle defined in Figure 4. (Note that this is the same angle defined in Figure 3.) Even more specifically, for either a spherical void ($R_f = -1$) or rigid sphere ($R_f = 1$), $R_f(\theta)$ is a constant for all θ, so Eq. (17) can evaluated exactly as

$$(18) \qquad f = R_f \exp(-2ika)\left(-\frac{a}{2}+\frac{i}{4k}\right)-R_f\frac{i}{4k}$$

which has a corresponding impulse response, A(t), in the time domain with the time origin located at the center of the sphere as

$$(19) \qquad A(t) = -\frac{a}{2}R_f\,\delta\left(t+\frac{2a}{c_1}\right)+\frac{c}{4}R_f\left[H\left(t+\frac{2a}{c_1}\right)-H(t)\right]$$

where $\delta(\ )$ is the delta function and $H(\ )$ is the unit step function.

This result shows that the back scattering response from either a spherical void or a rigid sphere consists of two parts; the leading edge response from the specular point and a constant response from the lit part of the sphere. In a later section, we will show how Eq. (19) can be used as the motivation behind the approach in the FM method for determining the equivalent radius of the flaw.

AMPLITUDE-BASED EQUIVALENT FLAW SIZING METHOD

As mentioned previously, the scattering amplitude of the specular reflection of a 3-D scalar wave from a smooth convex fluid inclusion embedded in an otherwise homogeneous and isotropic fluid host, as shown in Eq. (14), is completely determined by two factors; the reflection coefficient and the local geometry of the scattering surface near the specular point. For an ellipsoidal flaw, the local geometry on the surface near the specular point can be defined by the semi-axis sizes of the ellipsoid (a, b, c) and the equivalent radius (r_e) at that point, as demonstrated in Eq. (15).

In most practical sizing situations one is interested in the more general case of an elastic flaw embedded in a solid host. Thus, the expression of Eq. (15) is not directly applicable. However, we can still apply Eq. (15) if we replace the fluid-fluid reflection coefficient of Eq. (12) with the coefficient for an elastic inclusion/solid host boundary. For the L (longitudinal) wave incident case, the L to L reflection coefficient $R_S(\theta)$ can be given by [23]

$$R_s(\theta) = \frac{(p_1 - p_3)(q_2 + q_4) - (p_2 + p_4)(q_1 - q_3)}{(p_1 + p_3)(q_2 + q_4) - (p_2 + p_4)(q_1 + q_3)} \tag{20}$$

where,

$p_1 = e/d$, $q_1 = s\cos\psi/d$, $p_2 = g/d\cot\varphi$, $q_2 = h\cot\psi/d\cot\varphi$, $p_3 = h\cot\phi/d\cot\theta$, $q_3 = -g/d\cot\theta$, $p_4 = -s\cot\theta/d$, $q_4 = p_1$, and

$d = \mu(b+2)$, $e = 2\mu+\mu'b'$, $s = 2(\mu-\mu')$, $g = \mu b-\mu'b'$, $h = 2\mu'+\mu b$,

$b = \cot^2\varphi - 1$, $b' = \cot^2\psi - 1$, where $\cot\theta = \sqrt{(c/c_{l1})^2 - 1}$, $\cot\varphi = \sqrt{(c/c_{s1})^2 - 1}$,

$\cot\phi = \sqrt{(c/c_{l2})^2 - 1}$, $\cot\psi = \sqrt{(c/c_{s2})^2 - 1}$, and $c = c_{l1}/\sin\theta$.

Here, c_{l1} is the longitudinal velocity in the solid host, c_{s1} is the shear velocity in the solid host, c_{l2} is the longitudinal velocity in the inclusion, c_{s2} is the shear velocity in the inclusion (Figure 5).

Using above reflection coefficient, the modified formula for the magnitude of the L to L ultrasonic scattering amplitude of the specular reflection with an incident angle of θ from an ellipsoidal elastic inclusion in a solid host can be given by

$$|f(\theta)| = \frac{1}{2}\,|R_s(\theta)|\,\frac{abc}{r_e^2} \qquad (21)$$

The ABE sizing method uses Eq. (21) as the basis for determining the best-fit equivalent ellipsoid from ultrasonic measurements taken at different transducer orientations.

Initial ABE Sizing Algorithm

Initially we chose an approach in which we sought to first determine the material properties of the flaw. In principle, Eq. (21) shows that this can be done by use of scattering amplitude ratios (the scattering amplitudes for various pitch-catch configurations (i.e. angle θ) divided by that at normal incidence) if

the specular point is held fixed since then the geometry dependent terms in Eq. (21) cancel out, leading reflection coefficient ratios which are only dependent on the flaw's material properties. For M pitch-catch measurements (Figure 6), a non-linear least squares minimization of the function

$$(22) \qquad I = \sum_{j=1}^{M} \left[\left(\frac{|R_s(\theta)|}{|R_s(0^o)|} \right)_j^{\text{model}} - \left\{ \frac{|f(\theta)|}{|f(0^o)|} \right\}_j^{\text{measured}} \right]^2$$

could then be used to determine the best-fit parameters (ρ_2, c_{l2}, c_{s2}) that match the measurements. Here, we expected that the scattering amplitude, $f(\theta)$, would be obtained experimentally from the ultrasonic signal using the measurement model developed by Thompson and Gray [24]. Once the material properties were estimated in this manner, the next step in this approach would be to determine the best-fit flaw geometry. This could be done using pulse-echo measurements at different transducer orientations (Figure 6 with $\theta = 0$). For N pulse-echo measurements, for example, we can minimize the function

$$(23) \qquad J = \sum_{j=1}^{N} \left[\left(\frac{r_e^2}{abc} \right)_j^{\text{model}} - \left\{ \frac{|R_s(0^o)|^{\text{calculated}}}{2|f(0^o)|^{\text{measured}}} \right\}_j \right]^2$$

where the reflection coefficient, $R_S(0^o)$, is calculated using information on the material properties, and recall r_e^2 is given by

$$(24) \qquad r_e^2 = \underline{n} \cdot \underset{\sim}{C} \underline{n}$$

Note that $\underline{n}$ is the same as $\underline{e}_q$ in Eq. (4) in this case. Solving the linear least squares optimization problem of Eq. (23) produces the best-fit C′ coefficients (where C′ = C/abc) and then solving the eigenvalue problem, similar to Eq. (7), gives the semi-axis sizes (as three eigenvalues of C) and orientations (as three corresponding eigenvectors) of the best-fit ellipsoid.

Unfortunately, in attempting to apply this algorithm, we found that it was not possible to determine the material flaw parameters from the minimization of the I function in Eq. (22), even when noise-free synthetic data was used. In attempting to understand the reasons for this failure, we plotted the normalized reflection coefficient ratios that appear in Eq. (22) for a wide variety of inclusion/host material combinations. Figure 7 shows a typical set of these results. As can be seen from Figure 7, the reason for the failure of this method lies in the fact that for angle θ below approximately 45°, the ratio $F(\theta) = R_s(\theta)/R_s(0^o)$ is nearly the same function, regardless of the inclusion/host properties. Since it would be difficult to obtain angles $\theta > 45^o$ in many practical situations, there is simply not enough leverage in the variation of F(θ) to solve Eq. (22). Although this negative result initially appears discouraging, the surprising fact that

$$R_s(\theta) = R_s(0^o)\, F(\theta) \tag{25}$$

where F(θ) is nearly a "universal" function for all flaw/material combinations and for θ not too large was used to motivate the FM method approach. First, however, we will describe a revised ABE sizing approach that does work.

Revised ABE Sizing Algorithm

In the revised algorithm, we return to Eq. (21) and note that by making a series of pulse-echo scattering amplitude measurements at different transducer orientations and then dividing those results by a single "reference" scattering amplitude measurement made at an arbitrary but fixed transducer orientation, the resulting ratio would be equivalent to a scaled equivalent radius calculation. Explicitly, for the j-th pulse-echo measurement divided by the r-th (reference) measurement, we have

$$(26) \qquad \frac{(r_e^2)_j}{(r_e^2)_r} = \left(\frac{r_e}{K}\right)_j^2 = \frac{|f(0^o)|_r}{|f(0^o)|_j}$$

where K is the scale factor (defined by the equivalent radius, r_e, of the r-th measurement). Then for N pulse-echo measurements, we can form up the function

$$(27) \qquad I_2 = \sum_{j=1}^{N} \left[\left(\frac{r_e^2}{K^2}\right)_j^{\text{model}} - \left\{ \frac{|f(0^o)|_r}{|f(0^o)|_j} \right\}^{\text{measured}} \right]^2$$

and search for the best-fit parameters C" (where $C'' = C/K^2$) by solving a linear least squares problem involving the function I_2. Thus, by solving the eigenvalue problem for the scaled matrix C" , as described previously, we can obtain the scaled sizes of the semi-axis (a/K, b/K, c/K) and the orientations ($\underline{e}_a$, $\underline{e}_b$, $\underline{e}_c$) of the best-fit ellipsoid. We should point out that one major difference between Eq. (27) and Eq. (23) is that Eq. (27) only involves relative amplitude

information. Consequently, results based on Eq. (27) should be less sensitive to various sources of error, such as flaw surface roughness.

Since we can find a scaled equivalent ellipsoidal flaw (scaled by factor of 1/K), from the above procedure, we need only to determine the scale factor K to finally get the "correct" equivalent flaw. One way in which this factor can be determined is to use the approach described above which defines a series of scaled equivalent radius values, $(r_e^{scaled})_j$ at different transducer orientations and then use any of the algorithms used previously (such as the inverse Born approximation coupled with a zero-of-time determination method) for estimating unscaled r_e values $(r_e^{unscaled})_j$ at the same transducer orientations. Then the scale factor K could be determined through a simple averaging process as

$$K = \frac{1}{N} \sum_{j=1}^{N} \left(\frac{r_e^{unscaled}}{r_e^{scaled}} \right)_j \tag{28}$$

Although this method would still contain the same errors present in current procedures (due to, for example, difficulties in measuring accurately a zero-of-time), in this case the errors should be less important since we are only using the experimentally determined $r_e^{unscaled}$ to estimate the single constant K and the averaging process should help to reduce the significance of these errors.

Implementation of the ABE Sizing Method

The revised ABE sizing algorithm has been implemented in FORTRAN 77 on a VAX computer. In this program, an IMSL subroutine, DLSQRR, which can solve a linear least squares problem without iterative refinement, was

adopted to solve the linear optimization problem of Eq. (27). Another IMSL subroutine, DEVCSF, was selected as a tool for solving the eigenvalue problem to determine the best-fit ellipsoid. To get the inputs for this program, we have used either synthetic data, taken with at least 6 different $\underline{e}_q$ values, or experimental data, taken at 6 or more different transducer orientations, and then processed through the measurement model [24] to obtain the necessary scattering amplitudes.

Performance of the ABE Sizing Method

For the initial test of the ABE method, "exact" synthetic data was generated for known flaws immersed in a single medium using 19 measurements over a one-sided scanning aperture angle of 120 degrees (Figure 8). Two different flaw shapes were considered: a round ellipsoid and a pancake-like flat ellipsoid, both of which have the same orientation but different sizes. As shown in Table 1, the ABE method gave the "exact" results (flaw size and orientation) for both cases.

As an initial experimental verification of this method, equivalent flaw sizing was done for a 1/4 inch (6.35 mm) diameter steel sphere immersed in water. The specific apparatus used in this work was an automated multiviewing ultrasonic transducer system developed by Thompson and et. al. [25]. This fully automated system can provide very precise information about the transducer orientation, which is needed for the application of the ABE method. In one-sided conical scanning, a total of 19 measurements were taken at different transducer orientations (as depicted in Figure 8). Since it was not practical to determine the equivalent radius experimentally for such a large flaw, the exact radius of the sphere was considered as the $r_e^{unscaled}$. As shown in

Table 2, the ABE method produced results with a maximum error in the semi-axis size estimation of about 0.05 mm.

Since this initial experimental test of the ABE sizing method was very encouraging, we also applied this method to a more realistic flaw. Equivalent flaw sizing was done for a 380 μm flat circular crack (actually a 380x380x45 μm thin flat disk-shaped cavity with the flat-bottom face parallel to the specimen surface) placed in titanium alloy (Ti-6Al-4Vd: $\rho = 4.42$ g/cm^3, $c_l = 0.634$ cm/μsec, $c_s = 0.303$ cm/μsec). Fortunately for this flaw the scattering amplitude data at 13 different transducer tilting angles and the equivalent radius ($r_e^{unscaled}$) data estimated from "flash point distance" measurements were available [6]. Originally these data were taken at the same azimuthal angle, but this type of scanning pattern is known to be very poor for any equivalent flaw sizing algorithm [6]. Thus, the azimuthal angles for all data were artificially changed to angles between 0° and 360°. This type was replacement was possible because for the given crack orientation the equivalent radius data should be independent of the azimuthal angle [6]. From the available waveforms for scattering amplitudes, the magnitudes were measured. Examination of the data set showed that there were two data points that had particularly large errors. Table 3 shows the ABE sizing results with and without these "bad" data points. For the data set without these bad data points (11 data points total) the ABE method produced reasonably good results for both size and orientation with the maximum error in size estimation for the semi-axis of the crack of about 12%, which is much less than the average error in the equivalent radius estimation of 21%.

In summary, the ABE sizing algorithm showed very good performance on both the synthetic and experimental data sets. In the sizing of the crack in the titanium alloy it was shown that this method was indeed able to reduce error caused by the equivalent radius measurement (or equivalently the zero-of-time problem) as postulated earlier. Even though this method showed very good performance in the case of a large flaw (a 1/4 inch diameter steel sphere), its real usefulness lies in its ability to deal with very small flaws where other methods fail. The method is computationally efficient and stable, and relatively insensitive to various sources of error because it uses relative amplitude information.

FIRST MOMENT FLAW SIZING METHOD

The equivalent radius is the one of the basic parameters in most current equivalent flaw sizing algorithms. This information is normally obtained directly from the ultrasonic waveform itself using signal processing. Unfortunately, most current methods suffer from the zero-of-time problem. In this section, we will address a new first moment (FM) method which can determine the equivalent radius accurately and hence provide a solution to the zero-of-time problem. The algorithm and the performance of this method will be presented.

The FM Method Algorithm

From our previous results, Eq. (19), the impulse response function, A(t), of a scalar wave from either a spherical void or a rigid sphere in a fluid medium by the Kirchhoff approximation is composed of two parts; the leading edge response from the specular point and the constant response from the lit region of the sphere. (Figure 9). If we calculate the first moment of this theoretical response starting from the peak point of the leading edge response as

$$(29) \qquad FM(\delta t) = \int_0^{-\delta t} \tau \cdot A(-2a/c_1 + \delta t + \tau)\, d\tau$$

it is simple to show that the first moment will be zero when $\delta t = 2a/c_1$ (Figure 9a), which corresponds to the center of the spherical void.

For the more general case of a fluid or solid inclusion (Eq. (17)), Fourier inversion provides a pulse-echo impulse response, A(t), given by

$$(30) \qquad A(t) = \frac{d}{dt}\frac{a^2}{c_1}\int_{\theta=0}^{\pi/2} \delta(t + 2a\cos\theta/c_1)\, R(\theta)\sin\theta\cos\theta\, d\theta$$

where $R(\theta) = R_f(\theta)$ for the fluid inclusion in a fluid host or $R(\theta) = R_s(\theta)$ for a solid inclusion in a solid host.

Based on our previous results (Eq. (25)) we note that in Eq. (30) we can write $R_s(\theta) = R(0^o)\, F(\theta)$ where $F(\theta)$ is nearly a universal function for all flaw/host combinations if θ does not differ too greatly from the back scatter direction ($\theta = 0^o$ here). In fact, since the product $\sin\theta\cos\theta$ vanishes at both of the end points of the integration in Eq. (30), it is easy to see that this behavior suppress even further the differences in the total product $R_s(\theta)\sin\theta\cos\theta$ and we can say that $R_s(\theta)\sin\theta\cos\theta = R_s(0^o)\, G(\theta)$ where $G(\theta)$ is nearly a universal function for the entire intergration range. A similar result can be shown to be true also for the fluid case, i.e. $R_f(\theta)\sin\theta\cos\theta = R_f(0^o)\, G'(\theta)$ where again G' is nearly a universal function. The significance of both of these results lies in the fact that when we compute the time δt when the first moment of the impulse response in Eq. (30) is zero, δt will be a strong function only of the true equivalent radius of the flaw and not its material properties.

Thus, in principle, one should be able to use our model (Eq. (30)) to develop a calibration curve that is relatively insensitive to the material characteristics of the flaw and relates the true equivalent radius of the flaw to the value calculated from the condition $FM(\delta t) = 0$. When R_f is used to generate such a calibration curve, we will henceforth refer to it simply as the "fluid model." Similarly when R_s is used, we will refer to it as the "solid model." To

examine the behavior of both these models, initially we used a series of tests with synthetic data.

Initial Tests

Since all real signals are bandlimited (Figure 9b), it was important to introduce the effects of this loss of frequency information. This was done by not employing Eq. (30) directly but by instead using the original frequency domain results (Eq. 17) with either R_f or R_s in the integrand and then calculating the time domain response via Fourier transformation as

$$(31) \qquad A(t) = \frac{1}{2\pi} \int_{\omega=-\infty}^{\infty} f(\omega)\, B(\omega) \exp(-i\omega t)\, d\omega$$

where $f(\omega)$ is the scattering amplitude in the frequency domain (defined by Eq. (17)) and $B(\omega)$ is the transducer bandwidth function (defined as $B(\omega) = 1$ inside the transducer bandwidth and $B(\omega) = 0$ outside).

By using this resulting A(t), we could then calculate a calibration curve for different flaw materials to see how universal such curves really were. However, in order to do such calculations reliably, we discovered that we had to consider two key issues. They were; 1) to find the peak point of the leading edge response correctly from a digitized time domain flaw response, and 2) to handle a problem with the accurate determination of the first moment condition for large flaws.

The first issue arose because normally the peak point of the leading edge response was not sampled (unless the flaw size precisely matched with the integer times of the time sampling resolution). This quite often introduced

significant errors in the size estimation in the FM method even using synthetic data. As a remedy of this problem, we adopted a curve fitting of the leading edge response to a quadratic function. Accurate curve fitting required more data points on the leading edge response, than our "nominal" simulated sampling period of 9.76 nsec. Thus, we increased the data points of the waveform by a factor of 4 (so that the sampling period was reduced to 2.44 nsec) by the well-known technique of zero-padding in the frequency domain. After this interpolation the peak point could be determined very accurately from the curve fitted data for most practical situations.

The other problem we encountered was that for "large" flaws (near 1 mm in size) the first moment calculations had significant oscillations in them, often resulting in a zero-crossing point quite far from the true value. To suppress these oscillations, we chose to shift the starting point of the first moment calculation to the right of the peak point of the leading edge response, and consequently considered only a portion of the leading edge response in the first moment calculation (Figure 10). In this study, we chose the starting point, t_{start}, as

$$t_{start} = 0.25\,(t_{zero} - t_{peak}) + t_{peak} \tag{32}$$

where,

t_{zero} is the first zero-crossing point of the time domain flaw response after the peak point, and t_{peak} is the peak point of the leading edge response of the time domain flaw response.

Although this starting point shift cures the problem with oscillations for the larger flaws it also biases the FM method to produce estimated flaw sizes much smaller than the actual size. But since this bias is incorporated in the calibration curve anyway, it does not pose a serious problem.

Performance of the FM Method

For the experimental verification of the FM method with the modifications mentioned above, we chose two kinds of flaws; 1) a 350 μm radius spherical void ($\rho = 0.0012$ g/cm^3, $c_l = 0.033$ cm/μsec, $c_s = 0.0$ cm/μsec) in fused silica ($\rho = 2.2$ g/cm^3, $c_l = 0.597$ cm/μsec, $c_s = 0.367$ cm/μsec) and 2) a 1/32 inch (794 μm) radius steel sphere ($\rho = 7.8$ g/cm^3, $c_l = 5.9$ cm/μsec, $c_s = 3.1$ cm/μsec) embedded in thermoplastic material (Buehler's transoptic: $\rho = 1.18$ g/cm^3, $c_l = 0.272$ cm/μsec, $c_s = 0.135$ cm/μsec). These are nice examples of flaws with both high (a steel sphere) and low (a spherical void) acoustic impedance embedded inside materials.

For each flaw, the far-field scattering amplitude in backscatterer was calculated from the time domain flaw signal and the reference signal (front surface reflection for the fused silica case and back surface reflection from an unflawed specimen for the thermoplastic case) measured by a pulse-echo set-up by use of the measurement model [24]. Then the interpolated time domain flaw response was obtained by use of zero-padding in the frequency domain and the Fourier transform. From this response, the first moment was calculated as a function of δt beginning with the starting point defined by Eq. (32), and then the time δt which made the first moment be zero was found. Finally this time δt was converted to the flaw size by $a = c_l \delta t/2$ since the L wave was used in the experiments.

For the same inclusion/host combinations, synthetic data sets were generated using the procedure similar to that for the experiments. The transducer bandwidth measured from the transducer used in the experiments were used for the determination of the calibration curves. Figures 11a shows the calibration curves constructed for spherical voids in fused silica using the fluid model and the solid model together with the experimental data for a 350 μm radius spherical void embedded in the same host. Figure 11b shows the similar calibration curves for spherical steel inclusions in the thermoplastic material and the experimental data for a 1/32 inch (794 μm) radius steel sphere embedded in the same host. In both cases, the experimental data agree with the solid model calibration curves, which implies that solid model is needed to adequately describe the physics of the scattering process. Thus, we chose the solid model curves for all subsequent analysis.

Figure 12a shows the sizing result for the 350 μm radius spherical void embedded in fused silica using the best-fit line for the calibration curve (using the solid model) for voids in the same host. The estimated size for the actual 350 μm void by the FM method was 319 μm with an estimation error of about 8.9%. Figure 12b shows the similar result for the 1/32 inch (794 μm) radius steel sphere embedded in the thermoplastic material. In this case, the estimated size was 893 μm with an estimation error of about 12.5%.

Figures 13a, b show the calibration curves for a wide variety of inclusions in fused silica and a thermoplastic, respectively. As can be seen from those figures, there is some significant variation in the calibration curves so that a single universal best-fit line produced through an averaging process will likely lead to larger than desirable sizing errors. However, one can define two distinct

best-fit lines, one for flaws whose impedance is less than that of the host and one for flaws of greater impedance than the host. These separate lines are useful since the discrimination of flaws according to their relative acoustic impedance can be easily done using the observed polarity of the leading edge response in the time domain. High impedance flaws have positive polarity while low impedance flaws have negative polarity. Figure 13a also shows the sizing result for the 350 μm radius spherical void embedded in fused silica. Calibration curves for four typical inclusions (void, water, steel, tungsten) were constructed and two best-fit lines were determined. In this case, the estimated size was 358 μm with the estimation error of about 2.3%. Figure 14b shows the similar result for the 794 μm radius steel sphere embedded in the thermoplastic material. The FM method produced the estimated size of 791 μm with the estimation error of about 0.4%.

The FM method showed very good sizing performance on both flaws with the maximum estimation error of about 12.5%. It was also shown that this method was able to estimate accurately the size of a relatively small flaw (< 1 mm) even without exact flaw type information in advance. Thus, this is indeed a viable method which both solves the zero-of-time problem and can determine flaw sizes for very small flaws. In addition, this method is very simple to implement so that we feel it can be applied to many practical applications. Although the FM method was only tested here on spheres, it should be able to be used to estimate equivalent radii in more general situations, and when combined with the linear least squares/ eigenvalue approach, produce best-fit equivalent ellipsoids. Demonstration of these capabilities, however, will be done in future studies.

SUMMARY

We have described two new approaches to equivalent sizing for relatively small flaws; a amplitude-based equivalent (ABE) sizing method and a first moment (FM) method.

The ABE sizing method uses the ratios of specular reflection amplitudes from a flaw measured at different transducer orientations to determine the best-fit ellipsoid. This method showed very good performance on both synthetic and experimental data sets. In the sizing of a crack in titanium alloy it was shown that this method was able to reduce errors caused by the equivalent radius measurement. Furthermore, this method is computationally efficient and stable since this approach adopted the linear least squares/ eigenvalue approach to find the best-fit flaw parameters that match the measurement data.

The FM method is a new approach which can determine the flaw size accurately by use of the first moment calculation of the time domain flaw response. In this study, this method showed very good size estimation performance for both high and low impedance flaws even without exact flaw type information in advance. Thus it is indeed a viable method which both solves the zero-of-time problem and can determine sizes of small flaws.

Finally, the excellent performance of the two methods observed in this study suggest that they can serve as robust tools for many practical sizing problems.

ACKNOWLEDGEMENTS

One of the authors, S. J. Song, would like to thank Dr. C. P. Chiou for his valuable discussions. This research was supported by the Center for Nondestructive Evaluation at Iowa State University.

REFERENCES

1. J. Krautkramer and H. Krautkramer, Ultrasonic Testing of Materials, 4th Edition, New York: Springer-Verlag, 1990.

2. C. F. Schueler, H. Lee and G. Wade, "Fundamentals of digital ultrasonic imaging." IEEE Transactions on Sonics and Utrasonics, Vol. SU-31. pp. 195-217, 1984.

3. D. K. Hsu, J. H. Rose and D. O. Thompson, "Reconstruction of inclusions in solids using ultrasonic Born inversion." Journal of Applied Physics, Vol. 55, pp. 162-168, 1984.

4. D. K. Hsu, D. O. Thompson and S. J. Wormley "Reliability of reconstruction of arbitrarily oriented flaws using multiview transducers." IEEE Transactions of Ultrasonics, Ferroelectrics, and Frequency Control, Vol. UFFC-34, pp. 508-514, 1987.

5. A. Sedov and L. W. Schmerr, "The time domain elastodynamic Kirchhoff approximation for cracks: the inverse problem." Wave Motion, Vol. 8, pp. 15-26, 1986.

6. L. W. Schmerr, A. Sedov and C. P. Chiou, "A unified constrained inversion model for ultrasonic flaw sizing." Research in Nondestructive Evaluation, Vol. 1, pp. 77-97, 1989.

7. C. P. Chiou and L. W. Schmerr, "New approaches to model-based ultrasonic flaw sizing." to appear in Journal of Acoustical Society of America.

8. S. J. Song and L. W. Schmerr, "An ultrasonic time-of-flight equivalent flaw sizing method." to be submitted to Research in Nondestructive Evaluation.

9. L. J. Bond, C. A. Chaloner, S. J. Wormley, S. P. Neal, and J. H. Rose, "Recent advances in Born Inversion (weak scatterers)." in Review of Progress in Quantitative Nondestructive Evaluation, Eds. D. O. Thompson and D. E. Chimenti, Vol. 7A, pp. 437-444, New York: Plenum, 1988.

10. C. A. Chaloner and L. J. Bond, "Investigation of the 1-D inverse Born technique." IEE Proceedings, Vol. 134, Pt. A, pp. 257-265, 1987.

11. S. J. Song and L. W. Schmerr, "Ultrasonic flaw sizing - some new approaches," to appear in Review of Progress in Quantitative Nondestructive Evaluation, Eds. D. O. Thompson and D. E. Chimenti, Vol. 11, New York: Plenum, 1992.

12. J. E. Gubernatis, E. Domany, J. A. Krumhansl, and M. Huberman, "The Born Approximation in the theory of the scattering of elastic waves by flaws." Journal of Applied Physics, Vol. 48, pp. 2812-2819, 1977.

13. J. H. Rose and J. A. Krumhansl, "Determination of flaw characteristics from ultrasonic scattering data." Journal of Applied Physics, Vol. 50, pp. 2951-2952, 1979.

14. J. H. Rose and J. M. Richardson, "Time domain Born approximation." Journal of Nondestructive Evaluation, Vol. 3, pp. 45-53, 1982.

15. J. H. Rose, R. K. Elsley, B. R. Tittman, V. V. Varadan, and V. K. Varadan, "Inversion of ultrasonic scattering data." in Acoustic, Electromagnetic, and Elastic Wave Scattering - Focus on the T-Matrix Approach, Eds. V. K. Varadan and V. V. Varadan, New York: Pergamon Press, pp. 605-614, 1980.

16. J. H. Rose and J. L. Opsal, "The inverse Born approximation: exact determination of shape of convex voids." in Review of Progress in Quantitative Nondestructive Evaluation, Eds. D. O. Thompson and D. E. Chimenti, Vol. 2b, pp. 949-959, New York: Plenum, 1985.

17. R. B. Thompson and T. A. Gray, "Range of applicability of inversion algorithms." in Review of Progress in Quantitative Nondestructive Evaluation, Eds. D. O. Thompson and D. E. Chimenti, Vol. 1, pp. 233-249, New York: Plenum, 1982.

18. F. Cohen-Tenoudji, G. Quentin and B. R. Tittmann, "Elastic wave inversion transformation." in Review of Progress in Quantitative Nondestructive Evaluation, Eds. D. O. Thompson and D. E. Chimenti, Vol. 2B, pp. 961-974, New York: Plenum, 1982.

19. L. S. Koo, "Ultrasonic flaw classification: an approach using modelling, signal processing, and adaptive learning." Ph.D. Dissertation, Iowa State University, 1987.

20. J. Yang and L. J. Bond, "Errors in determining the flaw centroid by using area functions." to appear in Review of Progress in Quantitative Nondestructive Evaluation, Eds. D. O. Thompson and D. E. Chimenti, Vol. 11, New York: Plenum, 1992.

21. J. D. Achenbach, A. K. Gautesen and H. McMaken, Ray Methods for Waves in Elastic Solids, Boston: Pitman, 1982.

22. J. S. Chen, "Elastodynamic ray theory and asymptotic methods for direct and inverse scattering problems." Ph.D. Dissertation, Iowa State University, 1987.

23. J. Miklowitz, The Theory of Elastic Waves and Waveguides. New York: North-Holland, 1978.

24. R. B. Thompson and T. A. Gray, "A model relating ultrasonic scattering measurements through liquid-solid interfaces to unbounded medium scattering amplitudes." Journal of the Acoustical Society of America, Vol. 74, pp. 1279-1646, 1983.

25. D. O. Thompson, S. J. Wormley, and D. K. Hsu, "Apparatus and technique for reconstruction of flaws using model-based elastic wave inverse ultrasonic scattering." Review of Scientific Instruments, Vol. 57, pp. 3089-3098, 1986.

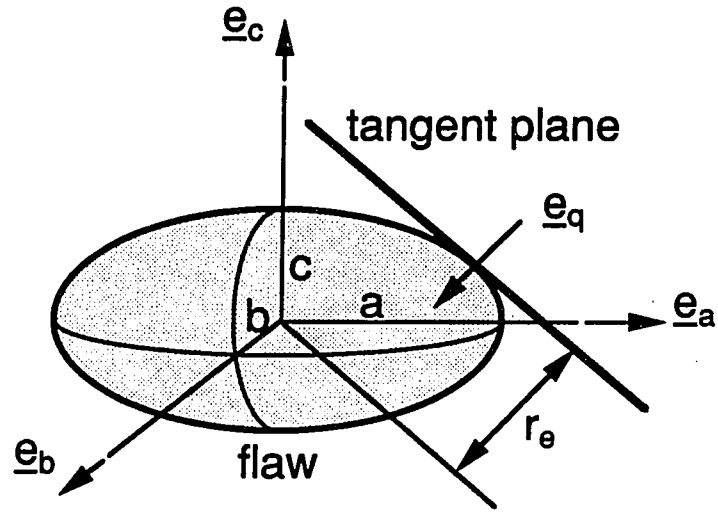

Figure 1. Ellipsoidal geometry and the definition of the equivalent radius, r_e

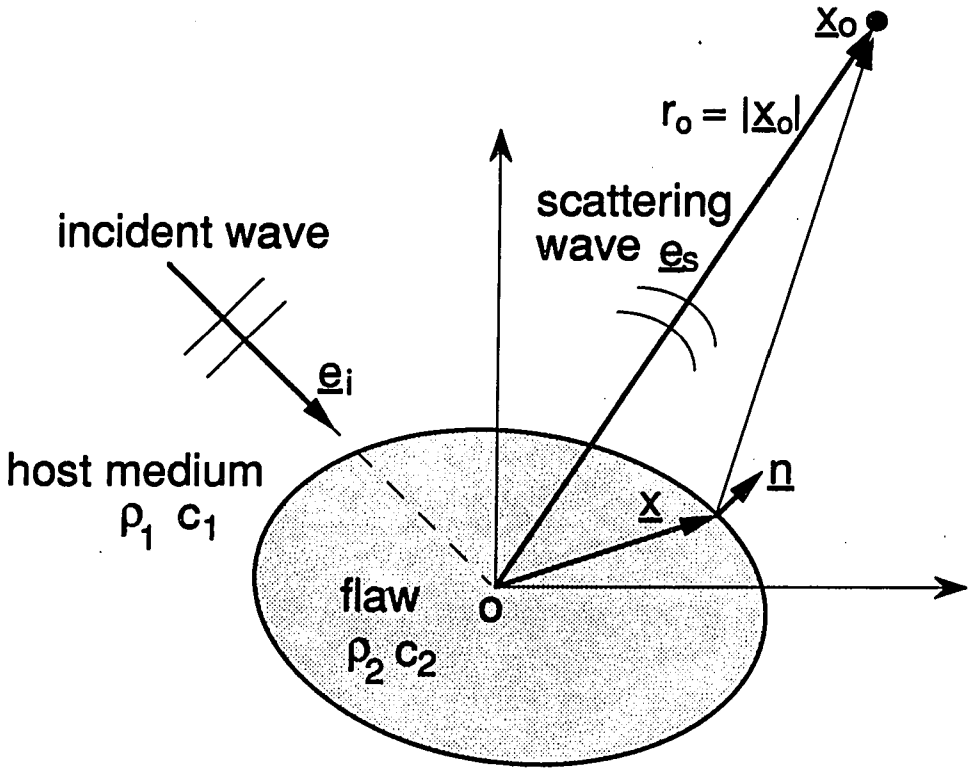

Figure 2. Flaw scattering geometry

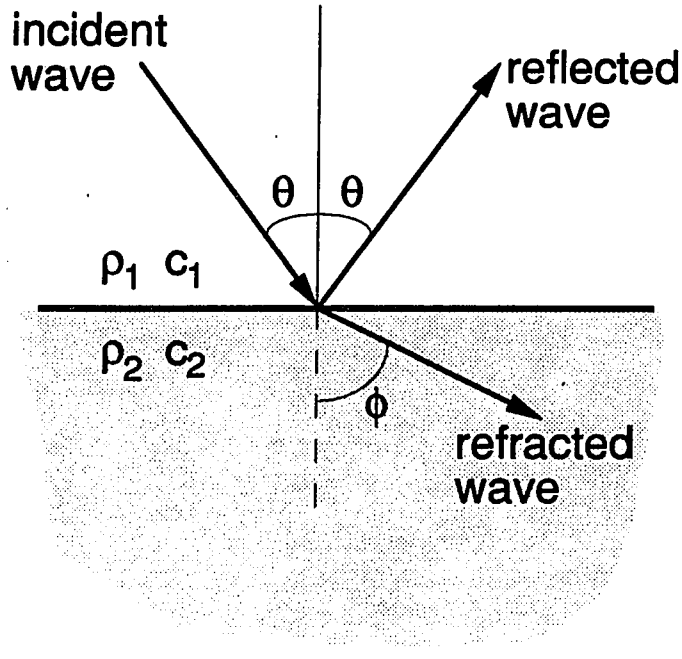

Figure 3. Reflection geometry for plane wave incident on fluid/fluid boundary

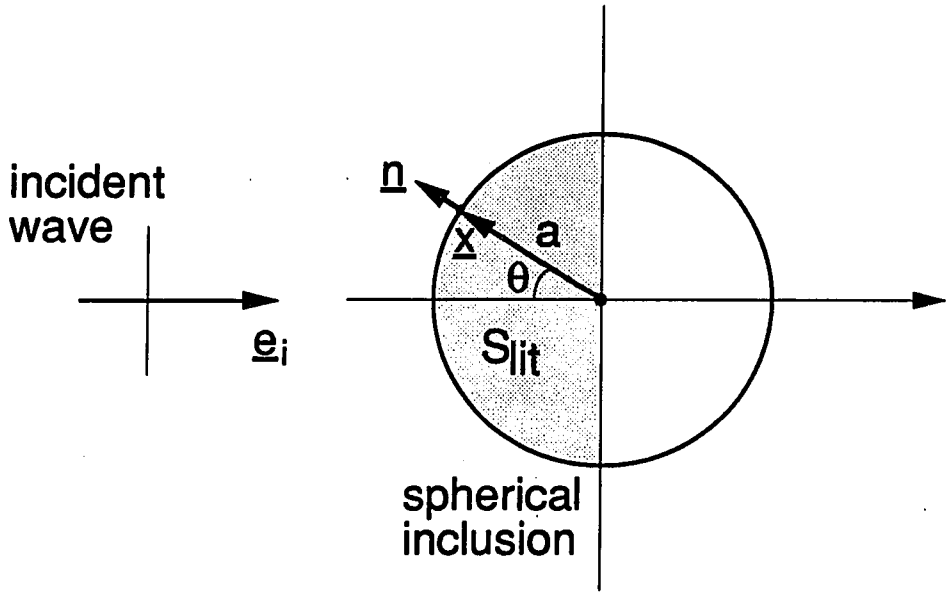

Figure 4. Scattering geometry from a spherical inclusion

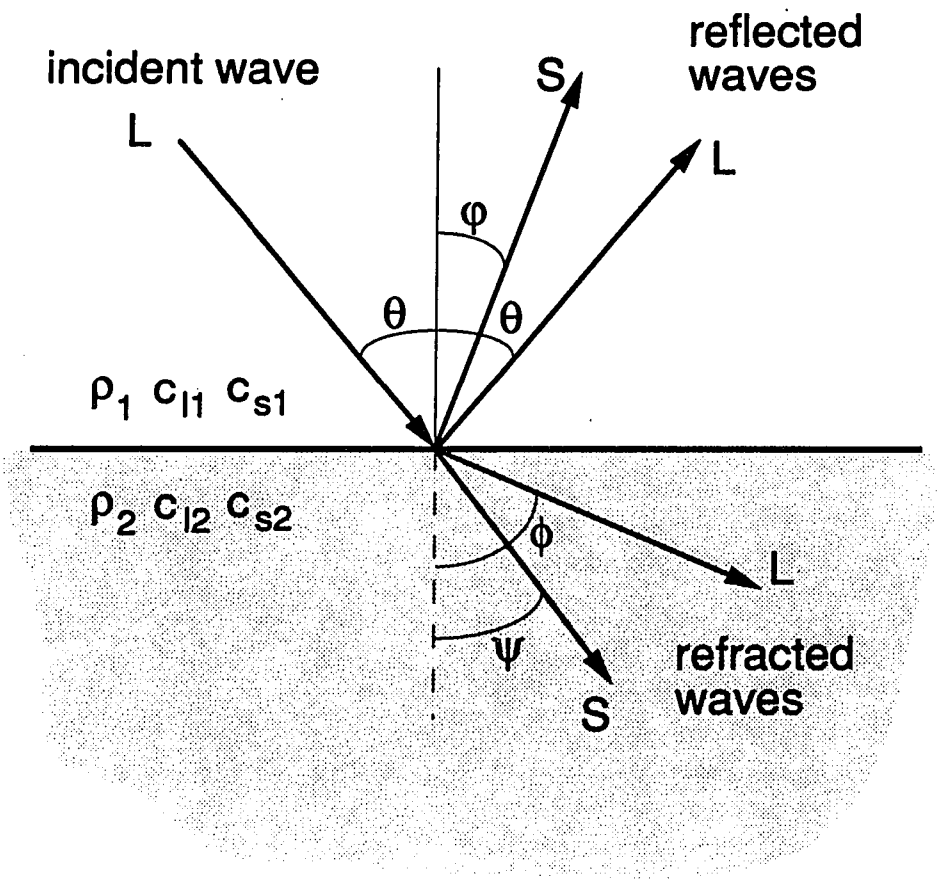

Figure 5. Reflection geometry for plane L wave incident on solid/solid boundary

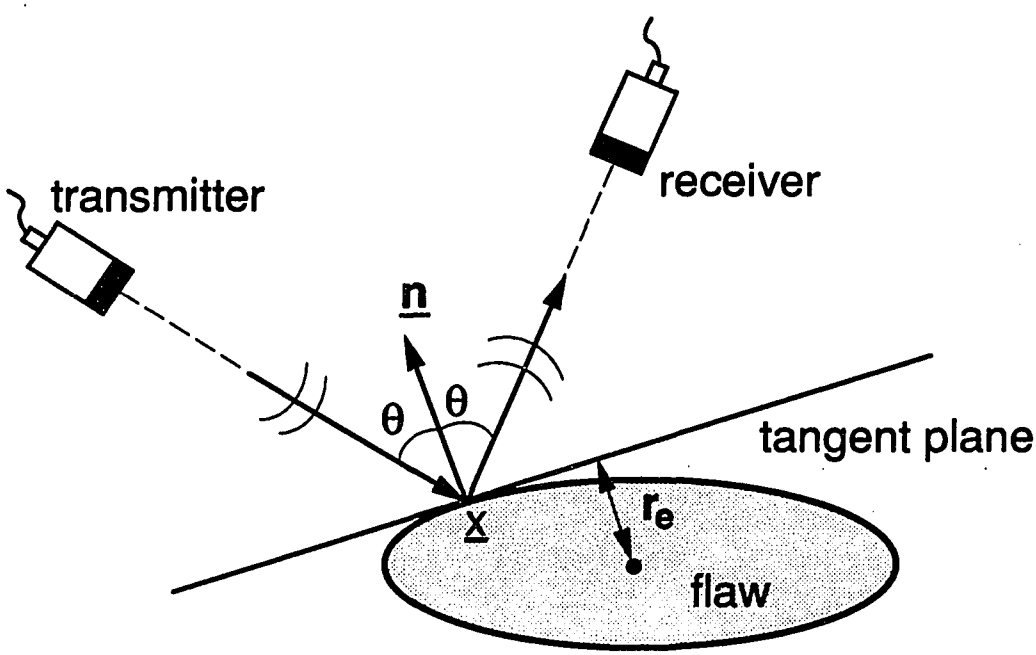

Figure 6. Pitch-catch ultrasonic measurement set-up

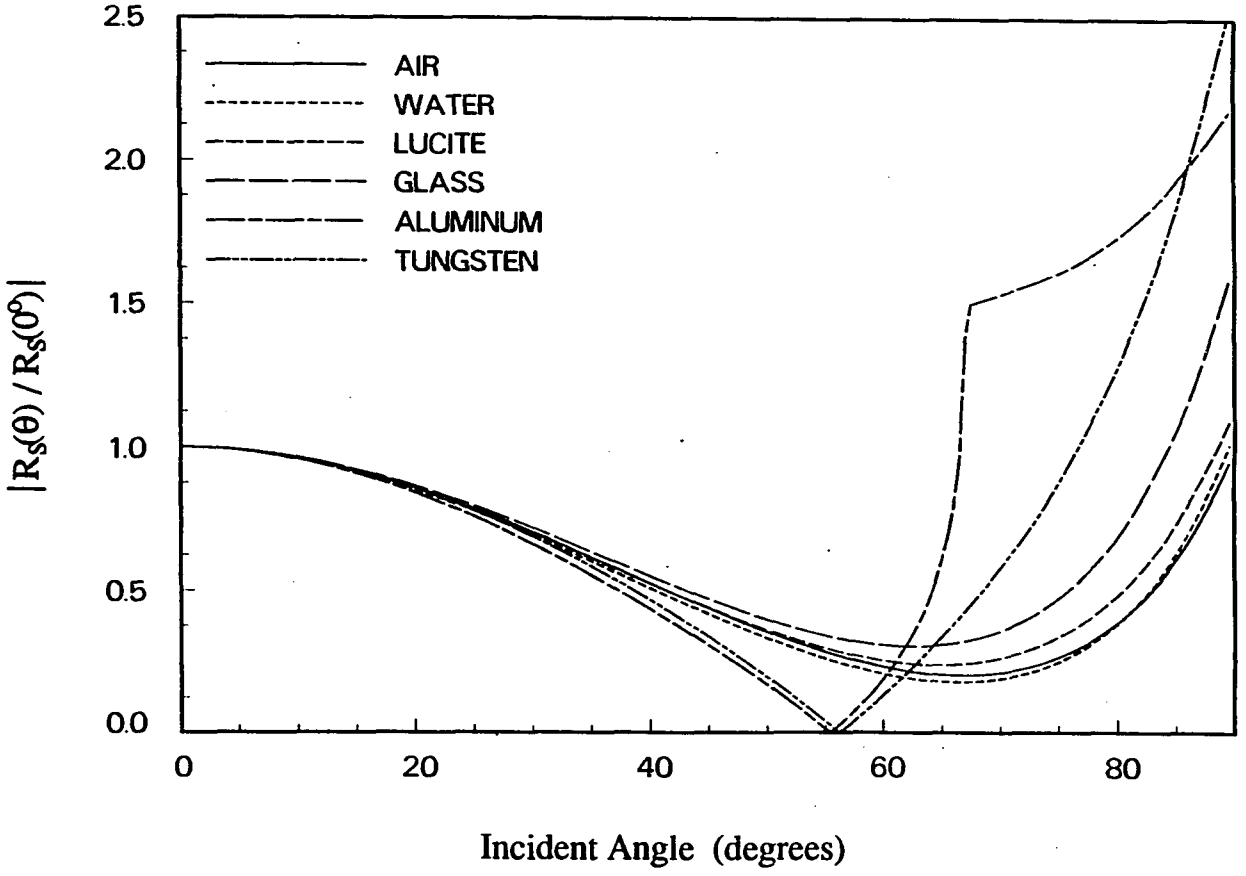

Figure 7. Variation of normalized L to L reflection coefficient ratios, $|Rs(\theta)/Rs(0^{\circ})|$, for various inclusions embedded in a solid host according to the incident angle θ. Host: steel, Inclusions: air, water, lucite, glass, aluminum, and tungsten.

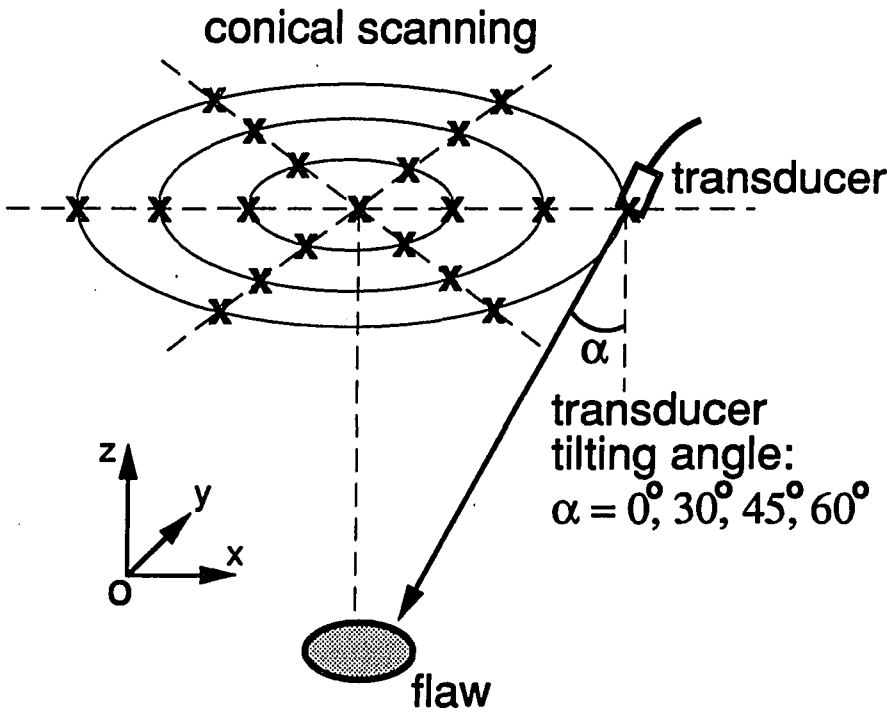

Figure 8. Schematic diagram of one-sided conical scanning ("x" denotes a measurement point.)

Table 1. ABE sizing results for error free synthetic data

(unit : μm)

Shape	Parameter	Actual	Estimated
Round Ellipsoid			
	a	400	400
	b	500	500
	c	600	600
Flat Ellipsoid			
	a	400	400
	b	500	500
	c	100	100

Table 2. ABE sizing result for a 1/32 inch (3.175 mm) radius steel sphere immersed in water.

(unit : mm)

Parameter	Actual	Estimated
a	3.175	3.130
b	3.175	3.227
c	3.175	3.182

Table 3. ABE sizing results for a "crack" in a titanium alloy

(unit : μm)

Parameter	Actual	Estimated	
		(with 11 data)	(with 13 data)
a	380	354	368
b	380	335	237
c	45	65	79

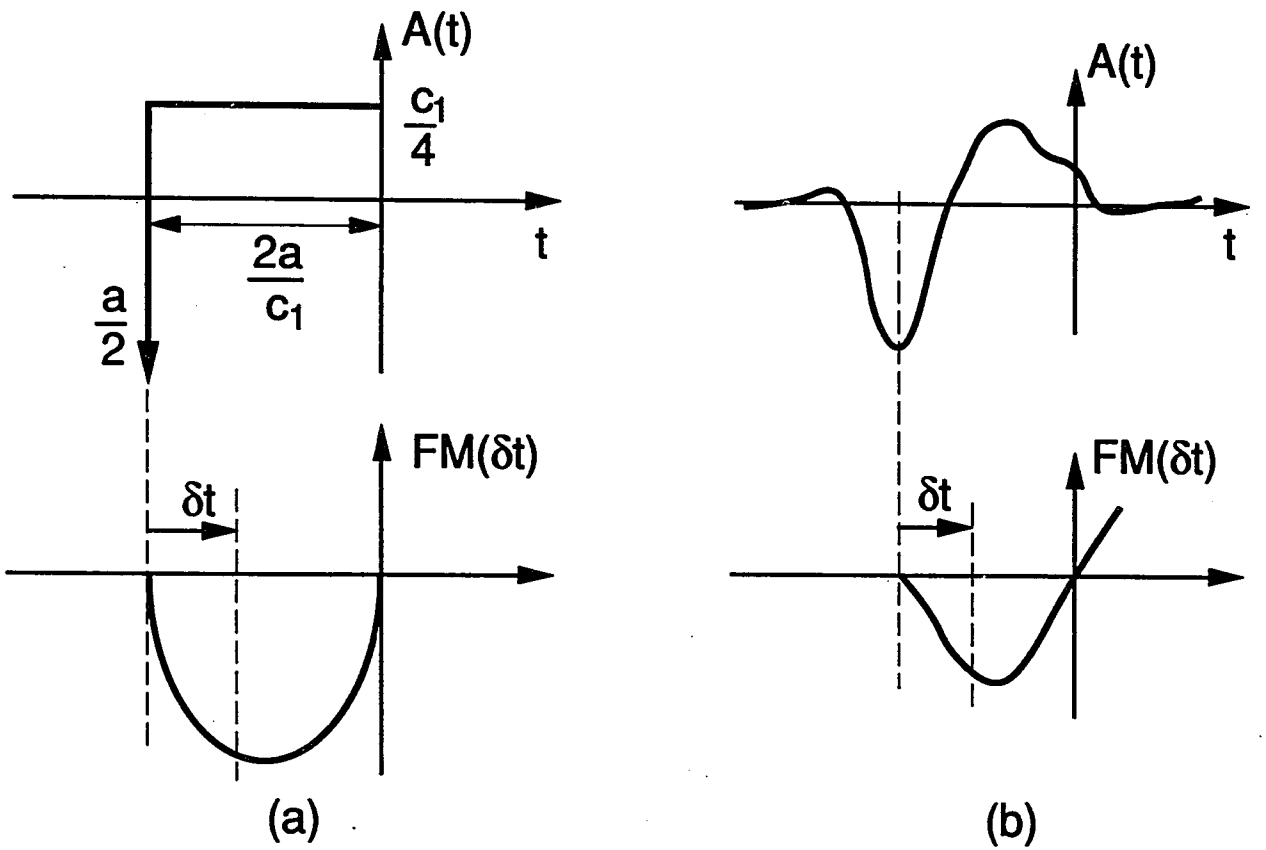

Figure 9. Time domain flaw response from a spherical void for (a) an infinite bandwidth case, and (b) a finite bandwidth case

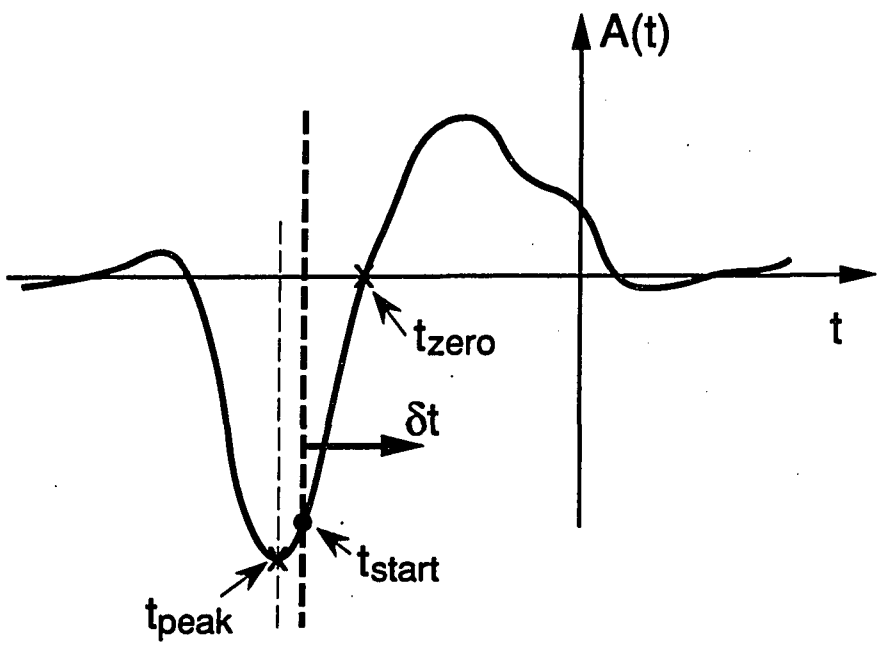

Figure 10. Starting point of the first moment calculation of the time domain flaw response

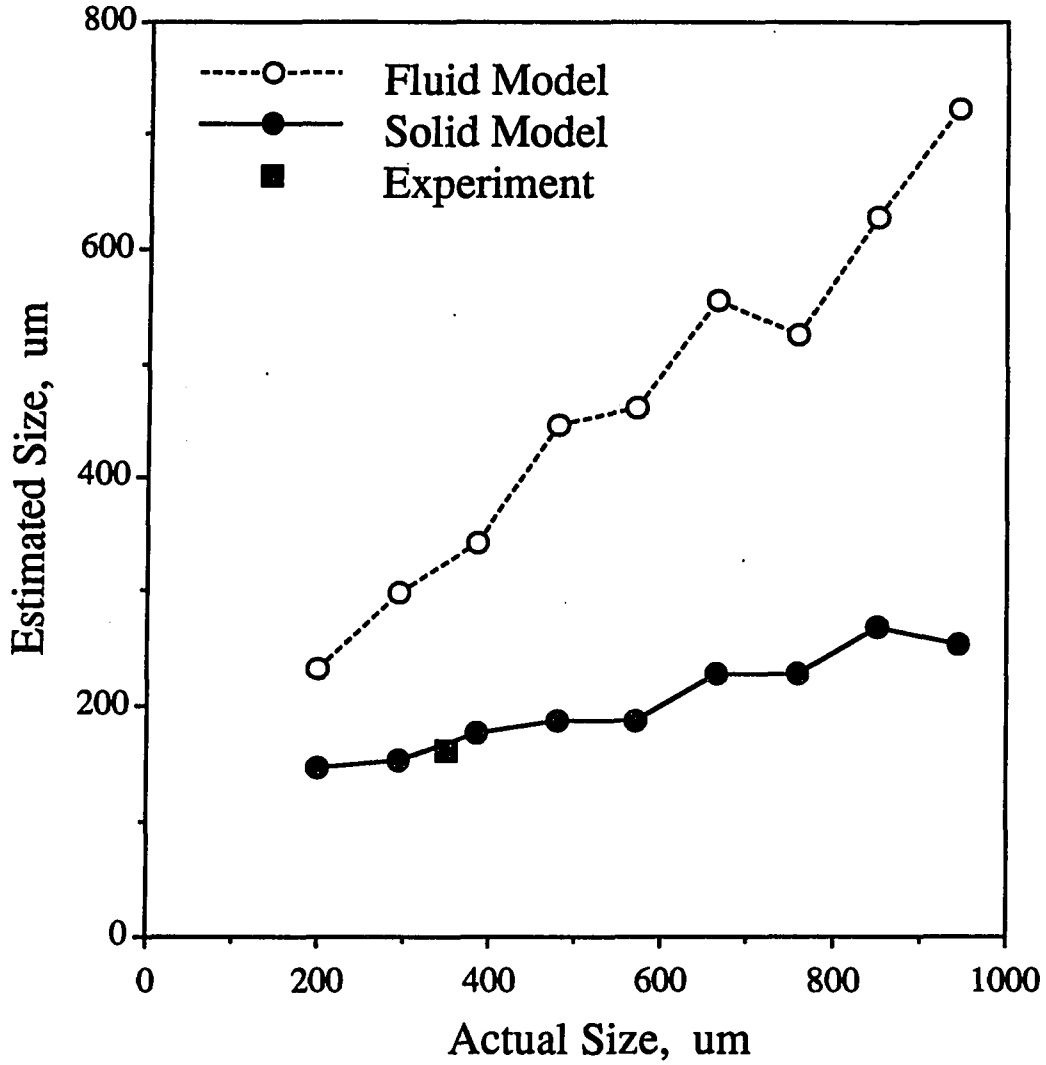

Figure 11a. Comparison of calibration curves (constructed using the fluid model and the solid model for spherical voids embedded in fused silica) with the experimental data for a 350 μm radius spherical void embedded in the same host.

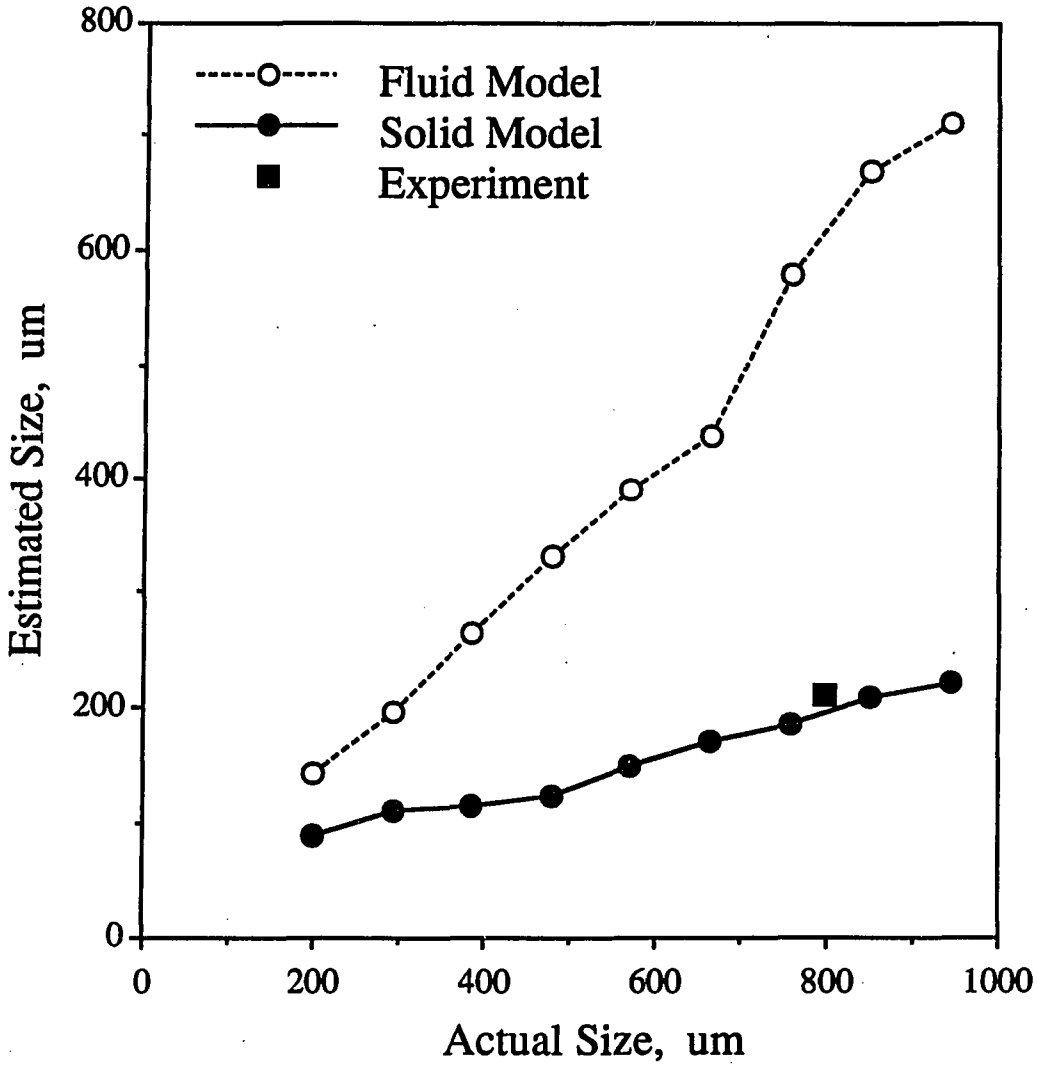

Figure 11b. Comparison of calibration curves (constructed using the fluid model and the solid model for spherical steel inclusions embedded in thermoplastic material) with the experimental data for a 794 μm radius spherical steel inclusion embedded in the same host.

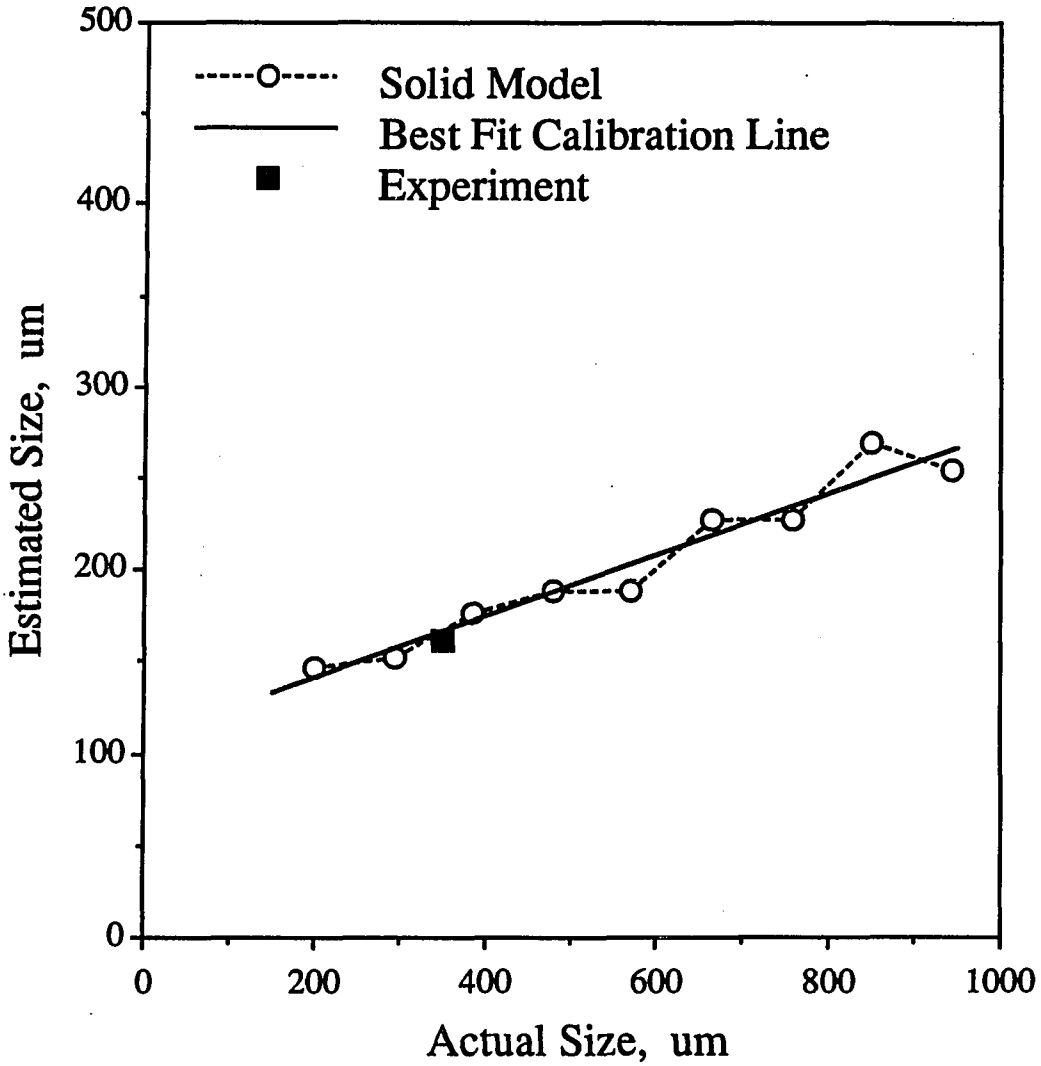

Figure 12a. FM sizing result for a 350 μm radius spherical void embedded in fused silica using the best-fit calibration line determined from the solid model calibration curve for voids embedded in the same host.

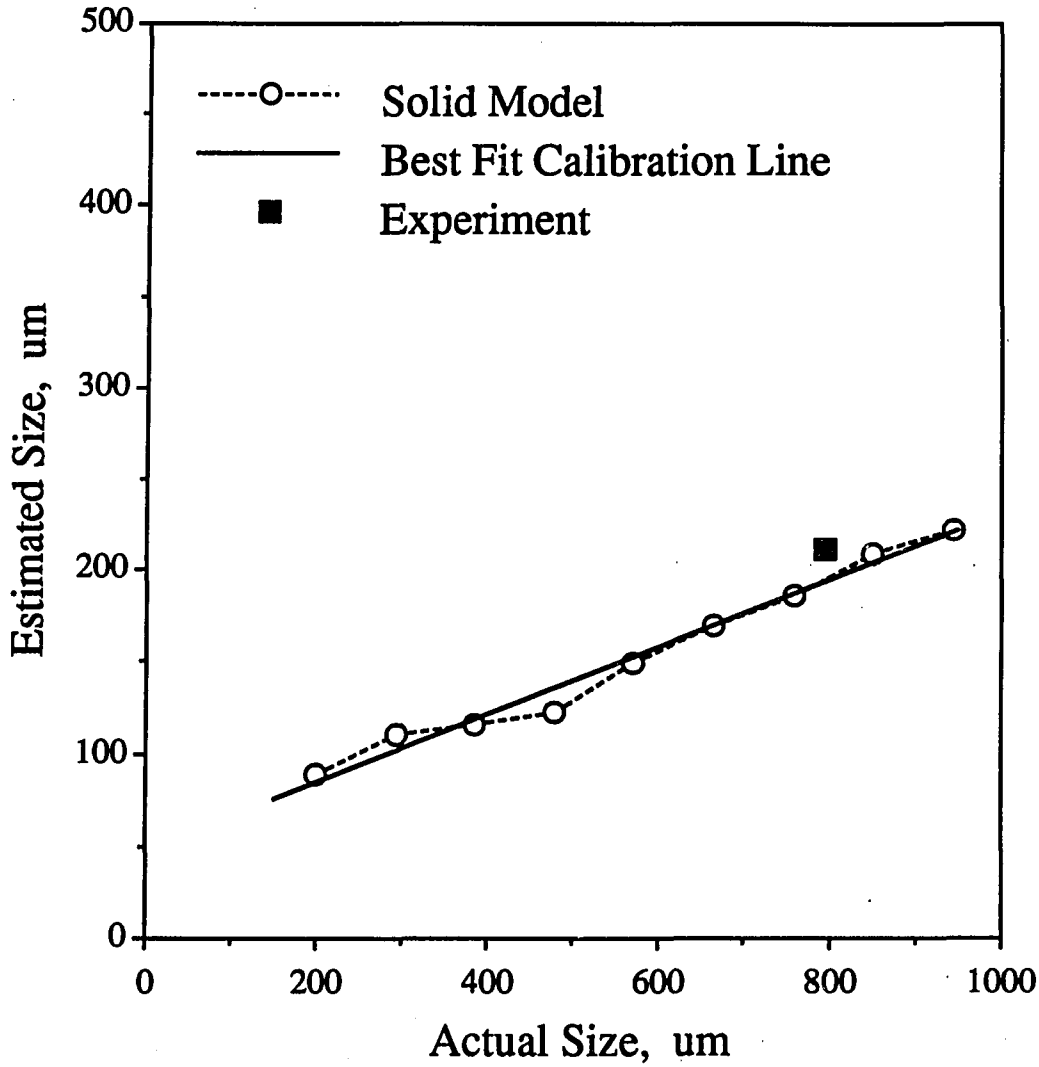

Figure 12b. FM sizing result for a 794 μm radius spherical steel inclusion embedded in a thermoplastic material using the best-fit calibration line determined from the solid model calibration curve for steel inclusions embedded in the same host.

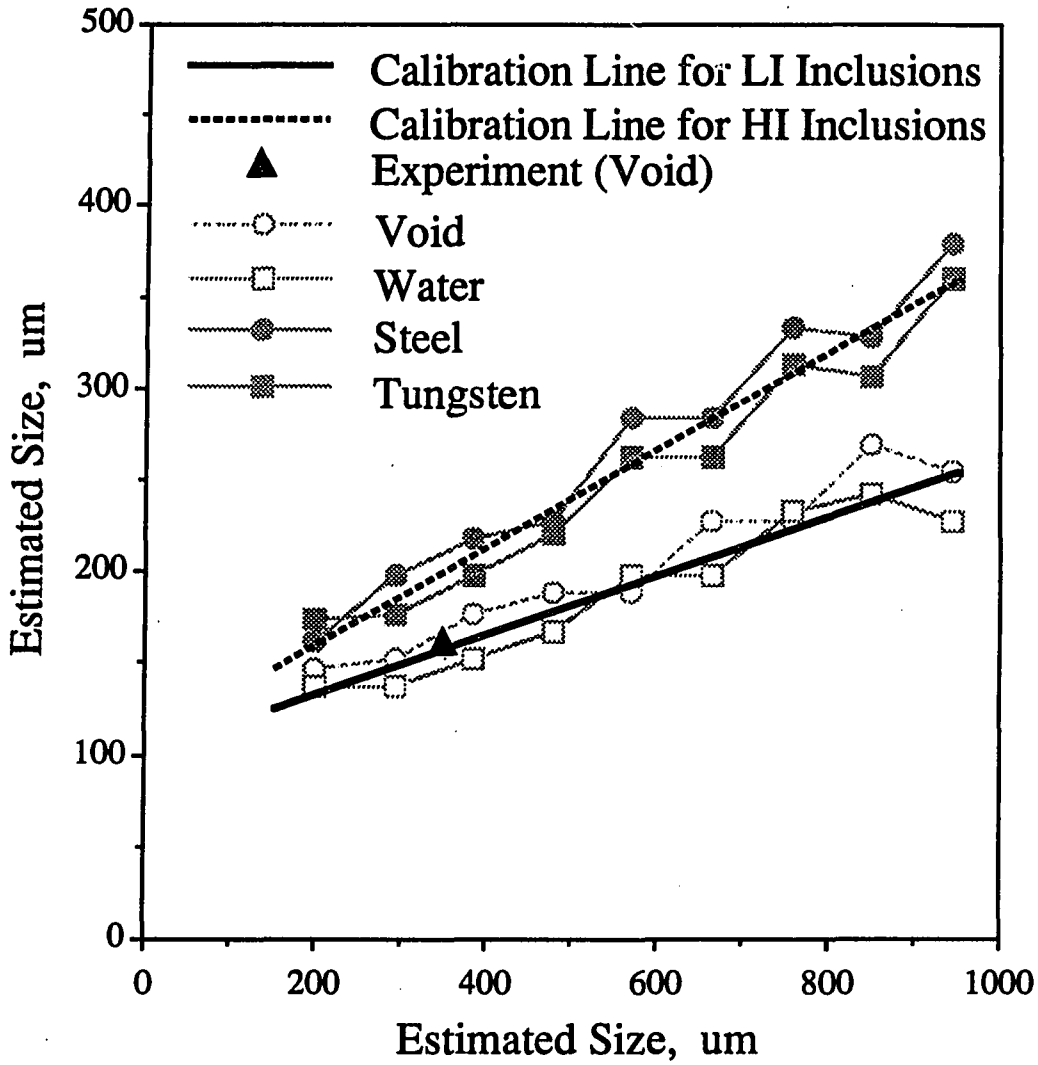

Figure 13a. FM sizing result for a 350 μm radius spherical void embedded in fused silica using the best-fit calibration line determined from the solid model calibration curve for inclusions whose impedances are less than that of the host.

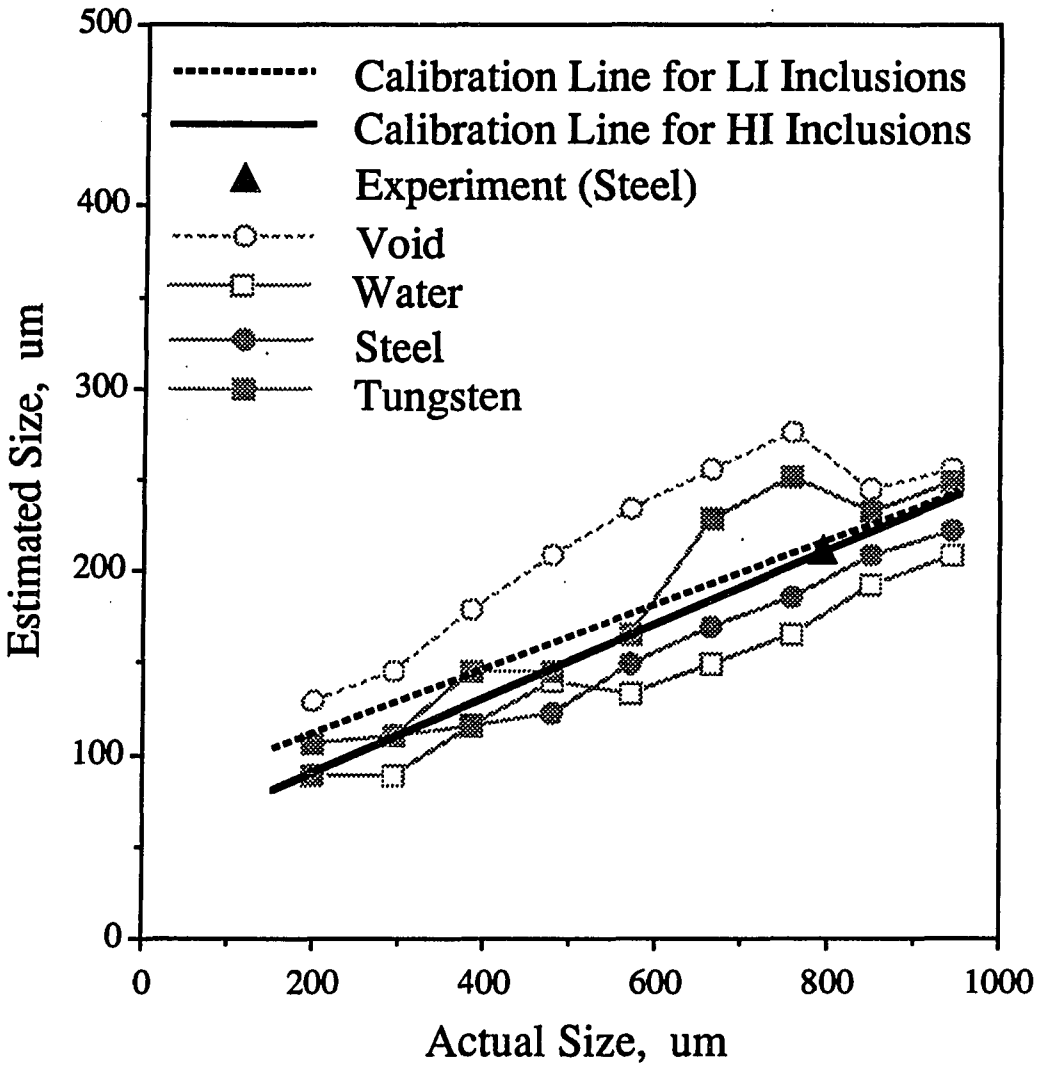

Figure 13b. FM sizing result for a 794 μm radius spherical steel inclusion embedded in a thermoplastic material using the best-fit calibration line determined from the solid model calibration curve for inclusions whose impedances are greater than that of the host.

GENERAL SUMMARY

In this work, we have presented some new approaches for both classifying and sizing isolated flaws inside materials using ultrasonic measurements.

In Part I, we have demonstrated the use of probabilistic neural networks (PNN's) for the classification of welding flaws. The PNN's produced reasonable and consistent classification performances for the two experimental cases considered. In the second data set, the PNN showed the high performance of a back-propagation network but without having the lengthy training time. Also for both cases, the PNN's behaved similarly to K-nearest neighbor (KNN) classifiers while retaining their unique advantages such as speed. We showed that the PNN is indeed a good choice as a classifier for these weld problems.

In Part II, we have demonstrated that the flat-bottom hole model developed in [36] is capable of producing theoretical time domain DGS diagrams and frequency response curves that compare well with experiments, even in the near-field. The model, therefore, generalizes the Krautkramer model [34] to a practical immersion testing geometry where no limitation is placed on the distance between the transducer and the hole. The quality of the experimental results obtained in this study suggests that the model can serve as an important new theoretical reference standard for a variety of ultrasonic calibration and sizing applications.

In Part III, we have described a new time-of-flight equivalent (TOFE) sizing method for relatively large flaws in materials. We have shown that for volumetric flaws using time-of-flight information in two-sided scanning makes the algorithm stable and fast. For cracks, the method is always stable and

fast, even in one-sided scanning. From our tests of the TOFE method in both a composite material and a weldment we have shown that the method is accurate provided that the wavespeed in the material is well characterized. The excellent performance of the method observed in this study demonstrates that it can serve as a robust sizing tool for many practical applications.

In the last part, we have presented two new approaches to equivalent sizing for relatively small flaws; an amplitude-based equivalent (ABE) sizing method and a first moment (FM) method. The ABE sizing method showed very good peformance on both synthetic and experimental data sets. In the sizing of a "crack" in a titanium alloy we demonstrated how this method is able to reduce errors caused by the zero-of-time problem. The FM method also showed excellent performance in sizing spherical flaws with both high and low acoustic impedances even in the absence of apriori information on the type of flaw present. The accuracy of these results verify that this method is a viable sizing method for small flaw size estimation.

In this work, we have developed robust methods for both classification and sizing of flaws in materials, which can be applied to various practical applications. Extensive use has been made of a number of "tools" including ultrasonic wave scattering models, experimental instrumentation, digital signal processing techniques, numerical optimization algorithms and neural networks.

Even with these advances, considerable challenges still remain. In the area of flaw classification, other neural network architectures may be competitive to the PNN and should be considered. Similarly, other approaches, such as

statistical classification and regression rules, may be useful tools for solving ultrasonic flaw classification problems.

In the area of flaw sizing by use of reference/calibration standards, we developed a model-based approach which can determine the DGS diagrams and frequency response curves of flat-bottom holes. This model-based approach can be extended to other reference/calibration standards such as a sphere.

In the area of equivalent flaw sizing, there also exist a number of opportunities. For large flaws, the performance of the TOFE sizing algorithms needs to be tested in more general situations involving curved surfaces, more general composites, different reflectors, etc. In the ABE method, further work is needed to verify that the method is indeed insensitive to sources of experimental error, such as surface roughness, and can be applied to flaws of irregular shape. The FM sizing method showed excellent performance for spherical flaws in this work, but obviously needs more work to test its performance for flaws of more general shape. Finally, another potential extension would be a combination of the ABE and the FM sizing methods. For example, one could apply the ABE method to obtain scaled size information and then use the FM method to determine the scaling constant.

LITERATURE CITED

1. International Institute of Welding, The Evaluation of Ultrasonic Signals, Cambridge, England: Welding Institute for International Institute of Welding 1987.

2. International Institute of Welding, Handbook on the Ultrasonic Examination of Welds, Cambridge, England: Welding Institute for International Institute of Welding 1977.

3. V. G. Shcherbinskii and V. E. Belyi, "New informative index for the nature of flaws in ultrasonic inspection." Soviet Journal of Nondestructive Testing, Vol. 11, pp. 279-288, 1975.

4. A. K. Volpinkin, "Diffracted waves and their application in ultrasonic nondestructive testing II. Practical application of diffracted waves." Soviet Journal of Nondestructive Testing, Vol. 21, pp. 143-154, 1985.

5. G. J. Gruber, "Defect identification and sizing by the ultrasonic satellite-pulse technique." Journal of Nondestructive Evaluation, Vol. 1, pp. 263-273, 1980.

6. C. P. Chiou and L. W. Schmerr, "A quasi-pulse-echo technique for ultrasonic flaw classification." Ultrasonics, Vol. 29, pp. 471-481, 1991.

7. O. R. Gericke, "Determination of the geometry of hidden defects by ultrasonic pulse analysis testing." Journal of Acoustical Society of America, Vol. 35, pp 364-368, 1963.

8. O. R. Gericke, "Ultrasonic spectroscopy" in Research Techniques in Nondestructive Testing, pp. 31-61, Ed. R. S. Sharpe, London: Academic Press, 1970.

9. D. W. Fitting and L. Adler, Ultrasonic spectral analysis for Nondestructive Evaluation. New York: Plenum Press, 1981.

10. J. L. Rose, "Elements of a feature-based ultrasonic inspection system." Materials Evaluation, Vol. 42, pp. 210-218, 1984.

11. J. L. Rose, Y. H. Jeong, and C. T. Cooper, "A methodology for reflector classification analysis in complex geometric welded structures." Materials Evaluation, Vol. 42, pp. 98-106, 1984.

12. J. L. Rose, J. Nestleroth, L. Niklas, O. Ganglbauer, J. Ausserwoeger and F. Wallner. "Flaw classification in welded plates employing a multidimensional feature-based decision process." Materials Evaluation, Vol. 42, No. 4, pp. 433-438, 443, 1984

13. S. F. Burch and N. K. Bealing, "A Physical approach to the automated ultrasonic characterization of buried weld defects in ferritic steel." NDT International, Vol. 19, pp. 145-152, 1986.

14. S. F. Burch, "Objective characterization of welding defects using physical based pattern recognition techiniques." in Review of Progeress in Quantitative Nondestructive Evaluation, Vol. 7B, eds. D. O. Thompson and D. E. Chimenti, pp. 1495-1502, New York: Plenum Press, 1988.

15. A. N. Mucciardi, R. Shankar and M. F. Whalen. "Application of Adaptive Learning Networks to NDE Methods." Interdisciplinary Program for Quantitative Flaw Definition Special Report Third Year Effort, 1976.

16. M. F. Whalen and A. N. Mucciardi. "Inversion of Physically Recorded Ultrasonic Waveforms Using Adaptive Learning Network Models Trained on Theoretical Data." In Proc. ARPA/AFML Review of Progress in Quantitative NDE. ed. D. O. Thompson, Air Force Materials Laboratory Technical Report AFML-TR-78-205, pp. 341-367, 1979.

17. L. S. Koo, "Ultrasonic flaw classification: an approach using modelling, signal processing, and adaptive learning." Ph.D. Dissertation, Iowa State University, 1987.

18. S. M. Nugen, L. W. Schmerr, K. M. Christensen, and B. K. Lovewell, "Design and implementation of an expert system for flaw classification." Microcomputer Applications, Vol. 9, pp. 1-8, 1990.

19. L. W. Schmerr, K. E. Christensen, S. M. Nugen, L.-S. Koo and C.-P. Chiou. "Ultrasonic Flaw Classification - An Expert System Approach." in Review of Progress in Quantitative Nondestructive Evaluation, Vol. 8A, eds. D. O. Thompson and D. E. Chimenti, pp. 657-664, New York: Plenum Press, 1989.

20. R. P. Lippmann, "An introduction to computing with neural nets.", IEEE ASSP Magazine, pp. 4-22, April 1987.

21. Y. H. Pao, Adaptive Pattern Reconition and Neural Networks. Reading: MA, Addison-Wesley Publishing Co., Inc., 1989

22. D. E. Rumelhart, G. E. Hinton and R. J. Williams, "Learning internal representations by error propagation." in Parallel Distributed Processing, eds. D. E. Rumelhart, J. L. McClelland and the PDP Research Group, Vol. 1, pp. 318-362, Cambridge, MA:MIT Press, 1986

23. L. Udpa and S. S. Udpa, "Eddy current defect characterization using neural network." Materials Evaluation, Vol. 48, pp. 342-347, 353, 1990.

24. J. M. Mann, L. W. Schmerr and J. C. Moulder, "Neural network inversion of uniform-field eddy current data." Materials Evaluation, Vol. 49, pp. 34-39, 1991.

25. C. P. Chiou and L. W. Schmerr, "A neural network model for ultrasonic flaw sizing." to appear in Nondestructive Testing and Evaluation.

26. L. M. Brown and R. DeNale, "Classification of ultrasonic defect signatures using an artificial neural network." in Review of Progress in Quantitative Nondestructive Evaluation, Vol. 10A, eds. D. O. Thompson and D. E. Chimenti, pp. 705-712, New York: Plenum Press, 1990.

27. D. Berry, L. Udpa and S. S. Udpa, "Classification of ultrasonic signals via neural networks." in Review of Progress in Quantitative Nondestructive Evaluation, Vol. 10A, eds. D. O. Thompson and D. E. Chimenti, pp. 697-704, New York: Plenum Press, 1990.

28. D. F. Specht, "Probabilistic neural networks for classification, mapping, or associative memory." in Proceedings of the IEEE InternationalConference on Neural Networks, Vol. 1, pp. 525-532, 1988.

29. D. F. Specht, "Probabilistic neural networks." Neural Networks, Vol. 3, pp. 109-118, 1990.

30. D. F. Specht, "Probabilistic neural networks and polynomial adaline as complementary techniques for classification." IEEE Transactions on Neural Networks, Vol. 1, No. 1, pp. 111-121, 1990.

31. R. B. Thompson and D. O. Thompson, "Ultrasonics in nondestructive evaluation." Proceedings of the IEEE, Vol. 73, pp. 1716-1755, 1985.

32. R. B. Thompson, "Quantitative ultrasonic nondestructive evaluation methods." Transactions of ASME/ Journal of Applieds Mechanics, Vol. 50, pp. 1191-1201, 1983.

33. J. Krautkramer and H. Krautkramer, Ultrasonic Testing of Materials, 4th Edition, New York: Springer-Verlag, 1990.

34. J. Krautkramer, "Determination of the size of defects by the ultrasonic impulse echo methods." British Journal of Applied Physics, Vol. 10, pp. 240-245, 1959.

35. L. W. Schmerr and A. Sedov, "The flat-bottom hole: an ultrasonic scattering model." Research in Nondestructive Evaluation, Vol. 1, pp. 181-196, 1989.

36. A. Sedov, L. W. Schmerr, and S. J. Song, "Ultrasonic scattering of a flat-bottom hole in immersion testing: an analytic model." to appear in Journal of Acoustical Society of America.

37. D. Heinrich, K. H. Mayer, G. Muller and W. Prestel, "Manual and mechanized ultrasonic inspection of large components in respect of flaw estimation by fracture mechanics." Nuclear Engineering and Design, Vol. 112, pp. 127-137, 1989.

38. M. G. Silk, A. M. Stoneham and J. A. G. Temple, The Reliability of Non-Destructive Inspection, Bristol, England: Adam Hilger, 1987.

39. M. G. Silk, "Sizing crack-like defects by ultrasonic means." in Research Techniques in Nondestructive Testing, Vol. 2, Ed. R. S. Sharpe, Ch. 2, London: Academic Press, 1977.

40. M. G. Silk, "The use of diffraction based time-of-flight measurements to locate and size defects." British Journal of NDT, Vol. 26, pp. 208-213, 1984.

41. J. P. Charlesworth and J. A. G. Temple, Engineering Applications of Ultrasonic Time-of-Flight Diffraction, Somerset, England: Research Studies Press, 1989.

42. G. J. Gruber, G. J. Hendrix and W. R. Schick, "Characterization of flaws in piping welds using satellite pulses." Materials Evaluation, Vol. 42, pp. 426-432, 1984.

43. C. F. Schueler, H. Lee and G. Wade, "Fundamentals of digital ultrasonic imaging." IEEE Transactions on Sonics and Utrasonics, Vol. SU-31. pp. 195-217, 1984.

44. J. Seydel, "Ultrasonic synthetic-aperture focusing techniques." in Research Techniques in Nondestructive Testing, Vol. VI, Ed. R. S. Sharpe, New York: Academic Press, pp. 1-48, 1982.

45. S. O. Harrold, "Ultrasonic focusing techniques." in Research Techniques in Nondestructive Testing, Vol. VI, Ed. R. S. Sharpe, New York: Academic Press, pp. 49-106, 1982.

46. B. Grohs, O. A. Barbian, W. Kappes, H. Paul, R. Licht and F. W. Hoh, "Characterization of flaw location, shape, and dimensions with the ALOK system." Materials Evaluation, Vol. 40, pp. 84-89, 1982.

47. B. P. Hildebrand and B. B. Brenden, An Introduction to Acoustical Holography, New York: Plenum Press,1972.

48. L. S. Koo, H. R. Shafiee, D. K. Hsu, S. J. Wormley and D. O. Thompson, "Two-dimensional ultrasonic tomography in nondestructive evaluation by using area functions." IEEE Transactions on Ultrasonics, Ferroelectrics, and Frequency Control, Vol. 37, pp. 148-158, 1990.

49. D. K. Hsu, J. H. Rose and D. O. Thompson, "Reconstruction of inclusions in solids using ultrasonic Born inversion." Journal of Applied Physics, Vol. 55, pp. 162-168, 1984.

50. D. K. Hsu, D. O. Thompson and S. J. Wormley "Reliability of reconstruction of arbitrarily oriented flaws using multiview transducers." IEEE Transactions of Ultrasonics, Ferroelectrics, and Frequency Control, Vol. UFFC-34, pp. 508-514, 1987.

51. A. Sedov and L. W. Schmerr, "The time domain elastodynamic Kirchhoff approximation for cracks: the inverse problem," Wave Motion, Vol. 8, pp. 15-26, 1986.

52. L. W. Schmerr, A. Sedov and C. P. Chiou, "A unified constrained inversion model for ultrasonic flaw sizing." Research in Nondestructive Evaluation, Vol. 1, pp. 77-97, 1989.

53. L. J. Bond, C. A. Chaloner, S. J. Wormley, S. P. Neal, and J. H. Rose, "Recent advances in Born Inversion (weak scatterers)." in Review of Progress in Quantitative Nondestructive Evaluation, Eds. D. O. Thompson and D. E. Chimenti, Vol. 7A, pp. 437-444, New York: Plenum Press, 1988.

54. C. A. Chaloner and L. J. Bond, "Investigation of the 1-D inverse Born technique." IEE Proceedings, Vol. 134, Pt. A, pp. 257-265, 1987.

55. R. B. Thompson, "Status of implementation of the inverse Born sizing algorithm." in Review of Progress inQuantitative Nondestructive Evaluation, Eds. D. O. Thompson and D. E. Chimenti, Vol. 4A, pp. 611-621, New York: Plenum Press, 1985.

56. J. Yang and L. J. Bond, "Errors in determining the flaw centroid by using area functions." to be appeared in Review of Progress in Quantitative Nondestructive Evaluation, Eds. D. O. Thompson and D. E. Chimenti, Vol. 11, New York: Plenum Press, 1992.

57. C. P. Chiou and L. W. Schmerr, "New approaches to model-based ultrasonic flaw sizing." submitted to Journal of Acoustical Society of America.

ACKNOWLEDGMENTS

I would like to express my sincere gratitude to my major professor, Dr. Lester W. Schmerr, for his support and guidance in this work as well as in my graduate study. For his great understanding and insight in various fields together with his patience and kindness, I will never be able to fully express my appreciation.

I would also like to thank Professors R. Bruce Thompson, David K. Hsu, Anna L. Pate, John P. Basart and Otto Buck for serving as my committee members, and Dr. Donald O. Thompson for ultimately giving me the opportunity to pursue this research at the Center for NDE.

Thanks are also due to my senior colleague Dr. Chien-P. Chiou for his valuable assistance and discussion; to Mr. Samuel J. Wormley for his kind help and advice. I am also indebted to many of my colleagues, Dr. Hyunjo Jeong, Mr. Babak Forouraghi, Mr. Steve Nugen, and Mr. James Mann for their friendship and encouragement. The support from both the Department of Aerospace Engineering and Engineering Mechanics and Center for Nondestructive Evaluation at Iowa State University is acknowledged.

Finally, I am especially thankful to my mother and my wife, to whom this dissertation is dedicated.